

THESIS FOR THE DEGREE OF DOCTOR OF PHILOSOPHY

$\text{YBa}_2\text{Cu}_3\text{O}_{7-\gamma}$ nanogaps: A path toward
hybrid junctions

REZA BAGHDADI



Quantum Device Physics Laboratory
Department of Microtechnology and Nanoscience (MC2)
CHALMERS UNIVERSITY OF TECHNOLOGY
Göteborg, Sweden 2017

YBa₂Cu₃O_{7-γ} nanogaps: A path toward hybrid junctions

REZA BAGHDADI

ISBN 978-91-7597-529-0

©REZA BAGHDADI, 2017

Author email: reza.baghdadi@chalmers.se

Doktorsavhandlingar vid Chalmers tekniska högskola

Ny serie nr 4155

ISSN 0346-718X

Chalmers University of Technology

Department of Microtechnology and Nanoscience (MC2)

Quantum Device Physics Laboratory

SE-412 96 Göteborg, Sweden

Telephone +46 (0)31-772 1000

ISSN 1652-0769

Technical Report MC2-354

Printed by Chalmers Reproservice, Chalmers University of Technology
Göteborg, Sweden, January 2017

YBa₂Cu₃O_{7- γ} nanogaps: A path toward hybrid junctions

REZA BAGHDADI

Department of Microtechnology and Nanoscience, MC2

Chalmers University of Technology, Göteborg, Sweden 2017

Abstract

This thesis paves the way for the realization of hybrid Josephson junctions based on YBa₂Cu₃O_{7- γ} (YBCO) nanogaps. This allows one to explore a much richer Josephson physics where the superconducting properties of YBCO, like the d-wave order parameter and large superconducting gap, are proximized into the 2-dimensional Dirac materials such as graphene, or topological insulators.

The core part of the thesis discusses a complicated nanopatterning technology employed to realize encapsulated YBCO nanogaps where the electrodes preserve superconducting properties close to the bulk. To assess the quality of the nanogaps, we promoted three sets of YBCO nanowires fabricated by applying different lithographic processes. Using a thermally activated vortex-entry model applied to resistance vs. temperature measurements close to the critical temperature T_C allows us to determine the maximum damage the nanowires undergo during the patterning. We found that the effective width of the nanogap is of the order of 100 nm at T_C while retaining the geometrical value of about 35 nm at lower temperatures. The effect of an ex-situ ozone annealing is investigated both on YBCO films and nanowires. Studying the X-ray diffraction pattern on bare films revealed that the ozonation is a practical method to oxygenate YBCO films. To probe the effectiveness of this method on nanostructures, we compared the critical current density and the broadening of the resistive transition close to T_C measured before and after the ozone treatment. We conclude that the ozone treatment is instrumental in recovering very high-quality superconducting properties inside the nanostructures, which were degraded by the oxygen out-diffusion occurring during the nanopatterning.

The feasibility of the encapsulated YBCO nanogaps for hybrid Josephson devices is demonstrated by bridging them with thin Au films. We successfully fabricated and studied planar Superconductor-Normal-Superconductor (SNS) Josephson junctions made of YBCO high- T_C superconductor (S) and Au normal metal (N). Our junctions showed Fraunhofer-like modulation patterns and Shapiro steps when they are irradiated by microwave radiation. By using a double barrier SINIS model, we have studied the transport properties of the critical current in temperature. The results of the fitting suggest that the Cooper pair transport is mainly across the 5 nm Ti sticking layer, underneath of the Au film bridge, due to the ozone treatment.

We promoted the growth of fully untwinned high-quality *a*-axis oriented YBCO films on LaSrGaO₄ substrates using PrBa₂Cu₃O_{7- γ} as a buffer layer. Such films allow for a strong induced superconductivity in proximity based multilayer devices due to the large coherence length along the *a*-axis, compared to the *c*-axis film based devices. YBCO nanowires at different angles with respect to the [0,1,0] direction of the substrate are realized to investigate the in-plane anisotropy of the critical current density. The in-plane anisotropy could be explained by considering the anisotropy in the coherence length ξ and London penetration depth λ_L along the *b*- and *c*- axis film.

Keywords: High- T_C superconductors, YBCO nanogap based hybrid junction, YBCO nanowires, YBCO NanoSQUIDS, *a*-axis YBCO nanowires.

I DEDICATE THIS THESIS TO MY GRANDFATHER.

STILL I AM TRAVELING,
I THINK
THERE IS A BOAT IN THE RIVERS OF WORLD.
Sohrab Sepehri (1928-1980)

List of Publications:

The thesis is based on the work contained in the following papers:

Paper I

Toward $\text{YBa}_2\text{Cu}_3\text{O}_{7-\gamma}$ Nanoscale Structures for Hybrid Devices

Reza Baghdadi, Riccardo Arpaia, Thilo Bauch, Floriana Lombardi.

IEEE Trans. on Appl. Supercond., Vol. 25 (3) 2245, (2015).

Paper II

Fabricating Nanogaps in $\text{YBa}_2\text{Cu}_3\text{O}_{7-\gamma}$ for Hybrid Proximity-Based Josephson Junctions

Reza Baghdadi, Riccardo Arpaia, Sophie Charpentier, Dmitri Golubev, Thilo Bauch, Floriana Lombardi.

Phys. Rev. Applied 4, 014022 (2015).

Paper III

Josephson effect through $\text{YBa}_2\text{Cu}_3\text{O}_{7-\gamma}$ /Au Nanogaps: A route for hybrid devices

Reza Baghdadi, Simon Abay, Dmitri Golubev, Thilo Bauch, Floriana Lombardi.

Manuscript to be submitted.

Paper IV

Study of in-plane electrical transport anisotropy of a -axis oriented $\text{YBa}_2\text{Cu}_3\text{O}_{7-\gamma}$ nanodevices

Reza Baghdadi, Riccardo Arpaia, Evgeny Stepantsov, Marco Arzeo, Dmitri Golubev, Domenico Montemurro, Eric Andersson, Thilo Bauch, and Floriana Lombardi.

Submitted to Physical Review B.

Paper V

Improved noise performance of ultrathin $\text{YBa}_2\text{Cu}_3\text{O}_{7-\gamma}$ Dayem bridge nanoSQUIDs

R. Arpaia, M. Arzeo, **R. Baghdadi**, E. Trabaldo, F. Lombardi, and T. Bauch.

SUST 30 (1), 014008 (2016).

Paper VI

Transport properties of ultrathin $\text{YBa}_2\text{Cu}_3\text{O}_{7-\gamma}$ nanowires: a route to single photon detection

Riccardo Arpaia, **Reza Baghdadi**, Regina Ciancio, Dimitri Golubev, Eldoardo Trabaldo, Thilo Bauch, Floriana Lombardi.

Submitted to Phys. Rev. Appl.

Paper VII

Resistive state triggered by vortex entry in $\text{YBa}_2\text{Cu}_3\text{O}_{7-\gamma}$ nanostructures

Riccardo Arpaia, Dmitri Golubev, **Reza Baghdadi**, Marco Arzeo, Gunta Kunakova, Sophie Charpentier, Shahid Nawaz, Floriana Lombardi, Thilo Bauch.

Physica C: Superconductivity and its Applications.

Other related manuscript by the Author not included in this thesis:

Paper 1

Toward ultra high magnetic field sensitivity YBCO nanowire based superconducting quantum interference devices

M. Arzeo, R. Arpaia, **R. Baghdadi**, F. Lombardi and T. Bauch

Journal of Applied Physics 119 (17), 174501.

Paper 2

Topological superconductivity on the surface states of Bi₂Te₃

S. Charpentier, L. Galletti, Y. Song, **R. Baghdadi**, D. Golubev, J. Linder, S. M. Wang, F. Tafuri, T. Bauch and F. Lombardi

Submitted to Nature Nanotechnology.

Paper 3 Hot spot formation in electron doped PCCO nanobridges

Sophie Charpentier, Riccardo Arpaia, **Reza Baghdadi**, Jonathan Gaudet, Dominique Matte, and Patrick Fournier, Tomas Lofwander Thilo Bauch, Dmitri Golubev and Floriana Lombardi

Physical Review B 94 (6), 060503.

Paper 4

Noise properties of YBCO Nanostructures

Edoardo Trabaldo, Marco Arzeo, Riccardo Arpaia, **Reza Baghdadi**, Eric Andersson, Floriana Lombardi, and Thilo Bauch.

Accepted to be published in IEEE Trans. on Appl. Supercond.

Paper 5

Superconducting NbN nanowire networks templated by porous Si substrates

M. Salvato, **R. Baghdadi**, C. Cirillo, M. Caputo, T. Bauch, F. Lombardi, S.L. Prischepa, A.L. Dolgiy, V.P. Bondarenko, and C. Attanasio

In manuscript.

Contents

DEDICATION	III
1 INTRODUCTION	1
2 SUPERCONDUCTIVITY AND CUPRATES	5
2.1 Introduction to superconductivity	5
2.2 Superconductivity in the high critical temperature cuprates	9
3 JOSEPHSON JUNCTIONS	15
3.1 Josephson Effect	15
3.2 Fluctuation Mechanisms in Superconductors	19
3.3 Josephson junction in a magnetic field	21
3.4 The Resistively and Capacitively Shunted junction (RCSJ junction) . .	24
3.5 AC-Josephson effect: Shapiro Steps	27
3.6 Superconducting QUantum Interference Devices (SQUIDS)	28
4 MESOSCOPIC TRANSPORT IN SNS JUNCTIONS	31
4.1 Tunneling Current for NIN , NIS and SIS junctions	31
4.2 SNS junctions	37
4.3 Classification of weak links	38
4.4 Critical current in SNS Josephson Junctions	40
4.5 Theoretical model for Josephson current in a $SINI'S$ junction	42
5 YBCO FILM GROWTH	47
5.1 YBCO thin film growth using pulsed laser deposition	47
5.2 Growing c -axis YBCO on MgO (1 1 0) substrate	47
5.3 Growing a -axis YBCO on SLGO substrate using PBCO buffer layer . .	50
5.4 Characterization of a -axis oriented YBCO films	52
5.5 Growing ultra-thin c -axis YBCO films on MgO (1 1 0)	54
6 NANOFABRICATION PROCESSES	57
6.1 Fabrication details of YBCO nanowires	57
6.2 Fabrication details of the Au/YBCO interface resistance devices	60

6.3	Fabrication details of the YBCO-Au-YBCO Junctions	62
7	TRANSPORT CHARACTERIZATION OF ENCAPSULATED YBCO NANOWIRES	65
7.1	Critical current density J_C as a function of the nanowire width and length	65
7.2	Estimate the lateral damage of 1EBL and 3EBL nanowires	67
7.3	Ozone treatment	70
8	TRANSPORT CHARACTERIZATION OF YBCO-AU-YBCO JUNCTIONS	77
8.1	YBCO/Au interface contact resistance	77
8.2	Transport properties of YBCO-Au-YBCO junctions	81
8.3	Shapiro steps	84
8.4	Temperature dependence of the current in YBCO-Au-YBCO junctions .	86
9	IN-PLANE TRANSPORT ANISOTROPY OF a -AXIS ORIENTED YBCO NANODEVICES	91
9.1	Study of the in-plane anisotropy in a -axis YBCO nanostructures	91
9.2	Resistance vs. temperature of nanowire along $\gamma = 0^\circ$ and $\gamma = 90^\circ$	95
9.3	Effect of ozone treatment on superconducting properties of nanowires .	97
9.4	Temperature dependence of the London penetration depth	97
9.5	Half integer Shapiro-like steps in underdoped a -axis nanowires	98
10	CONCLUSION	101
	APPENDIX A CONSTANTS-SYMBOL DEFINITION-ABBREVIATION	103
	APPENDIX B MEAN FREE PATH IN AU	107
	APPENDIX C CHARACTERIZATION OF AU QUALITY	109
	APPENDIX D MEASUREMENT SETUP	111
	D.1 280 mK Heliox Fridge	111
	D.2 Electrical measurement	111
	D.3 Drawplot plotting software	113
	APPENDIX E NANOFABRICATION PROCESSES	115
	E.1 Fabrication recipe for YBCO nanowires/nanogap	115
	E.2 Fabrication recipe for encapsulating nanowires/nanogap	119
	E.3 Fabrication recipe for defining the normal layer in SNS junctions	120
	ACKNOWLEDGMENTS	121
	REFERENCES	135

1

Introduction

In the latest years, the great advances of nanotechnologies applied to High Temperature Superconductors (HTS) have opened the door to a new class of Josephson devices with novel functionalities. We refer here to the realization of hybrid devices involving HTS electrodes and exotic barriers represented for instance by Graphene^{1,2}, a Topological Insulator (TI) or a semiconducting nanowire with spin orbit coupling^{3,4}. Interesting theoretical reports, for example, make use of the d-wave symmetry of the order parameter in HTS and the large value of the superconducting gap to design experiments to reveal the existence of Majorana fermions, still elusive particles in solid state systems, that are supposed to nucleate at the interface between a superconductor and a TI or semiconducting nanowire⁵⁻⁸. The search for Majorana fermions, in solid states physics, has recently received a great boost, since these peculiar particles, which are their own antiparticles, obey a non-abelian statistics at the basis for topological quantum computation which evades decoherence at the hardware level⁹⁻¹². Another interesting example is given by the realization of HTS devices interfaced with Graphene. In such structures one could study the Quantum Hall effect in a regime of Josephson transport, which is accessible because of the extremely high upper critical field (of the order of ≈ 100 T) and superconducting gap in HTS materials^{13,14}. At the same time Superconductors (S)-Semiconductors interfaces have a broad potential for a wide range of applications¹⁵⁻¹⁷. The use of HTS could bring several advantages, and more importantly higher operational temperatures fundamental for practical applications of superconducting field effect transistors.

The fabrication of HTS hybrid devices requires, however, the engineering of re-

producibile and stable nanogaps. This is a challenging task because of the surface and chemical instability of HTS thin films and the very short superconducting coherence length ξ that for YBCO (the most studied HTS) is of the order of a few nanometers ($\xi_{a,b} \approx 1 - 2$ nm and $\xi_c \approx 0.2 - 0.3$ nm). Previous attempts to fabricate nanogaps/nanotrenches made use of high aspect ratio trenches excavated in perovskite substrates by various techniques¹⁸⁻²¹. The subsequent YBCO growth was expected to be discontinued at the trench top, resulting in the formation of a YBCO nanogap, which was bridged with a noble metals Au/Ag forming a Superconductor (S)-Normal conductor (N)- Superconductor (S) Josephson junction. However these approaches suffered from the random formation of grain boundaries along the trench profile, which could mimic the SNS behavior [10]. Moreover, the resulting YBCO nanogaps cannot be easily integrated with complex barriers like for example flakes of TI/Graphene or semiconducting nanowires since the YBCO nanogaps are first exposed to ambient and then to chemicals and resists due to further processing required for interfacing with the normal metal barrier. This fact would seriously damage the YBCO nanogap.

In this thesis, we show a flexible way to obtain $\text{YBa}_2\text{Cu}_3\text{O}_{7-\gamma}$ (YBCO) nanogaps, starting from a bilayer formed by a c -axis YBCO film covered in-situ by Au. This represents the main building block to realize HTS hybrid devices. The basic concept we have used is the complete Au encapsulation of the YBCO electrodes, forming the nanogap. This procedure allows the preservation of the superconducting properties of YBCO (close to those of pristine film) in the closest proximity of the normal metal barrier (N). The feasibility of the encapsulated nanogaps, for hybrid devices, has been tested by bridging the nanogaps with Au and by studying transport properties of the resulting S-N-S junctions. The observation of Josephson effects, with rather high current densities, and a Fraunhofer-like dependence in magnetic fields of the critical current are clear manifestations of a) a high transparency between the YBCO and the *in-situ* Au and the formation of a minigap in the Au bridge and b) rather uniform Josephson transport properties across the junction.

a -axis YBCO films are in general more suitable for the fabrication of hybrid devices This is due to the two-dimensionality of the d -wave order parameter (confined to the a - b planes) and to the anisotropy of the superconducting properties. Hybrid devices made of a -axis film are supposed to have a stronger induced proximity effect due to direct contact of the a - b planes with the normal barrier under study. At the same time nanostructures made on bare a -axis films can also be considered ideal systems to study the effect of confinement on the anisotropy of the transport properties of HTS. However a -axis films are much more complicated to deposit and nanopattern compared to the c -axis counterpart. In this thesis we have succeeded in depositing high quality untwinned a -axis thin film and realize nanowires and nanoSQUIDS at different angles γ with respect to the one of the in plane direction of the substrate. From the resistive transition as a function of temperature, measurements of the critical current density of the nanowires and of the critical current modulation of the nanoSQUIDS, we have gotten

important information about the anisotropy of the coherence length, ξ , and the London penetration length, λ_L , of YBCO when the dimensionality of the systems is strongly reduced. Indeed for $\gamma = 90^\circ$ the nanowires are characterized by a series of confined a - b planes with nanoscale dimensions. At the same time, such kind of structure can also inspire future work aimed at studying the effect of the confinement of the a - b planes or the appearance of the recently discovered charge density wave order and its interplay with high critical temperature superconductivity.

The thesis is structured as follows.

Chapter 2 introduces superconductivity and discusses the important properties of conventional superconductors and HTS. Chapter 3 describes the Josephson effect, and the behavior of a Josephson junction in presence of a magnetic field and a microwave radiation. A brief description and the performance of Superconducting QUantum Interference Devices (SQUIDS) is also given. Chapter 4 discusses the most relevant theoretical aspects of the transport in SNS junctions. It introduces the double-barrier (SINIS) used later on to analyze the Josephson current as a function of the temperature in nanogap based YBCO-Au-YBCO junctions. In Chapter 5, we look into the growth of c - and a -axis oriented YBCO films on MgO (110) and LSGO (100) substrates, respectively. The quality of the films is checked by scanning electron microscopy (SEM) and atomic force microscopy (AFM) imaging. Chapter 6 is devoted to the description of the fabrication of the devices studied in this thesis. The transport properties of encapsulated YBCO nanowires and the ozone annealing as a powerful tool to recover the oxygen out-diffused YBCO nanostructures are studied in Chapter 7. In Chapter 8, we will discuss the transport properties of our SNS junctions as a function of an external magnetic field, rf-microwave irradiation and of the temperature. In Chapter 9 we investigate the in-plane transport anisotropy of a -axis oriented YBCO nanowires. Chapter 10 is devoted to the conclusions and possible outlook.

This page intentionally left blank.

2

Superconductivity and Cuprates

2.1 INTRODUCTION TO SUPERCONDUCTIVITY

Heike Kamerling Onnes in 1908 after successfully liquefying helium, was able to study the properties of mercury at very low temperatures. He observed a sudden drop of the electrical resistance to a zero value below a characteristic critical temperature, T_C . He named this unexpected phenomenon superconductivity. Later in 1933, Meissner and Oschenfeld²² showed that superconductors are also perfect diamagnets: below T_C , superconductors expel an external applied magnetic field B (if B is below a critical field) from the interior, through the generation of diamagnetic current confined within a distance λ_L , called *London penetration depth*, from the superconductor's surface. Superconductivity can be defined by these two distinct features: perfect conductivity and perfect diamagnetism.

The phenomenon of superconductivity has continued to be an active and promising research field for more than 100 years. As a result, several Nobel prizes in physics have been awarded.

The conventional superconductors are mainly elemental metals and metallic alloys with T_C that doesn't exceed 30 K*. High critical Temperature Superconductors (HTS) are mostly complex compounds sharing "defected" perovskite structures. The T_C can be close to 165 K for mercury based compounds²⁴⁻²⁷. Fig. 2.1 shows the T_C of superconductors versus date of discoveries²⁸.

*MgB₂ with a critical temperature of about 40 K and H₂S with a T_C of 203 K (under high pressure) are believed to be BCS superconductors²³.

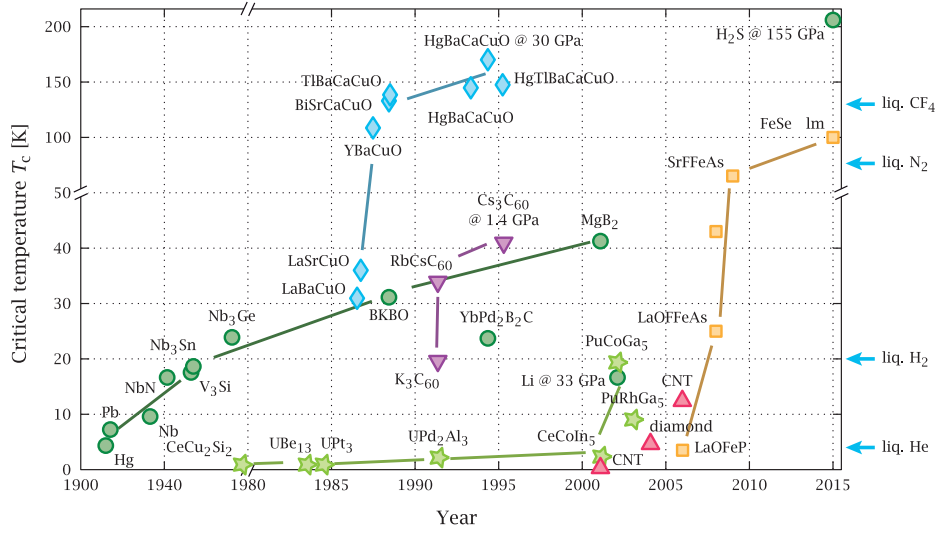


Figure 2.1: The T_C of superconductors versus date of their discovery. The BCS superconductors are marked by green circles. MgB_2 with $T_C = 39$ K has a record for conventional superconductors at ambient pressure. Fe based superconductors (yellow squares)²⁹ with $T_C \approx 100$ K have been discovered more recently³⁰. The cuprates (blue diamonds) are the first superconductors showing T_C above LN₂ temperatures. The Hg-copper oxide superconductors show a T_C of 130 K at ambient pressure and of 164 K under high pressure (blue diamonds)^{24,27}. Unconventional superconductivity (violet down triangles) with $T_C \approx 40$ K found in a molecular Jahn-Teller metal³¹. The Ce- and U-based compounds (light-green stars) showed T_C as big as 20 K³². The record holder (known to date) is Hydrogen sulfide (H_2S) under extremely high pressure with T_C near 203 K^{33,34}. It is a high-Tc superconductor which is believed to be a BCS superconductor.

Fritz and Heinz London³⁵ developed a phenomenological theory for superconductivity based on classical electrodynamics. They used a two-fluid model in which the total current is a sum of two separate components, given by the supercurrent J_s which flows without dissipation and a normal current J_n^\dagger , subject to dissipation. They then related J_s to the electromagnetic field applied to the superconductor. There are two London equations:

$$\frac{\partial \mathbf{J}_s}{\partial t} = \frac{n_s e^{*2}}{m^*} \mathbf{E}, \quad (2.1a)$$

$$\nabla \times \mathbf{J}_s = -\frac{n_s e^{*2}}{m^*} \mathbf{B}. \quad (2.1b)$$

Here n_s is the density of superconducting electrons, m^* and e^* are the mass and electric charge of the superelectrons, respectively.

Eq. 2.1a is called the first London equation and describes the collisionless response of the supercurrent: in presence of an electric field, the superelectrons accelerate, just like an undamped charged particle.

Eq. 2.1b, is called the second London equation and explains the *Meissner effect*. Taking

[†]Basically the normal current is due to the thermally excited unbound electrons the so-called quasi-particles.

the curl of the Maxwell equation (Ampere's law) $\nabla \times \mathbf{B} = \mu_0 \mathbf{J}_s$ and using the second London equation (Eq. 2.1b), we arrive at

$$\nabla^2 \mathbf{B} = \frac{1}{\lambda_L^2} \mathbf{B}, \quad (2.2)$$

where $\lambda_L \equiv \sqrt{\frac{m^*}{\mu_0 n_s e^{*2}}}$ is known as the *London penetration depth*. Eqs. 2.2 and 2.1b imply that the applied magnetic is screened out inside the superconductor by the supercurrent decaying exponentially from the surface with a characteristic decay length given by λ_L .

In 1950, Ginzburg and Landau postulated a phenomenological model to explain the superconducting phenomena based on the second order-disorder phase transition established by Landau. The G-L theory is a mean field theory and extends the London theory by introducing the concept of the macroscopic wavefunction Ψ to describe the phenomenon of superconductivity. In the superconducting state ($T < T_C$) which is the ordered phase, $\Psi \neq 0$, and the order parameter has an amplitude and a phase, while it is zero for temperatures above T_C . Ginzburg and Landau identified that Ψ is related to the superfluid density as

$$\Psi(\mathbf{r}) \equiv |\Psi(\mathbf{r})|e^{i\theta(\mathbf{r})} \equiv \sqrt{n_s(\mathbf{r})}e^{i\theta(\mathbf{r})}, \quad (2.3)$$

where $n_s(\mathbf{r})$ is the density of superconducting electrons and $\theta(\mathbf{r})$ is the phase of the order parameter. In the G-L theory, the free energy of a superconductor can be expressed in powers of Ψ and $\nabla\Psi$ as

$$F - F_n = \alpha|\Psi|^2 + \frac{\beta}{2}|\Psi|^4 + \frac{1}{2m^*}|(-i\hbar\nabla + q^*\mathbf{A})\Psi|^2 + \frac{\mathbf{B}^2}{2\mu_0}. \quad (2.4)$$

Here the F_n is the free energy of the normal phase, \mathbf{A} is the magnetic vector potential, m^* and q^* are the superconducting electron mass and charge, respectively, α and β are temperature dependent Ginzburg-Landau coefficients³⁶.

By minimizing the free energy, Eq. 2.4, with respect to the wavefunction Ψ we obtain the G-L equation

$$\alpha|\Psi| + \beta|\Psi|^2 + \frac{1}{2m^*}(-i\hbar\nabla + q^*\mathbf{A})^2\Psi = 0. \quad (2.5)$$

Eq. 2.5 is a differential equation for Ψ which is analogous to a Schrödinger equation for a free particle but with a nonlinear term.

Similarly, by minimizing the free energy, Eq. 2.4, with respect to the vector potential, \mathbf{A} , one gets the expression for the diamagnetic supercurrent

$$\mathbf{J}_s = \frac{-i\hbar q^*}{2m^*}(\Psi^*\nabla\Psi - \Psi\nabla\Psi^*) - \frac{q^{*2}}{m^*}\mathbf{A}|\Psi|^2 = q^*|\Psi|^2\mathbf{v}_s, \quad (2.6)$$

if one identifies

$$\mathbf{v}_s = \frac{\hbar \nabla \phi - q^* \mathbf{A}}{m^*}, \quad (2.7)$$

as the velocity of the superelectrons.

The G-L Eqs. 2.5 and 2.6 account for the variation of the superelectron density and supercurrent density in presence of a magnetic field. They represent therefore an extension of the London equations.

The identification of the microscopic origin of superconductivity is strictly linked to the observation of the isotope effect. In 1950, Fröhlich³⁷ predicted that the superconducting transition temperature is a function of isotope effect parameter α as $T_C \propto M^{-\alpha}$, where M is the isotopic mass³⁸. This suggests that the electron-phonon coupling is related to the superconductivity. Soon after, Maxwell³⁹ and Reynolds et al.⁴⁰ observed that the transition temperature of Hg superconductor was a function of the nuclear mass, the lighter the mass the higher the transition temperature.

A few years later, in 1957, Bardeen, Cooper and Schrieffer⁴¹, came up with a microscopic theory for conventional superconductivity known as BCS theory. According to their model, an electron moving through a lattice of positively charged ions can displace ions and create a local excess of positive charge which attracts the next passing electron. This attraction force is possible since the atoms are much heavier than the electrons and move more slowly. Because of the attractive force an electron with positive spin and momentum at the Fermi energy pairs up with another electron with opposite spin and momentum to form a Cooper pair. Once formed, the Cooper pairs which are bosons, condense in the same ground state. The BCS coherence length $\xi_{\text{BCS}} = \hbar v_f / \pi \Delta_0$ accounts for Cooper pair dimension. Here, v_f is the Fermi velocity, and $\Delta_0 = 3.5 k_B T_C$ is the necessary energy to break a Cooper pair, also known as the *superconducting energy gap*. If ξ is small, the energy cost, Δ_0 , for breaking a Cooper pair is large and vice versa. The condensation of the Cooper pairs in the same quantum state opens up an energy gap Δ_0 in the density of states, around the Fermi energy of the superconductor. The reason that a superconductor has a zero resistance is closely linked to the existence of the energy gap Δ_0 at the Fermi energy. Scattering events which are responsible for the appearance of resistance in a conductor are not allowed since they would break a Cooper pair.

The BCS theory has been proven by several experiments and could explain the superconducting properties of conventional superconductors. However, the BCS theory predicts that, there is a theoretical maximum to the critical temperature which is about 30 K. Above this temperature, the thermal energy would reduce electron-phonon interactions, result high energy states which destroy Cooper pairs.

2.2 SUPERCONDUCTIVITY IN THE HIGH CRITICAL TEMPERATURE CUPRATES

High critical temperature (High- T_C) superconductivity was discovered by K. G. Müller and J. A. Bednorz in 1986²⁸. The first compound was $\text{Ba}_x\text{La}_{5-x}\text{Cu}_5\text{O}_{5(3-y)}$ with critical transition temperature between 30–40 K which overcame the T_C limit predicted by the BCS theory. However, the BCS theory fails to explain the superconductivity in copper-oxide high- T_C superconductors. There are two main reasons: the electron-phonon coupling is not strong enough and there is not a conventional Fermi surface. Soon after, other cuprate families such as $\text{YBa}_2\text{Cu}_3\text{O}_{7-\gamma}$ ($T_C=90$ K), $\text{Bi}_2\text{Sr}_2\text{CaCu}_2\text{O}_{8+x}$ ($T_C = 80-115$ K)⁴² and $\text{Tl}_x\text{Ba}_{y-1}\text{Cu}_y\text{O}_{2y+x+2}$ TBCO ($T_C = 85-125$ K)⁴³ were discovered and among them YBCO remained the most studied high- T_C cuprate.

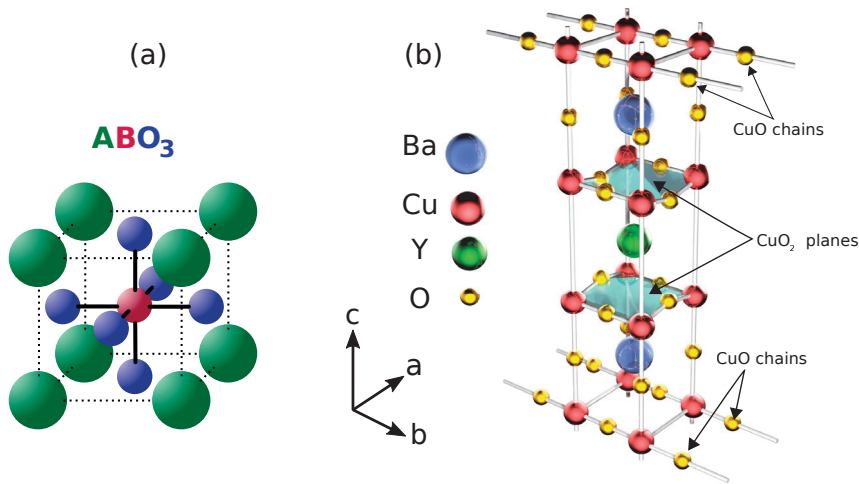


Figure 2.2: (a) The configuration of a perovskite structure is (ABO_3) , where A and B are two cations and O is Oxygen. Perovskites have a cubic unit cell structure and are composed of corner-sharing BO_6 octahedra, with A ions at the corners of the unit cell (adpoted from⁴⁴), (b) schematic representation of a YBCO cell. Each perovskite unit cell consists of a Y and Ba atom at the center. Cu atoms occupy all the corner sites and oxygen atoms are in the middle edge positions.

The crystal structure of YBCO is based on a defected perovskite structure (Fig. 2.2) where 3 blocks are stacked up on the top of each other. The superconductivity mainly occurs in two-dimensional CuO_2 planes that are weakly coupled to each other. These planes arise from the oxygen deficiency at the Y plane, as compared to a perfect perovskite structure. The oxygen atoms at the top and bottom planes of the YBCO cell are missing in a -axis direction giving rise to Cu-O chains. These Cu-O chains act as the charge reservoir and by adding or removing oxygen from the chains one can change the superconductive and normal state properties of YBCO. In the $\text{YBa}_2\text{Cu}_3\text{O}_{7-\gamma}$ formula, for $\gamma = 1$, the compound is an insulator with a tetragonal structure. By adding oxygen to the chains γ decreases and YBCO becomes superconducting with a T_C which depends on the oxygen stoichiometry. The superconducting YBCO is orthorhombic with lattice

parameters: $a \approx 3.82 \text{ \AA}$, $b \approx 3.89 \text{ \AA}$ and $c \approx 11 \text{ \AA}$ at the optimal doping^{45,46}. Varying the oxygen content of $\text{YBa}_2\text{Cu}_3\text{O}_{7-\gamma}$ results in significant changes of its physical properties such as its crystal structure and T_C .

2.2.1 PHASE DIAGRAM

As mentioned in the previous section, the transport properties of cuprates are drastically altered by changing the hole concentration p in the CuO_2 planes, which can be varied by adding or removing oxygen atoms in Cu-O chains. Depending on p , YBCO goes from an antiferromagnetic Mott insulator to superconductor and then to Fermi metal. Fig. 2.3 shows the phase diagram of YBCO as a function of the temperature T and the hole concentration p which addresses the hole per planar Cu atom.

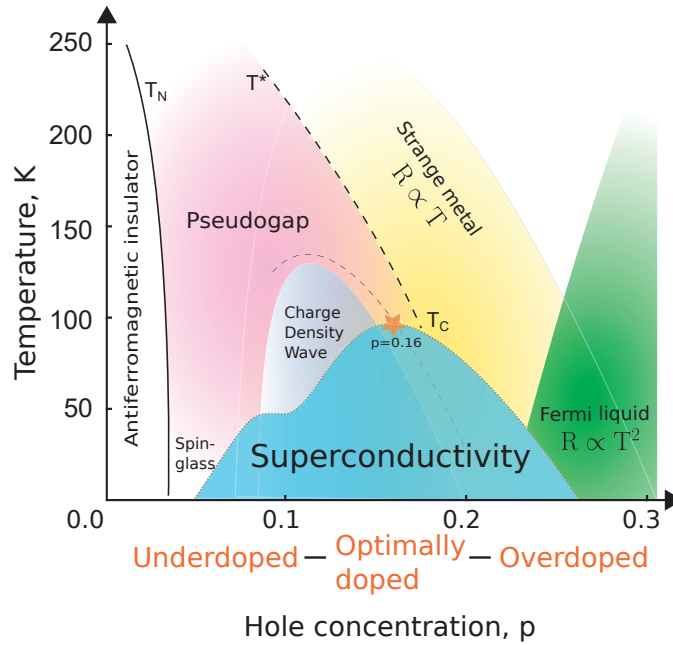


Figure 2.3: Phase diagram of the YBCO as a function of the temperature and the hole doping p . The undoped YBCO with $p = 0$, is an antiferromagnetic insulator as a consequence of strong correlation effects. Upon doping with hole, the YBCO becomes superconducting for $T < T_C$. In the under-doped or pseudogap region ($p = 0.16$), there is a significant suppression of the electron density of states in the normal state. Moreover, in the same region of the phase diagram, it is proved that there are various forms of ordering such as charge density wave (CDW) and spin density wave (SDW). By further increasing the doping, close to the optimal doping and for $T > T_C$ YBCO behaves differently from a normal metal and is addressed as "strange" metal. In this region, the resistivity increases linearly with temperature ($R \propto T$). Finally, the region with $p > 0.16$ called overdoped region YBCO can be described as a Fermi liquid model and the resistance is a quadratic function of temperature ($R \propto T^2$).

At very low doping, $p \approx 0$, and below the Néel temperature, $T_N = 400 \text{ K}$, YBCO is not a metal (as one would expect from the band theory) but it is an antiferromag-

netic insulator (AFI) or Mott insulator with the spins of adjacent Cu atoms pointing in opposite direction. The insulating behavior at very low doping is mostly due to the strong electron correlation leading to the localization of the charge carriers on each atomic site. However, upon small hole-doping ($p = 0.05$), this antiferromagnetic phase vanishes quickly and superconductivity as well as other interesting properties emerge⁴⁷. Superconductivity occurs only over a limited range of p (dome-like shape in the phase diagram). Depending on the doping level, the superconducting region can be divided into three parts namely the *underdoped*, *optimally-doped*, and *overdoped* regions:

- **Underdoped region** ($p < 0.16$): here a pseudogap phase in the normal region appears. It is one of the least understood features of the phase diagram; the properties of the YBCO in the normal region are very unconventional. The main signature is the presence of a pseudogap, namely a suppression of electronic density of states near the Fermi energy at a temperature T^* , which is well above the T_C . T^* reduces by increasing the doping.

The pseudogap has been measured with a number of techniques like Angle-resolved photoemission spectroscopy (ARPES)⁴⁸ and tunneling spectroscopy⁴⁹. Fig. 2.4 shows the tunneling spectra of $\text{Bi}_2\text{Sr}_2\text{CaCu}_2\text{O}_{6+\delta}$ (Bi2212) with $T_C = 83\text{ K}$ as a function of temperature. A gap-like feature survives at temperature well above the superconducting transition.

The possible mechanisms leading to the pseudogap are not clearly understood^{50–53}. There are some speculations that the observation of short-range charge density wave (CDW) correlation above (and below) T_C could be the answer to the origin of the pseudogap^{54,55}.

Recently, Lee⁵⁶ promoted a theory called *amperean pairing* to explain the pseudogap phase. In his theory, he considered that the pseudogap phase can be associated to Cooper pairs with a net momentum but without any phase coherence. The most credited theory for the pseudogap is that of Varma⁵⁷, where loop currents at the corners of the Cu atoms in the a - b planes are responsible for the unconventional behaviors.

- **The optimally-doped region** ($p = 0.16$) is defined when the superconducting transition temperature T_C reaches its maximum. Near the optimal doping, at temperature above the T_C , YBCO behaves like a strange metal phase. Transport measurements revealed that over the accessible temperature range up to 1000 K, the resistivity is linear in temperature instead of a quadratic dependence expected from the electron scattering model.

- **The overdoped region** ($p > 0.16$) can be explained based on a Fermi liquid physic. Although the heavily hole-doped cuprates show a large Fermi surface volume, the pairing model based on the phonon interactions can not unambiguously elucidate the superconductive mechanism in cuprates.

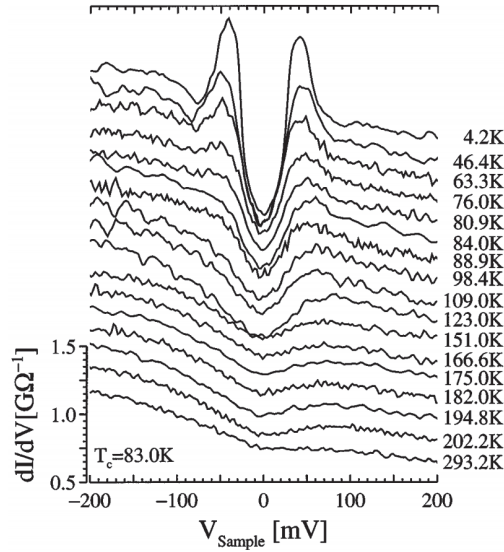


Figure 2.4: Tunneling spectra measured as a function of temperature on underdoped Bi2212. The conductance scale corresponds to the 293 K spectrum⁴⁹.

Table 2.1: Summary of superconducting properties of optimally doped YBCO single crystal and thin film. For comparison, the superconducting properties of some common conventional superconductors are listed⁵⁸⁻⁶⁰.

Material	$T_C(K)$	$\Delta(\text{meV})$	$\lambda_L(\text{nm})$	$\xi(\text{nm})$	$H_{c2}(\text{T})$
YBCO	91	20 – 25	$\lambda_a = 150 - 300$ $\lambda_c = 1000$	$\xi_{a-b} = 1 - 3$ $\xi_c = 0.24$	$H_{c2}^{a-b} = 250$ $H_{c2}^c = 120$
Al	1.18	0.2	50	1600	0.01
Nb	9.25	1.5	44	40	≈ 3
NbN	16.1	1.5	≈ 200	≈ 5	≈ 20

2.2.2 SUPERCONDUCTING ORDER PARAMETER SYMMETRY

As shown in Fig. 2.2(b), the YBCO unit cell is highly anisotropic which has consequences on physical properties such as the effective mass, coherence length and London penetration depth in the $a - b$ plane and the c -axis directions. For example, the effective mass of the electrons moving in the $a - b$ plane, m_{ab} , is different from that in the c -axis direction, m_c . One can introduce an anisotropy parameter $\gamma = \sqrt{m_c/m_{a-b}}$ which depends on the doping. Table. 2.1 summarizes the values of characteristic lengths (λ_L and ξ) in the $a-b$ planes and along the c -axis direction. By comparing with conventional superconductors, YBCO has smaller coherence length ξ , longer London penetration depth λ_L and larger superconducting energy gap Δ .

The knowledge of the symmetry of the order parameter is extremely important for understanding the superconducting mechanism. The conventional superconductors, with electron-phonon interaction, have an order parameter (superconducting gap) that

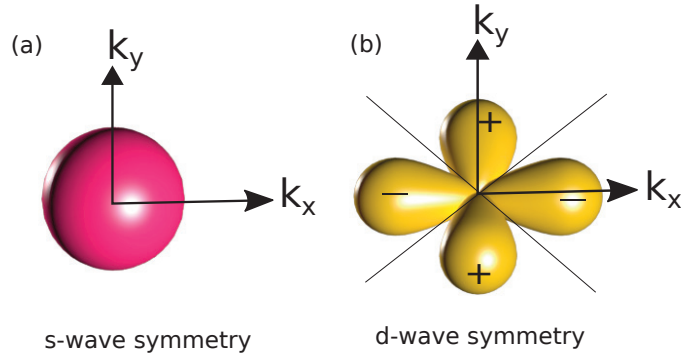


Figure 2.5: The pairing symmetry in (a) conventional superconductors with an s-type symmetry have uniform phase and amplitude. The s-wave superconductors have singlet spin state with orbital component of $l=0$, (b) cuprates with anisotropic $d_{x^2+y^2}$ order parameter have nodes, where the amplitude goes to 0 and the phase changes by π . The d-wave superconductors have singlet spin state with orbital component of $l=2$.

is isotropic in all directions with s-wave symmetry (see Fig. 2.5(a)), while for high-Tc superconductors including cuprates it is widely accepted that the order parameter symmetry is d-wave. In the momentum space, the $d_{x^2-y^2}$ order parameter can be characterized by four lobes separated by nodes where the gap is fully suppressed⁶¹ (see Fig. 2.5(b)). Moreover, the phase of the superconducting gap switches sign at the boundary between the lobes.

Different experiments like Josephson Interferometry⁶², vortices at tri-crystal boundaries⁶³ and ARPES measurement⁶⁴ convinced scientists that the pairing symmetry of HTS cuprate is d-wave. The d-wave order parameter in k-space can be expressed as

$$\Delta(\mathbf{k}) = \Delta_0[\cos k_x a - \cos k_y a]. \quad (2.8)$$

However, in recent studies by Gustafsson et al.⁶⁵ there are evidences that show deviation from a pure d-wave symmetry while supporting the appearance of a small subdominant imaginary component $i\delta$ which adds to the main $d_{x^2-y^2}$ component.

This page intentionally left blank.

3

Josephson junctions

3.1 JOSEPHSON EFFECT

A Josephson junction (JJ) is formed with two superconducting electrodes which are weakly coupled. The weak link can be an insulator, a normal metal, a geometrical constriction, a semiconductor, or a superconductor with lower critical temperature T'_C . Josephson⁶⁶ in 1962 predicated that Cooper-pairs can tunnel through a very thin insulating layer without any dissipation (see Fig. 3.1). This prediction was experimentally confirmed soon after⁶⁷.

The behavior of Cooper pairs in the superconducting electrodes on both sides of the barrier is described by a single wavefunction $\Psi_L = |\Psi_L|e^{i\theta_L}$ and $\Psi_R = |\Psi_R|e^{i\theta_R}$. Here, θ_R and θ_L are the phases of the superconducting order parameter in the electrodes on the right R and on the left L side of the barrier, respectively. Due to the small thickness of the barrier, the wavefunctions of the two superconducting electrodes overlap, allowing the coherent tunneling of Cooper pairs. For tunnel junctions, the amplitude of the Cooper pair current is related to the phase difference between the two electrodes $\varphi = \theta_R - \theta_L$ by the expression

$$I = I_C \sin \varphi. \quad (3.1)$$

Here, I_C is the critical current, that is the maximum supercurrent the junction can sustain without dissipation and is proportional to the transparency of the barrier and the superconducting gap of the electrodes⁶⁶. Eq. 3.1 describes the *DC Josephson effect*

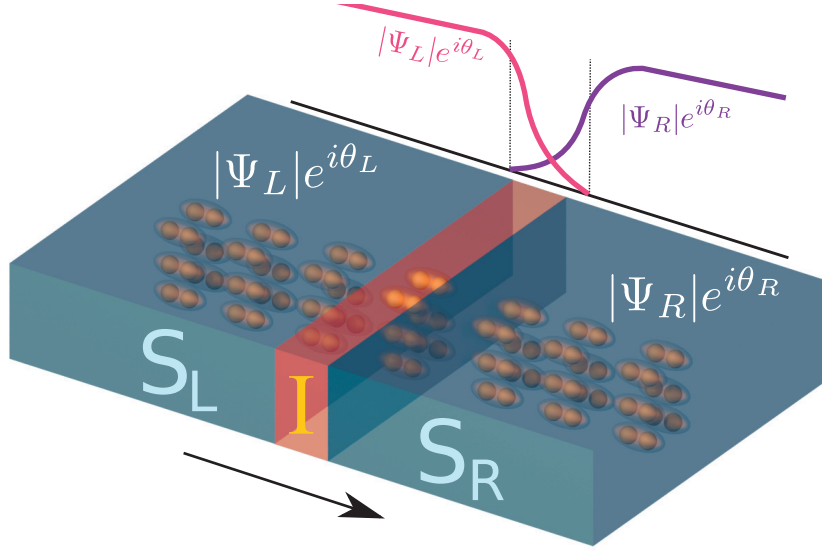


Figure 3.1: Sketch of a Josephson junction. Cooper pairs can tunnel through the barrier. The wavefunction of the superconductor on the left overlaps with the wavefunction of the superconductor on the right allowing coherent Cooper pair tunneling.

and is the commonly used current-phase relation (CPR) to describe ordinary tunnel Josephson junctions.

For two identical electrodes, the temperature dependence of I_C is given by the Ambegaokar-Baratoff (AB) relation ^{*68}

$$I_C(\varphi) = \frac{\pi\Delta(T)}{2eR_N} \tanh \frac{\Delta(T)}{2k_B T}. \quad (3.2)$$

where R_N and $\Delta(T)$ are normal state resistance and superconducting energy gap, respectively.

Josephson ⁶⁶ also found that when voltage biasing a JJ, the phase difference changes over barrier according to

$$V = \frac{\hbar}{2e} \frac{d\varphi}{dt}, \quad (3.3)$$

where e is the electron charge. Eq. 3.3 is also known as the *AC Josephson effect*. The phase difference in a Josephson junction grows linearly in time as

$$\varphi(t) = \frac{2e}{\hbar} V t + \varphi_0 = \omega_J t + \varphi_0^\dagger, \quad (3.4)$$

^{*}The AB relation is valid in tunnel junctions (i.e. SIS junctions with an insulating barrier).

[†]Here, we assumed a constant DC voltage V .

where $\omega_J = 2eV/\hbar$ is the *Josephson frequency*

$$f_J = \frac{\omega_J}{2\pi} = \frac{2eV}{h} = \frac{V}{\Phi_0} \approx V \times 483.6 \frac{\text{MHz}}{\mu\text{V}}, \quad (3.5)$$

and $\Phi_0 = \frac{h}{2e}$ is the flux quantum. The AC Josephson effect links the voltage to frequency only through fundamental constants, therefore it can be used as a voltage standard.

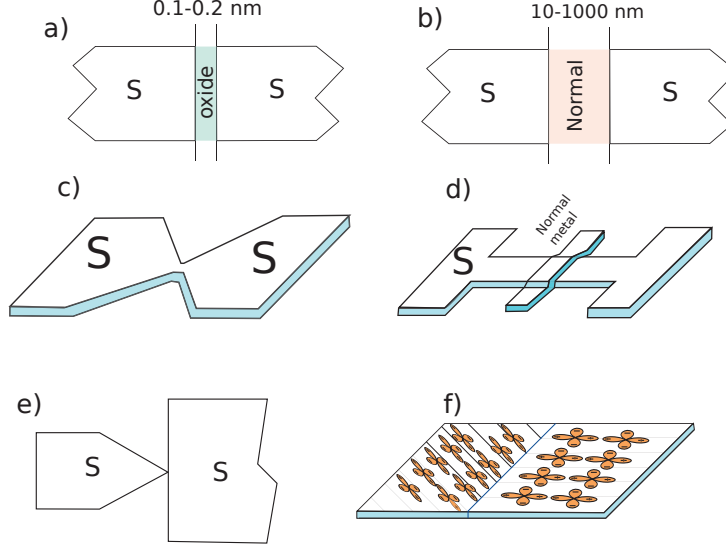


Figure 3.2: Common types of Josephson contacts a) Oxide layer; b) SNS- contact; c) constriction; d) Double layer contact via Proximity effects; e) point contact, f) Grain boundary junction.

The stored energy in a Josephson junction is given by

$$E_J = \int_0^t IV dt = \frac{\hbar I_C}{2e} (1 - \cos \varphi) = E_{J_0} (1 - \cos \varphi). \quad (3.6)$$

Here, the $E_{J_0} = \frac{\hbar I_C}{2e}$ is called the Josephson coupling energy. The CPR of a Josephson junction can be described through its Josephson energy via $I(\varphi) = \frac{2\pi}{\Phi_0} \frac{dE_J}{d\varphi}$.

Fig. 3.2 shows some possible experimental realizations of Josephson junctions, for example using a normal barrier (Fig. 3.2(b)) or a micro-constriction (Fig. 3.2(c) and 3.2(e)). In Eq. 3.1, the CPR for a tunnel barrier is sinusoidal. Nevertheless, this is not the case for all types of Josephson junctions. For example, it has been shown that the CPR can be strongly non-sinusoidal in superconducting point contacts and in diffusive SNS junctions^{69,70} ‡.

‡Note that the equilibrium CPR for all kinds of Josephson junctions have been found to be entirely sinusoidal at temperatures close to T_C . The CPR becomes less and less sinusoidal at low temperatures.

3.1.1 SUPERCONDUCTING NARROW BRIDGES

Among the types of weak links presented in Fig. 3.2, we will concentrate on superconducting narrow bridges in which a superconducting nanowire having length l , width w and thickness t bridges two superconducting electrodes.

Aslamazov and Larkin (AL)^{69,71} have generalized Eq. 3.1 for a nano-constriction (see Fig. 3.2(C)) for temperatures close to the critical temperature ($T \approx T_C$) in the case of a sufficiently short ($l \ll \xi$) and narrow ($w, t \ll \xi$) bridge. The AL current-phase relation is given by

$$J_s(\varphi) = \frac{\Phi_0}{2\pi\mu_0\lambda_L^2 l} \sin \varphi, \quad (3.7)$$

where Φ_0 is the flux quantum, μ_0 is the vacuum permeability and λ_L is the London penetration depth.

In a long wire limit, Likharev and Yakobson (LY)⁷¹ predicted that, by increasing the length l the CPR of the nanowire evolves from sinusoidal to a slanted sinusoidal and eventually becomes multi-valued at $l \geq 3.6\xi$ which is strongly connected to the depairing effect (see Fig. 3.3⁷²). Such a length dependence of the CPR is experimentally studied by Pei et al.⁷³. In fact, the maximum current saturates for $l > 10\xi$ to a value given by the depairing current density, above which the superconductivity is locally suppressed inside the bridge (assuming rigid-boundary condition) due to the phase slippage of the superconducting order parameter in the structure.

Considering the limit of a long ($l \gg \xi$) and one dimensional ($w, t \ll \xi$ and $wt \ll \lambda^2$) bridge, the free energy can be written as

$$F = F_n + \alpha|\Psi|^2 + \frac{\beta}{2}|\Psi|^4 + \frac{1}{2}m^*v_s^2|\Psi|^2, \quad (3.8)$$

where v_s is the Cooper pair velocity, defined from $J_s = e^*|\Psi|^2v_s$. The condition $w, t \ll \xi$ allows us to keep $\Psi(\mathbf{r}) = |\Psi|\exp(i\theta(\mathbf{r}))$ constant across the cross section of the superconductor and the limit $wt \ll \lambda^2$ means that the self magnetic field can be neglected. Likharev & Yakobson⁷¹ defined the order parameter inside the wire as

$$\Psi^{LY}(x) = |\Psi^{LY}| \exp(i\frac{x}{l}\varphi), \quad (3.9)$$

where φ is the phase difference between two ends of the wire. Consequently they obtained the modulus of the wavefunction by minimizing the Eq. 3.8 for a given v_s

$$|\Psi^{LY}|^2 = |\Psi_\infty^{LY}|^2 \left[1 - \left(\frac{\varphi\xi}{l}\right)^2 \right], \quad (3.10)$$

where $|\Psi_\infty^{LY}|$ is the wavefunction when the phase difference is zero. Finally by inserting the Eq. 3.9 and 3.10 into the GL critical current density relation (Eq. 2.6), they determined the CPR for the long one-dimensional bridge

$$J_s(\varphi) = \frac{\Phi_0}{2\pi\mu_0\lambda_L^2\xi} \left[\left(\frac{\xi}{l}\right)\varphi - \left(\frac{\xi}{l}\right)^3\varphi^3 \right]. \quad (3.11)$$

Minimizing the Likharev-Yakobson CPR, Eq. 3.11, with respect to φ/l , determines a critical value for the phase $\varphi_d = l/\sqrt{3}\xi$. The depairing critical current density can be achieved by substituting φ_d into Eq. 3.11 which gives the expression

$$J_d = \frac{\Phi_0}{3\sqrt{3}\pi\mu_0\lambda_L^2\xi}. \quad (3.12)$$

Therefore, by increasing the junction's length, we have transition from the Josephson effect to the depairing limit.

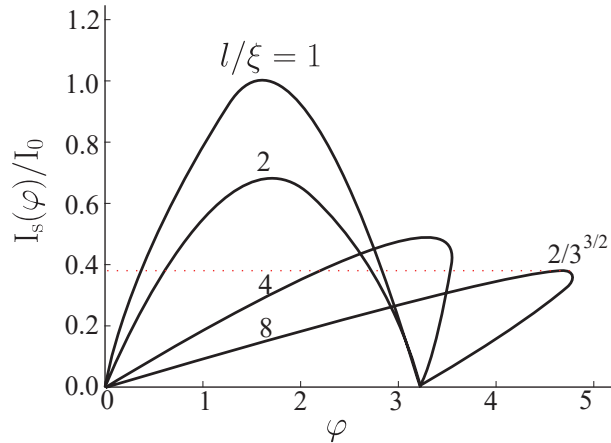


Figure 3.3: Variation of the current-phase relation with the length of a weak link at $T \leq T_C'$. Here, the currents are normalized to $I_0 = \Phi_0/2\pi\mu_0\lambda_L^2\xi$. Adapted from⁷¹.

3.2 FLUCTUATION MECHANISMS IN SUPERCONDUCTORS

Likharev⁷¹ showed that for a weak-link with $w < 4.44\xi$ and $l > 3.49\xi$ there is a regime in which fluctuation may stimulate the phase-slips centers[§], either thermally or quantum mechanically.

[§]In a superconducting nanowire, a phase-slip event occurs when the phase difference over the wire slips by a value of 2π and the magnitude of the order parameter oscillates between zero and its maximum value. First proposed by Little⁷⁴, a phase slip by thermal activation is responsible for a resistive tail-like behavior in the resistance-temperature characteristic of a nanowire for $T < T_C$.

In the case of wide wires, $w > 4.44\xi$ Bulaevskii et al.⁷⁵ showed that Abrikosov vortices can penetrate inside the structure. The current can be considered homogeneous if $t < \lambda_L$ and $w < \Lambda = \lambda_L^2/t$, (where Λ is the *Pearl length*) and the G-L equation reduces to one dimensional form⁷⁶. As a result, one can consider the same CPR as Eq. 3.11, with the difference that the maximum current density is given by Abrikosov vortices crossing the wire, and not by the depairing current. This happens at $\varphi_v = l/2.71\xi \cong 0.64\varphi_d$ ⁷⁵ and the critical current density J_v is smaller than the depairing critical current ($J_v \cong 0.826 J_d$).

Following Ref.⁷⁵ and considering also the contribution of the vortex core energy^{77,78}, the maximum of vortex entry potential can be obtained by

$$U_{max} = \mu^2 \epsilon_0(T) \ln \frac{1.47w}{\pi\xi(T)}, \quad (3.13)$$

where $\epsilon_B(T) = \Phi_0^2 t / 4\pi\mu_0 \lambda^2(T)$ is the characteristic energy in the thin film, ξ is the coherence length, w is the width of the wire and $\mu^2 = |\Psi|^2 / |\Psi_\infty|^2$ is the order parameter suppression due to the bias current and is equal to 1 in zero bias limit.

As shown in Fig. 3.4 the Lorentz force induced by the bias current \mathbf{I}_b [¶] and the vortex field \mathbf{B} , move the vortex which results in a voltage transient.

The resistance of the wire affected by the vortex entry below the T_C is given by^{79,80}

$$R(T) = R_\square \sqrt{2\pi} (1 + \pi) \frac{l\xi}{w^2} \left(\mu^2 \frac{\epsilon_B(T)}{k_B T} \right)^{\frac{3}{2}} \exp\left(-\frac{U_{max}}{k_B T}\right), \quad (3.14)$$

where l is the length of the wire and R_\square is the sheet resistance of the nanowire at a temperature slightly above T_C . Here, according to Eqs. 3.13 and 3.14, by increasing the temperature or reducing the junction's width w , the energy barrier for the vortex entry inside the superconductor is reduced and the probability for a vortex to overcome the barrier increases.

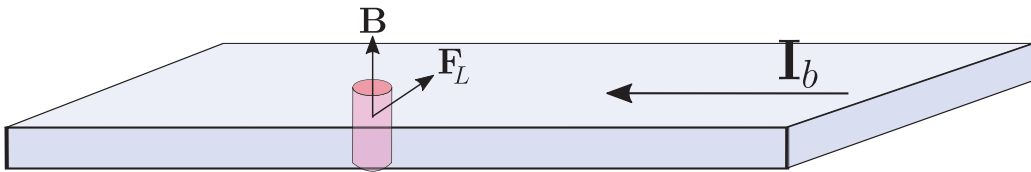


Figure 3.4: A superconducting nanowire of width w , carrying the bias current \mathbf{I}_b which exerts the Lorentz force \mathbf{F}_L on a vortex.

[¶]Here we considered the homogeneous current flow in the nanowire which is equivalent to $w.t \ll \lambda^2$.

3.3 JOSEPHSON JUNCTION IN A MAGNETIC FIELD

One of the most striking feature of a Josephson junction is its behavior when it is placed in an external magnetic field. Consider a sandwich-type Josephson junction, with a barrier thickness d , superconducting electrode thickness t and an area A , which is positioned in the middle of the yz plane and carrying current along the x axis direction. (see Fig. 3.6(a)). An external magnetic field B is applied in the plane of the Josephson junction (y direction). The applied magnetic field results in a spatial modulation of the phase differences φ along the barrier as⁸¹

$$\frac{\partial\varphi}{\partial z} = \frac{Bd_{\text{eff}}}{\Phi_0/2\pi}, \quad (3.15)$$

where $d_{\text{eff}} = \lambda_1 + \lambda_2 + d$ is the magnetic thickness and equals to the sum of the barrier thickness d and the London penetration depth of the superconductors, λ_1 and λ_2 .

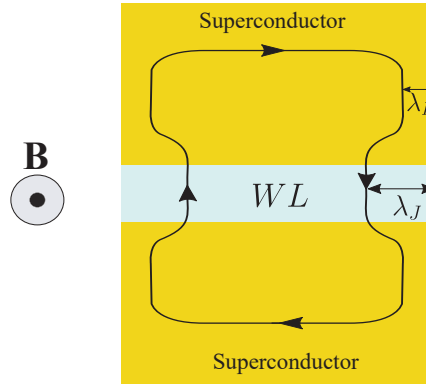


Figure 3.5: Josephson junction in an external magnetic field B . The field can enter the weak link over a distance called Josephson penetration depth λ_J where this screening current will flow.

In sandwich-type junctions where the film's thickness t is larger than the London penetration depth λ_L , the magnetic field penetrates a distance λ_J inside the barrier which is called Josephson penetration depth (see Fig. 3.5) and is given by

$$\lambda_J = \sqrt{\frac{\Phi_0}{4\pi\mu_0 J_C \lambda_L}}, \quad (3.16)$$

where μ_0 is vacuum permeability, J_C is the critical current density of the junction, and λ_L is the London penetration depths of the electrodes. λ_J also represents the length scale where the variation of the phase difference along the junction width occurs.

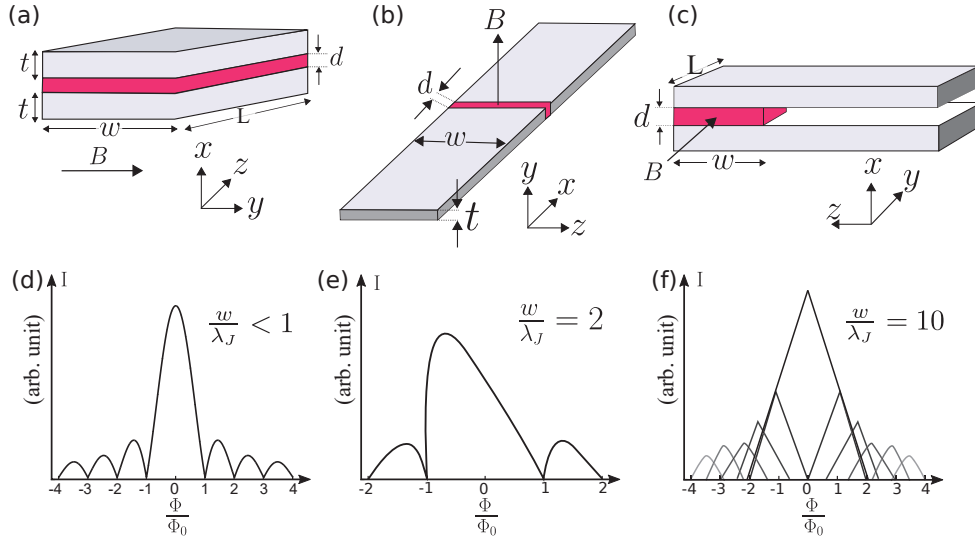


Figure 3.6: The geometry of (a) sandwich-type (b) planar type, (c) in-line Josephson junction. (d) The $I_C(B)$ of a short Josephson junction ($w < \lambda_J$) with uniform supercurrent density yields the well-known Fraunhofer diffraction pattern with a central lobe of width $2\Phi_0$ and side lobes of width Φ_0 , (e) due to the geometry of the long in-line junction with $w/\lambda_J = 2$ (Fig. 3.6(c)), the magnetic field generated by currents flowing in the electrodes (self-field) causes that the maximum of the $I_C(B)$ is shifted to a finite value (adopted from⁸²). (f) the self-field in a very long sandwich-like junction is reflected by a linear decrease of I_C with an externally applied magnetic field (adopted from⁸³).

In a planar junction (see Fig. 3.6(b)), the junction area is formed at the edge between two superconductors and the magnetic field is applied perpendicular to the film surface. In the case that the film's thickness is comparable with or less than the London penetration length, one needs to introduce an effective London penetration depth, $\Lambda = \lambda_L^2/t$ so-called the Pearl length⁷⁶ to determine the length where the magnetic field penetrates inside the superconductor. In this limit, the characteristic length l_J governing the spatial variation of the Josephson phase difference along the junction is given by⁸⁴

$$l_J = \frac{\lambda_J^2}{\Lambda} = \frac{\Phi_0}{4\pi\mu_0\lambda_L^2 J_C}. \quad (3.17)$$

The variation in phase, Eq. 3.15, manifests in the oscillation of the maximum supercurrent through the junction as a function of the applied field. It turns out that for a short ($w < \lambda_J$) sandwich or in-line Josephson junction with a uniform critical current density within the junction, the dependence of the critical current on the external magnetic field is given by a Fraunhofer diffraction pattern (see Fig. 3.6):

$$I_C(\Phi) = I_{C,\max} \frac{|\sin(\pi\Phi/\Phi_0)|}{|\pi\Phi/\Phi_0|}, \quad (3.18)$$

where $\Phi = Bwd_{\text{eff}}^{\parallel}$ is the total magnetic flux through the junction area, Φ_0 is the magnetic flux quantum and $I_{C,\text{max}}$ is the maximum critical current at zero magnetic field. The resulting $I_C(\Phi)$ modulation given in Eq. 3.18 is geometry independent and is valid for all kinds of Josephson junctions (shown in Fig. 3.6(a-c)). The Fraunhofer-like pattern has a magnetic flux periodicity of Φ_0 for junctions with $w < \lambda_J$. The magnetic field periodicity ΔB of a junction with $t \gg \lambda_L$ depends on its width w and magnetic thickness as

$$\Delta B = \frac{\Phi_0}{wd_{\text{eff}}}. \quad (3.19)$$

The examination of the Fraunhofer pattern is a powerful approach to study the behavior and the quality of the Josephson junction. Deviation from Fraunhofer-like pattern is expected for a non-uniform distribution of the critical current density across the junction^{85,86}. Thus, the measurements of the Fraunhofer-like pattern is a proper way to assess the homogeneity of the Josephson current.

The Eq. 3.18 holds only for short Josephson junctions where $w \leq \lambda_J$ when the magnetic fields generated by the supercurrent are neglected. However, if the dimensions of the Josephson junction exceed λ_J (or l_J in the case of a planar junction) the Josephson current can also produce a magnetic field (self-field) that affects the behavior of the magnetic field response of the Josephson current^{81,83,87,88}. Yamashita and Onodera⁸² studied the effect of the self-field on the magnetic field dependence of the critical current for a long in-line ($w > \lambda_J$) junction (Fig. 3.6(c)). They found that the self magnetic field of the junction produces a shift in the maxima of the magnetic field pattern (see Fig. 3.6(e)).

Later, Owen and Scalapino⁸³ performed a numerical calculation to compute the $I_C(\Phi)$ for a very long junction. As shown in Fig. 3.6(f), the critical current of the very long junction with $w = 10\lambda_J$ alters with magnetic field in a linear manner. This is a direct consequence of the Meissner effect in the junction which is a characteristic of a long junction with $w > 5\lambda_J$.

In the case of a narrow planar Josephson junction, Fig. 3.6(b), the field dependence of the critical current can be still approximated by Eq. 3.18^{84,89-93} where the magnetic periodicity ΔB is given by⁸⁹

$$\Delta B \approx \frac{\Phi_0}{w^2/1.84 + w.d} \approx \frac{\Phi_0}{w^2/1.84}. \quad (3.20)$$

Hence, the effective area of the narrow planar Josephson junctions scales as w^2 in contrast to the wd_{eff} dependence of sandwich-type Josephson junctions.

^{||}This relation for the magnetic flux is only valid for the sandwich-like Josephson junction.

3.4 THE RESISTIVELY AND CAPACITIVELY SHUNTED JUNCTION (RCSJ JUNCTION)

As mentioned in Section. 3.1, the behavior of a Josephson junction can be described in terms of the phase difference across the junction φ as following:

$$I = I_C \sin \varphi, \quad (3.21a)$$

$$V = \frac{\Phi_0}{2\pi} \frac{d\varphi}{dt}. \quad (3.21b)$$

An equivalent circuit for a Josephson junction can be used to gain more insight into the dynamic of the system. A Josephson junction can be sketched as the parallel of three circuits elements (see Fig. 3.7):

- **Resistor:** due to quasiparticle conduction through the barrier. The value of R will be close to the normal state resistance R_N at temperature slightly above T_C .

- **Capacitor:** due to the physical structure of the junction we consider a capacitance C forming between the two superconducting electrodes across the weaklink.

- **Non-linear inductor:** due to a supercurrent through the barrier (Josephson effect), the junction can be described by a non-linear inductance $L_J = \hbar/2eI_C \cos \varphi$.

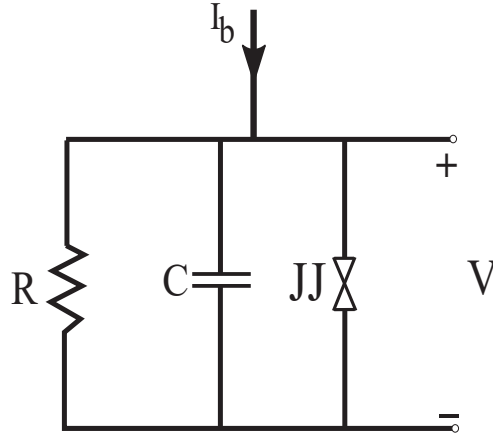


Figure 3.7: The schematic representation of Resistively and Capacitively Shunted Junction (RCSJ) equivalent circuit of a Josephson junction. The resistance R is taken to be the normal resistance of the junction. The capacitor C is due to the physical structure of the junction. For example, in a SIS junction, the capacitance C represents a parallel plate capacitor. The Josephson element is characterized by a variable Josephson inductance $L_J = \hbar/2eI_C \cos \varphi$.

These three circuit elements characterize the resistively and capacitively shunted junction (RCSJ) model^{94,95} (see Fig. 3.7). By applying the Kirchhoff's laws to the

RCSJ equivalent circuit (Fig. 3.7) and using the Eq. 3.21, we have:

$$I_b = C \frac{dV}{dt} + \frac{V}{R} + I_C \sin \varphi = \frac{\Phi_0}{2\pi} C \frac{d^2\varphi}{dt^2} + \frac{\Phi_0}{2\pi} \frac{1}{R} \frac{d\varphi}{dt} + I_C \sin \varphi. \quad (3.22)$$

We can interpret the Eq. 3.22 as that of a phase particle with mass $M \propto C$ and damping $\eta \propto 1/R$ in the potential U :

$$\frac{M d^2x}{dt^2} + \eta \frac{dx}{dt} + \nabla U = 0, \quad (3.23)$$

where

$$M = \left(\frac{\Phi_0}{2\pi}\right)^2 C, \quad (3.24a)$$

$$\eta = \left(\frac{\Phi_0}{2\pi}\right)^2 \frac{1}{R}, \quad (3.24b)$$

$$U = E_{J_0}[-\cos \varphi - i\varphi]. \quad (3.24c)$$

The potential U is the tilted washboard potential where the tilt is given by the bias current (see Fig. 3.8). For simplicity, one can use a normalized current $i = I_b/I_C$, a normalized time $\tau = \Phi_0 t / 2\pi R I_C$, the Stewart-McCumber parameter⁹⁵ $\beta_C = 2\pi I_C R^2 C / \Phi_0$ and rewrite the Eq. 3.22 in the form

$$\beta_C \frac{d^2\varphi}{d\tau^2} + \frac{d\varphi}{d\tau} + \sin \varphi - i = 0 \quad (3.25)$$

Depending on the capacitance C and the resistance R , the junction can be either over-damped $\beta_C \ll 1$, or under-damped $\beta_C \gg 1$.

Let's first consider the case of a over-damped junction ($\beta_C \ll 1$). When the bias current I_b is smaller than I_C , the junction is in the superconducting state and the average voltage across the junction is zero. This state can be seen as a particle sitting in a local minimum of the washboard potential (Fig. 3.8(a)). If the bias current reaches the critical current $I_b \approx I_C$ the phase particle is no longer trapped inside the potential well and can move smoothly down the washboard potential and the junction switches to the voltage state. By further increasing I_b , the voltage drop increases and for $I_b \gg I_C$ the junction behaves like a normal resistor described by the Ohm's law. Indeed for $I_b \gg I_C$ the washboard potential is close to a straight line and the contribution of the AC Josephson effect is vanishingly small.

To stop the phase particle motion, we need to reduce the bias current: once I_b reaches I_C , the phase particle gets trapped in the potential well. The current-voltage characteristics (IVC) of an overdamped Josephson junction is depicted in Fig. 3.8(b). The IVC for an overdamped junction is not hysteretic and is described by the relation³⁶ $V = R(I^2 - I_C^2)^{1/2}$.

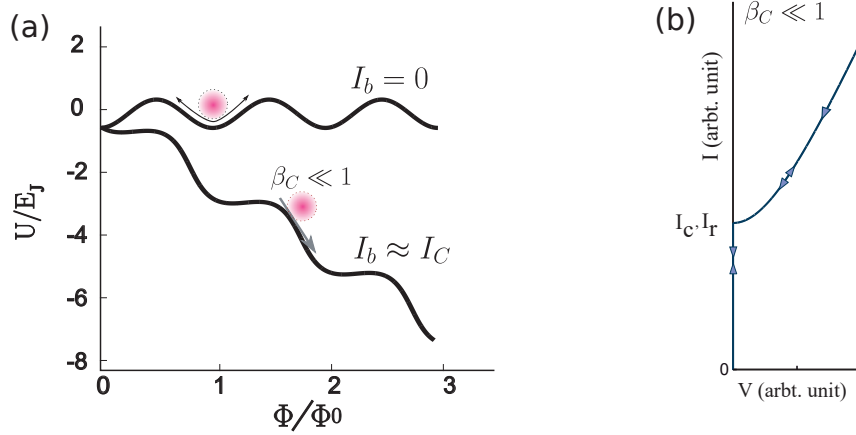


Figure 3.8: (a) Phase particle in a tilted "washboard" potential for two values of bias current ($I_b = 0$ and $I_b \approx I_C$) in an overdamped regime. In this case the trajectory of the Phase particle is that of the washboard potential. The virtual phase particle is indicated by a disc. (b) I-V Characteristics of an overdamped Josephson junction ($\beta_c \ll 1$).

In the underdamped regime ($\beta_c \gg 1$), the phase particle (in the absence of thermal and quantum fluctuations) is at rest in the minimum of the washboard potential as long as the bias current I_b is smaller than the critical current of the junction I_C . When I_b reaches the I_C , the phase particle escapes the valley and follows a straight trajectory (see Fig. 3.9(a)). The slope of the trajectory depends on damping. This is because in the underdamped regime $\beta_c \gg 1$ the dissipative term can be neglected and from the Eq. 3.25 one gets a conservative system. The junction voltage jumps discontinuously from the zero-voltage state to a finite value $V = R_N I_C$.

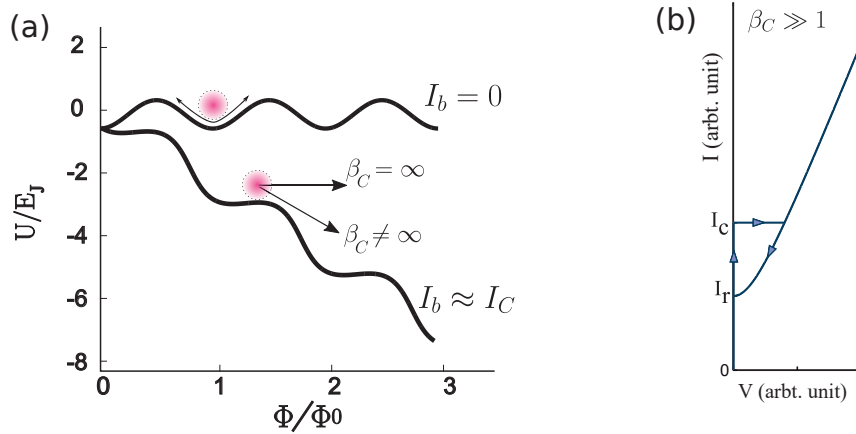


Figure 3.9: (a) Motion of the phase particle in a tilted "washboard" potential for two values of bias current ($I_b = 0$ and $I_b \approx I_C$) in an underdamped regime. The virtual particle is indicated by a solid disc. (b) I-V Characteristics of an underdamped Junction ($\beta_c \gg 1$). The underdamped junction shows a hysteretic behavior, and it switches back from voltage state to superconducting state at the current lower than the critical current, $I_r < I_C$.

When the bias current is reduced, the phase particle stays in the voltage state also for $I_b < I_C$. For $\beta_C \rightarrow \infty$ the retrapping will happen at $I_b = 0$. More in general for β_C finite the energy of the particle is not strictly conserved and the trajectories are not anymore parallel to the Φ axis. In this case, the phase particle gets re-trapped in a potential well (and eventually the system switches back into the superconducting state) once I_b reaches the so called *re-trapping current* I_r . The re-trapping current I_r is given by³⁶

$$I_r \simeq \frac{4I_C}{\pi\omega_p RC}, \quad (3.26)$$

where $\omega_p = \sqrt{\frac{2eI_C}{\hbar C}}$ is the plasma frequency and represents the oscillations of the phase in the potential minimum. The IVC of an underdamped junction shows an hysteretic behavior, and the amount of hysteresis depends on the damping parameter (see Fig. 3.9(b)).

3.5 AC-JOSEPHSON EFFECT: SHAPIRO STEPS

Phase locking is an intriguing phenomenon which happens in a Josephson junction when the Josephson frequency $\omega_J = 2eV/\hbar$ is synchronized with an external microwave field ω_{rf} . When the Josephson frequency ω_J couples to integer multiples of the external driving frequency ω_{rf} , quantized current steps appear in the current-voltage characteristics. They are called Shapiro steps^{96,97} (see Fig. 3.10(a)). The analytical expression

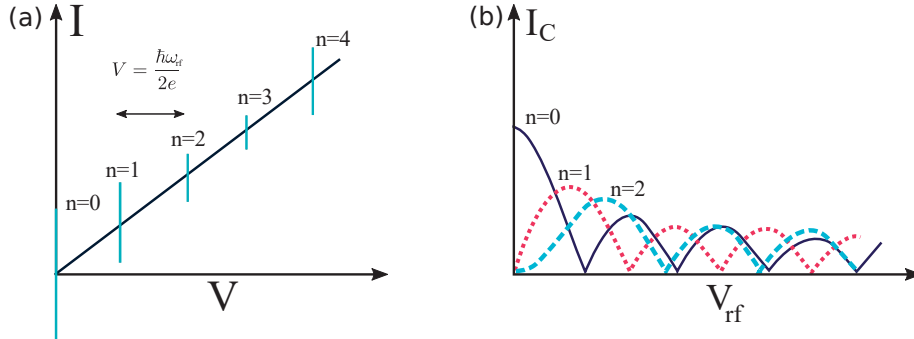


Figure 3.10: (a) Shapiro steps of width $\hbar\omega_{rf}/2e$ in a voltage-biased junction, (b) The height of critical current and the first two steps has a Bessel function power dependence.

for the current steps can be obtained by solving the voltage biased RCSJ model for the junction, in presence of an AC voltage source. One gets steps at $V_n = \hbar\omega_{rf}/2e$ of amplitude

$$I_s = I_C (-1)^n J_n \left(\frac{2eV_{rf}}{\hbar\omega_{rf}} \right), \quad (3.27)$$

where J_n is a Bessel function of the first kind. Moreover, Shapiro spike steps exhibit a Bessel function dependence as $|J_n(2eV_{rf}/\hbar\omega_{rf})|$ as a function of the applied AC voltage

field⁸¹. The dependence of the various step heights on the AC voltage amplitude are shown on Fig. 3.10(b).

Deviation from the Bessel function behavior, Eq. 3.27, are reported for current-biased junctions when the $2eI_C R_N$ product is bigger than the microwave energy $\hbar\omega_{rf}$ ⁹⁸.

Fig. 3.11 shows the measured IVCs of an SNS junction ($w_J = 3 \mu\text{m}$ and $L = 100 \text{ nm}$) placed under microwave irradiation of different powers at $f = 3.9 \text{ GHz}$. Voltage spacing between the Shapiro steps is measured as $\Delta V = 8.14 \mu\text{V}$ which is consistent with the expected value $\Delta V = hf/2e = 8.1 \mu\text{V}$.

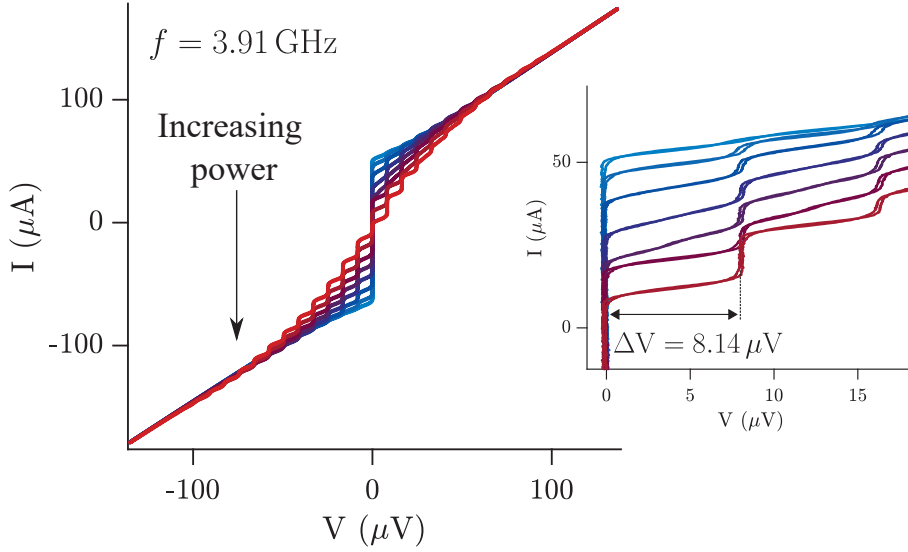


Figure 3.11: Current-voltage characteristic of a YBCO-Au-YBCO junction ($w_J = 3 \mu\text{m}$ and $L = 100 \text{ nm}$) taken at $T = 50 \text{ K}$ (fabricated in this work) for increasing applied microwave power. The inset shows the IVC in a narrower voltage range.

3.6 SUPERCONDUCTING QUANTUM INTERFERENCE DEVICES (SQUIDS)

A SQUID is a macroscopic quantum device that combines the phenomena of fluxoid quantization and Josephson effect. A SQUID sensor is basically a magnetic flux-voltage converter having an extremely low magnetic flux noise. It consists of a superconducting loop of inductance L interrupted by two Josephson junctions, or in general two weak links (see Fig. 3.12(a)). To understand the operation of a SQUID, the variation of the critical current as a function of applied magnetic flux needs to be derived.

In what comes, we derive the static solutions of a dc SQUID following Ref. ⁹⁹. Applying Kirchhoff's law to the circuit of Fig. 3.12 leads to:

$$I = I_1 + I_2 = I_C \sin \varphi_1 + I_C \sin \varphi_2. \quad (3.28)$$

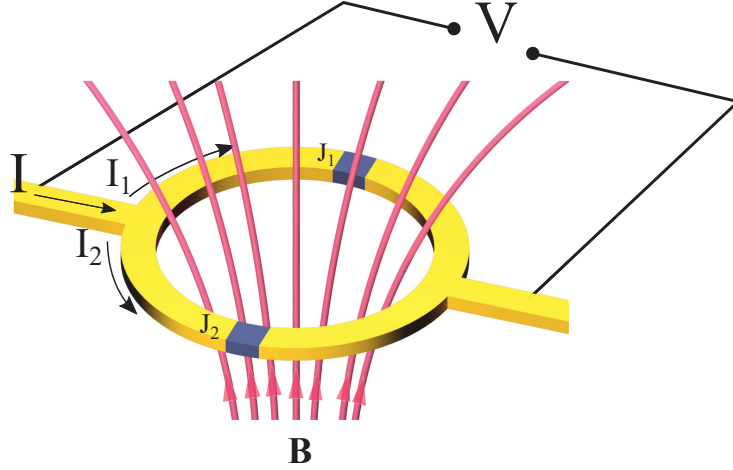


Figure 3.12: Schematic presentation of a SQUID. A dc-SQUID consists of one superconducting loop with two superconducting weak links (behaving like a Josephson junction)

From the fluxoid quantization in the superconducting loop, we have:

$$\varphi_2 - \varphi_1 = 2\pi \frac{\Phi}{\Phi_0} \pm 2n\pi, \quad (3.29)$$

where $\Phi_0 = h/2e$ is the flux quantum and $\Phi = \Phi_{ext} + LI_s$ is the total flux enclosed by the SQUID's loop which is the sum of the applied external magnetic flux and the self magnetic flux induced by the screening current I_s . Inserting the Eq. 3.29 in the Eq. 3.28, the SQUID's current becomes:

$$I = 2I_C |\cos(\pi \frac{\Phi}{\Phi_0})| \sin(\varphi + \frac{\pi\Phi}{\Phi_0}) = I'_C \sin \varphi', \quad (3.30)$$

where $I'_C = 2I_C |\cos(\pi\Phi/\Phi_0)|$, and $\varphi' = \varphi_1 + \pi\Phi/\Phi_0$. The Eq. 3.30 tells us that the DC-SQUID acts as a single Josephson junction with a flux tunable critical current.

Note that in deriving the Eq. 3.30, we assumed identical currents $I_1 = I_2$ and very low inductance or equivalently, the self magnetic flux generated by the screening current is negligible, $LI_s \ll \Phi_0$.

It can be shown that if we consider both the applied magnetic flux and self-flux, the total flux passing through the loop as a function of the Φ_{ext} and φ is given by

$$\Phi = \Phi_{ext} + LI_C \sin \pi \frac{\Phi}{\Phi_0} \cos(\varphi + \pi \frac{\Phi}{\Phi_0}). \quad (3.31)$$

Here, the second term is the circulating current.

In general, the SQUID's inductance L has two components: the geometric inductance $L_g \approx \mu_0 l$ (where l is the junction's length) and the kinetic inductance $L_k =$

$\mu_0 \lambda_L^2 l / wt$ (λ_L is the London penetration depth, w and t are the width and the thickness of the electrodes) which is related to the kinetic energy of the circulating current. The behavior of L_k is very different from that of L_g : its value depends not only on geometrical factors, but on the density of Cooper pairs n_s , and thus on the temperature T . L_k decreases as n_s increases and T decreases. L_k is dominant when the width w and/or thickness t of the SQUID loop are comparable to or smaller than the London penetration depth λ_L ($wt \ll \lambda_L^2$). This is the case with YBCO Dayem-bridge nanoSQUIDs where the two Josephson junctions are substituted by two parallel YBCO nanowires with widths smaller than 100 nm^{100,101}.

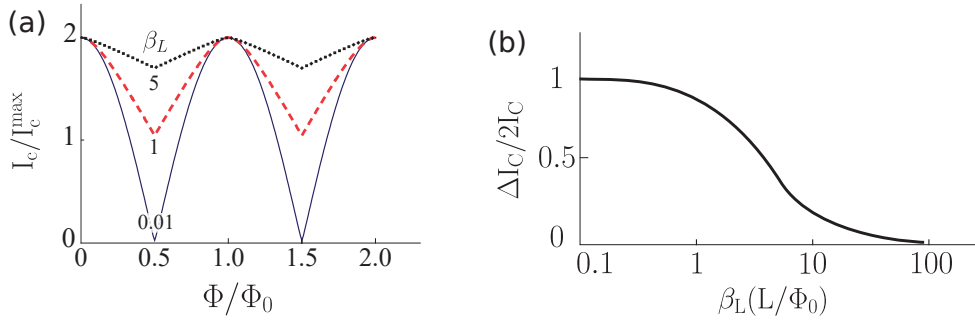


Figure 3.13: (a) Modulation depth of critical current I_C is strongly reduced with increasing β_L . I_C modulation as a function of applied magnetic flux for different values of $\beta_L = 5, 1$ and 0.01 . (b) modulation depth $\Delta I_C / 2 I_C$ vs. β_L as a function of inductance L ¹⁰².

To obtain the critical current modulation as a function of the applied magnetic flux, a numerical iteration method is needed^{103,104}. To study the effect of loop inductance in the response of the SQUIDs critical current as a function of an external applied magnetic field, we introduce the screening parameter $\beta_L = (2LI_C) / \Phi_0$. As shown in Fig. 3.13(a) by increasing the screening parameter β_L the relative critical current modulation $\Delta I_C / 2 I_C$ decreases monotonically as $\approx 1 / \beta_L$. Therefore, one can use this method to measure the value of β_L from the measurement of the critical current versus applied magnetic flux. Tesche and Clarke¹⁰² obtained the critical current modulation of a SQUID ΔI_C versus the β_L for fixed I_C . At small values of L where the $\beta_L \approx 0.1$, ΔI_C approaches $2I_C$. Moreover, for the case where $\beta_L \gg 1$, the critical current modulation depth approaches 0 (see Fig. 3.13(b)). A similar behavior has been also obtained for the case of a nanoSQUID where the both links are characterized by long Dayem ($l \gg \xi$) bridges¹⁰⁵.

4

Mesoscopic transport in SNS junctions

4.1 TUNNELING CURRENT FOR NIN , NIS AND SIS JUNCTIONS

Normal-Insulator-Superconductor (NIS) and Superconductor-Insulator-Superconductor (SIS) junctions are very important structures to get information about the density of states of a specific material*.

The current flowing through a Normal-Insulator-Normal (NIN) junction is given by

$$I_{NIN} = A \int_{-\infty}^{+\infty} |\mathcal{T}(E)|^2 N_L(E) N_R(E + eV) [f(E) - f(E + eV)] dE, \quad (4.1)$$

where the subscripts L and R refer to the left and right normal electrodes, respectively. In Eq. 4.1, $\mathcal{T}(E)$ is the transmission coefficient, $N(E)$ is the normal density of states and $f(E)$ is the Fermi distribution.

Assuming the density of states for both normal conductors and $\mathcal{T}(E)$ are constant, Eq. 4.1 becomes

$$I_{NIN} = A |\mathcal{T}|^2 N_1(0) N_2(0) eV = G_{NIN} V, \quad (4.2)$$

where $G_{NIN} = A |\mathcal{T}|^2 N_1(0) N_2(0) e$ is the conductance of the junction. The current voltage characteristic (IVC) of the NIN junction is ohmic at low voltages.

*In this section we follow Refs. ^{36,106} to study the tunneling transport in NIN , NIS and SIS systems.

For a *NIS* junction, at $T = 0$, the presence of a gap Δ in the density of states of a superconductor leads to a radically different current-voltage characteristic. Considering a BCS density of states for the superconductor $N_S(E) = |E|/\sqrt{E^2 + \Delta^2}$ and a constant density of states for the normal conductor, N_N , One can write the tunneling current as

$$I_{NIS} = \frac{2\pi e A |\mathcal{T}|^2 N_N}{\hbar} \int_0^{eV} dE N_s(E) = \begin{cases} G_{NIN} \sqrt{V^2 - (\frac{\Delta}{e})^2} & |V| > \frac{\Delta}{e} \\ 0 & |V| < \frac{\Delta}{e} \end{cases}. \quad (4.3)$$

The conductance for the *NIS* junction is given by

$$G_{NIS} = \frac{dI_{NIS}}{dV} = \frac{2\pi e A |\mathcal{T}|^2 N_N N_S(E)}{\hbar}, \quad (4.4)$$

and it is proportional to the density of states of a superconductor. The current-voltage and conductance-voltage (GV) characteristics of the *NIS* junction for $T = 0$ and $T \neq 0$ are shown in Fig. 4.1.

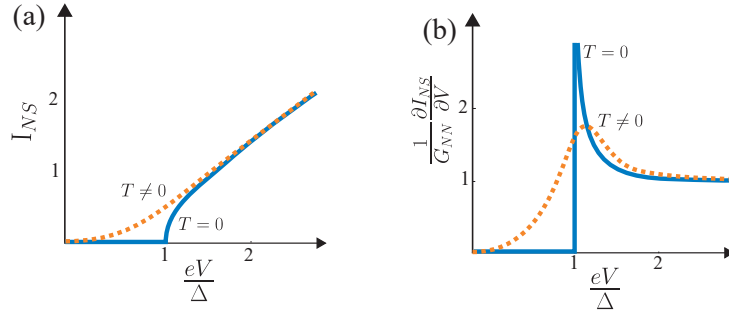


Figure 4.1: (a) Current-voltage and (b) differential conductance-voltage characteristics of a *NIS* tunnel junction at $T = 0$ (blue solid line) and a finite temperature (orange dashed line). At very low temperatures, the normalized differential conductance approaches the superconducting density of states.

Let's consider the case where both electrodes S and S' are superconductors with superconducting energy gap Δ_1 and Δ_2 , respectively. The current through the junction can be obtain by

$$\begin{aligned} I_{SIS'} &= \frac{2\pi e A |\mathcal{T}|^2}{\hbar} \int_0^{eV} dE N_s(E - eV) N'_s(E) \\ &= \frac{2\pi e A |\mathcal{T}|^2}{\hbar} \int_0^{eV} \frac{|E - eV|}{((E - eV)^2 + \Delta_1^2)^2} \frac{|E|}{(E^2 + \Delta_2^2)^{1/2}} [f(E - eV) - f(E)] dE. \end{aligned} \quad (4.5)$$

For $T > 0$, at very low voltages, tunneling can occur for thermally excited quasiparticles. This current is weak and has a maximum at $eV = \Delta_1 - \Delta_2$ when the overlap

between the thermally excited electrons in two superconductors is the largest. Moreover, at higher voltages ($eV > \Delta_1 + \Delta_2$), the current of non-thermal electrons becomes significant and one expects the current to increase sharply as V gets higher than $(\Delta_1 + \Delta_2)/e$. Fig. 4.2 shows the IVC of the SIS' junction for $T = 0$ and $T \neq 0$.

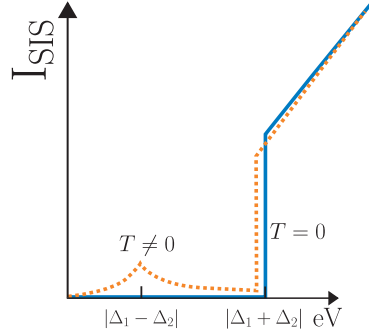


Figure 4.2: Current-Voltage characteristics of a SIS' tunnel junction at zero temperature $T = 0$ (blue solid line) and at non-zero temperature, $T \neq 0$, (Yellow dashed line). The singularity at $|\Delta_1 - \Delta_2|$ happens when the overlap between the thermally excited electrons in two superconductors is maximum, while the jump at $|\Delta_1 + \Delta_2|$ is due to the tunneling of the non-thermally excited electrons.

4.1.1 PROXIMITY EFFECT

In a Normal conductor-Superconductor (NS) junction, when the normal conductor N is in good electrical contact with the superconductor S , Cooper pairs can leak from S to N , modifying the properties of N in such a way that it shows superconducting-like behavior. This phenomenon is known as the proximity effect.

This effect was first treated (mostly qualitatively) by de Gennes¹⁰⁷ for a layered structure of superconducting and non-superconducting materials. He discussed the spatial variation of the microscopic order parameter in a NS sandwich junction. In such a structure, the condensation amplitude $F(x)$ is a function of position¹⁰⁸ and $|F(x)|^2$ is the probability of finding a Cooper pair at a distance x .

Fig. 4.3 shows the behavior of the Cooper pair density $|F(x)|^2$ at the NS interface. Close to the interface on the superconductor region $|F(x)|^2$ is suppressed on a distance ξ_S . The strength of suppression is determined by the so-called pair breaking parameter $\gamma = \rho_S \xi_S / \rho_N \xi_T$ where ρ_S and ρ_N are respectively, the specific normal resistance of the superconducting and normal regions. In this relation ξ_S is the superconducting coherence length in the superconductor region and ξ_T is the thermal coherence length in the normal conductor which will be explained shortly. At the interface, $F(x)$ drops abruptly by the value $\gamma_B = R_B / \rho_N \xi_T$ which is related to the strength of the barrier at the interface as well as the Fermi velocity mismatch between the S and N layers. Here R_B is the specific resistance of the NS boundary¹⁰⁹. $F(x)$ decays exponentially in the normal conductor and on a distance ξ_T from the interface in the normal conductor¹¹⁰.

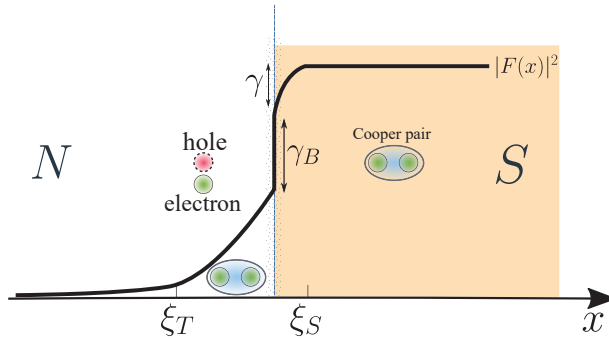


Figure 4.3: Schematic representation of the dependence of the Cooper pair density $|F(x)|^2$ at the NS interface. The proximity effect depends on two dimensionless parameters, so-called pair breaking parameters, γ and γ_B . For small value of γ the $F(x)$ is almost constant in the superconductor and for small limit of γ_B the Cooper pairs practically penetrate inside the normal region at the distance of ξ_T . The increase of γ_B leads to an abrupt drop of $F(x)$ at the NS interface¹⁰⁹.

Therefore, one can find Cooper pairs in the normal conductor over a characteristic length scale ξ_T .

The current understanding of the proximity effect in NS junctions is based on the work done by Andreev¹¹¹ while studying heat transport at NS interfaces. He introduced a microscopic mechanism of converting a single electron/hole into a Cooper pair at the NS interface.

Consider a NS junction in which an electron with energy E traveling inside the N region approaches to the NS interface (see Fig. 4.4). It is well-known that the electrical current in the superconductor is carried by the Cooper pairs. Therefore, an incident electron from the normal conductor with energy E smaller than the gap energy $E < \Delta$ cannot be directly transmitted into the superconductor because there are no available states for a single electron within the superconducting gap.

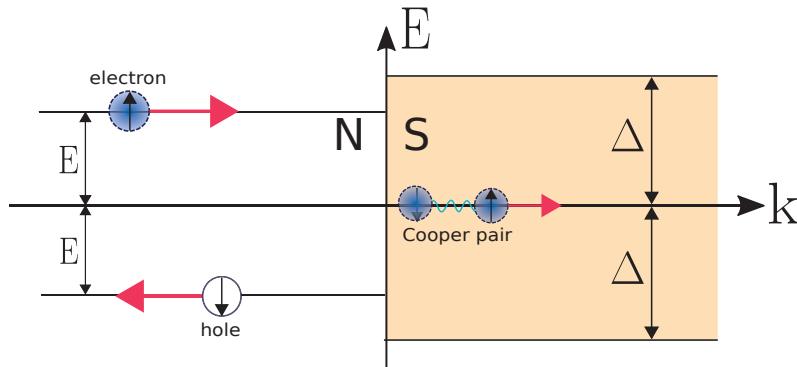


Figure 4.4: Schematic representation of the Andreev reflection at the NS interface. An electron approaching the barrier from the normal conductor with the energy below the superconducting gap cannot be transferred in the superconductor as a single particle. It can only be transferred as a Cooper pair while a hole is retroreflected in the normal metal.

However, another mechanism can take place as predicted by Andreev¹¹¹ where the

incident electron at the interface with $E < \Delta$ couples with another electron from the Fermi sea of the normal conductor and both are transferred as a Cooper pair in the condensate of the superconductor. To preserve charge and momentum conservation, a hole is formed in the normal metal and retroreflected with energy $-E$. This novel mechanism is called Andreev reflection^{111,112} and is shown schematically in Fig. 4.4.

The Andreev reflection is an elastic scattering process and the total energy and spin are conserved. It is also reversible, which means that if an incident hole instead of an electron in normal conductor approaches the NS interface, a Cooper pair in the superconductor will be annihilated and an electron is back-scattered. As a consequence of opposite group velocity and opposite charge of the electron and retro-reflected hole, the conductance of the system is twice as large as the case where we only have normal transmission at the NS interface.

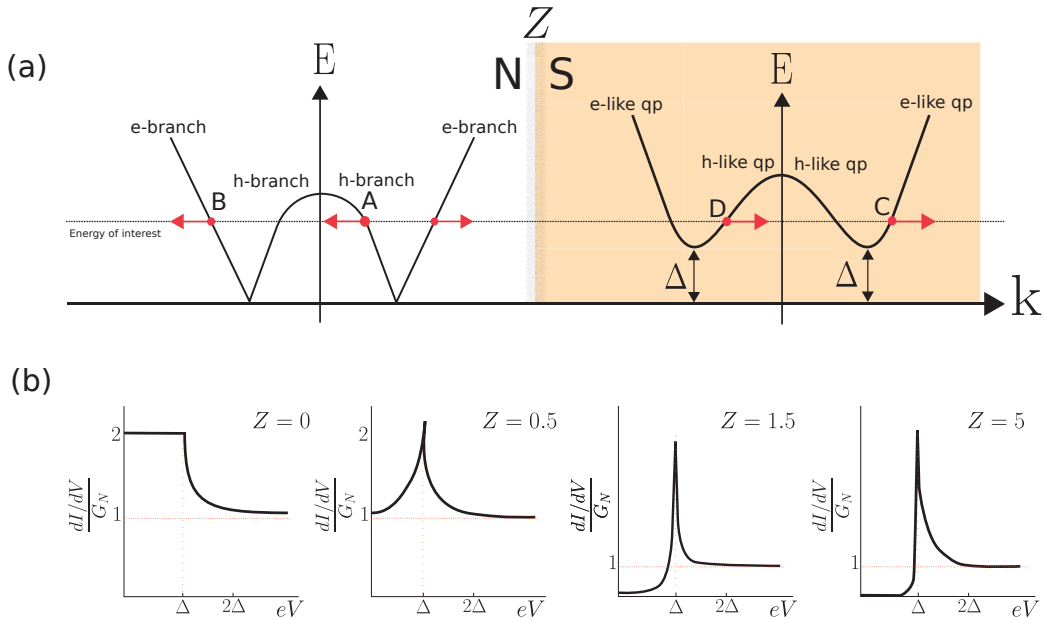


Figure 4.5: (a) Schematic diagram of energy vs. momentum spectrum of N and S at the NS interface (Here the arrows indicate velocities). Four allowed processes for an incident electron can be considered: the Andreev-reflected hole with a probability $A(E)$, the normal-reflected electron with a probability $B(E)$, the transmitted electron-like quasiparticle with a probability $C(E)$ and the transmitted hole-like quasiparticle with a probability $D(E)$. (b) The BTK calculation for the normalized differential tunneling conductance vs. bias voltage of a NS junction for different values of Z at $T = 0$ (adopted from the BTK original paper¹¹³).

The consequences of Andreev reflection on the IVC of a NS junction were studied by Blonder, Tinkham and Klapwijk in 1982¹¹³. Fig. 4.5(a) depicts a schematic representation of energy vs. momentum diagram ($E - k$) for the normal conductor and the superconductor at the NS interface. The superconductor, $E - k$ diagram is given by the BCS theory: for a fixed energy, there are two states for an electron/hole with k

and $-k$ having the same energy. Similarly, the same picture is adopted for the normal conductor.

In the so-called BTK theory, one uses the Bogoliubov de Gennes (BdG) equations to calculate the current of a NS junction for different transparencies of the interface (from a metallic to a tunnel-like). The NS interface is characterized by a dimensionless barrier strength $Z = Hm_e/\hbar^2k_{SF}$, where H is the height of barrier, k_{SF} is the Fermi wave vector in the superconductor, and m_e is the mass of an electron. The interface is highly transparent if $Z \ll 1$ and is weakly transparent (tunnel-like junction) if $Z \gg 1$. With this definition, the transmission probability \mathcal{T} reads as $\mathcal{T} = 1/(1 + Z^2)$ and the current I_{NS} can be calculated by

$$I_{NS} = (2e/h)\Omega \int_{-\infty}^{\infty} dE (f(E - eV) - f(E))(1 + A(E, Z) - B(E, Z)), \quad (4.6)$$

where $A(E, Z)$ and $B(E, Z)$ are respectively Andreev-reflected hole and normal-reflected electron probabilities¹¹³, $f(E)$ is the Fermi function and Ω is a measure of the area of the junction. Table. 4.1 shows the calculated expression $A(E, Z)$ and $B(E, Z)$ within the BTK model.

Table 4.1: Andreev reflection $A(E, Z)$ and $B(E, Z)$ probabilities for a NS junction. $\gamma = u_0^2 + Z^2(u_0^2 - v_0^2)$. Here $u_0^2 = 1 - v_0^2 = \frac{1}{2} \left[1 + ((E^2 - \Delta^2)/E^2)^{1/2} \right]$ are the wavefunctions for an electron and a hole, respectively.

	$A(E, Z)$	$B(E, Z)$
$E < \Delta$	$\frac{\Delta^2}{E^2 + (\Delta^2 - E^2)(1 + 2Z^2)^2}$	$1 - A(E, Z)$
$E > \Delta$	$\frac{u_0^2 v_0^2}{\gamma^2}$	$\frac{(u_0^2 - v_0^2)Z^2(1 + Z^2)}{\gamma^2}$

The zero-temperature differential tunneling conductance G_{NS} is then given by

$$G_{NS} = \frac{dI}{dV} = G_N [1 + A(E, Z) - B(E, Z)]. \quad (4.7)$$

Here, $G_N = 2e^2/h(1 + Z^2)$ is the normal state conductance for $eV \gg \Delta$ of a single channel. The zero bias conductance at zero voltage reads as

$$G_{NS} = \frac{4e^2}{h} \frac{1}{(1 + 2Z^2)^2}. \quad (4.8)$$

Fig. 4.5(b) show the normalized conductance of a NS junction for different values of barrier strength Z . For the case of only Andreev reflection process (perfect transparency) $Z = 0$, the low bias differential conductance ($eV < \Delta$) is twice as large as the

normal state conductance G_N . However, in most cases, NS interfaces are not perfect and there is a barrier ($Z \neq 0$) due to the Fermi-level mismatch, disorders, and scattering sites at the interface and accordingly, the low bias differential conductance is suppressed as Z increases.

4.2 SNS JUNCTIONS

In a SNS junction, where the normal region is confined between two superconducting electrodes, each of the NS interfaces acts as a scattering center for the incident electrons/holes. Because of the Andreev reflection process both electrons and holes reflect as holes and electrons, respectively at the two interfaces (for $eV < \Delta$). Fig. 4.6 schematically shows the Andreev reflection process at the two interfaces of a SNS junction. Here, the reflected hole at the right NS interface (Fig. 4.6) hosts the phase information of the right superconducting electrode, while the reflected electron at the left interface (Fig. 4.6) carries the phase information of the left superconducting electrode. This mechanism, leads to the formation of bound states which include the superconducting phase difference information of the left and right electrodes. This bound states are called Andreev Bound States (ABS) (See Fig. 4.6) and are fundamental to microscopically characterize the Josephson effect.

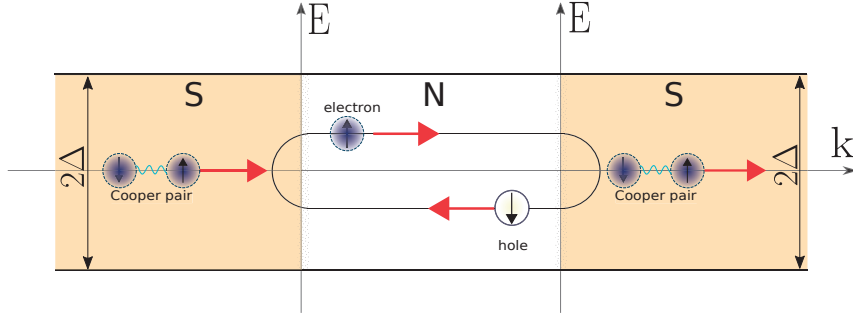


Figure 4.6: Schematic representation of an Andreev bound state in the N region in a SNS junction. The bound-states generally lie within the superconducting energy gap.

SNS junctions show different features compared to the SIS tunnel junctions^{69,113}. For example, an excess current, I_{exc} (defined by extrapolating the linear part of the IV characteristic at $V = 0$) for an ideal SIS junction is zero (see Fig. 4.7(a)). Due to the Andreev reflection in SNS junctions, the IV characteristics at high voltages ($V \gg \Delta/e$) does not follow the normal state relation $V = IR_N$, as it does in a tunnel junction (see Fig. 4.7(b)). Instead, it is shifted by a constant current I_{exc} . Fig. 4.7(c) shows that the value of the excess current decreases as the interface barrier Z increases¹¹⁴.

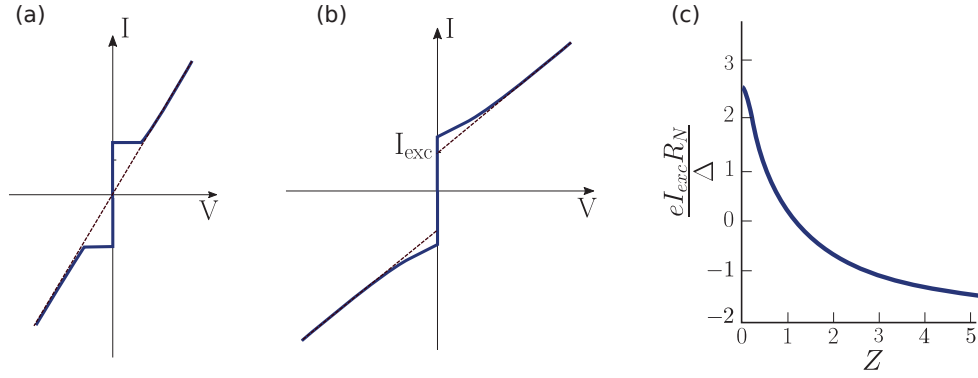


Figure 4.7: (a) The excess current I_{exc} for a SIS junction is practically zero. (b) The contribution of the Andreev reflection in SNS junctions manifests in the appearance of the excess current I_{exc} which is a current added to the normal current $I_N = V/R_N$ at $eV > \Delta$. (c) the excess current dependence on the values of Z .

4.3 CLASSIFICATION OF WEAK LINKS

The coherence of an electron is very decisive in mesoscopic transport. In general, the electron propagation in real materials happens through scattering processes which emerges from a number of different sources of disorder such as defects, impurities, quality of interfaces, lattice vibrations and etc.

To characterize the electron transport in different quantum systems, one needs to evaluate various characteristic length scales which are strongly material dependent. Important characteristic length scales are the phase coherence length L_φ , the sample size L , the electron mean-free path l_e , the superconducting coherence length ξ_S , Normal coherence length ξ_N and thermal coherence length ξ_T .

The phase coherence length L_φ : is the length scale over which an electron maintains its phase coherence and is determined by inelastic scattering processes.

The mean free path l_e : is the average length a charge carrier travels between collisions. Since in transport, only electrons near the material-dependent Fermi energy contribute, the mean free path is $l_e = v_F\tau$, where v_F is the Fermi velocity and τ is the elastic scattering time.

Based on the relation between the junction length L and the mean free path l_e , mesoscopic SNS junctions are classified as ballistic or diffusive. In a diffusive system, charge carriers move through the conductor and experience elastic scattering events while maintaining their phase coherence. In a diffusive system, the sample length L is much larger than the elastic mean free path l_e . In a ballistic system, the charge carriers cross the junction length without experiencing any scattering events. This means that $l_e \geq L$.

Other important length scales are:

The thermal coherence length ξ_T : is the distance in which quasiparticles at temperature T can travel before losing their phase coherence. The thermal coherence length of a diffusive system can be defined as $\xi_T = \sqrt{\hbar D / 2\pi k_B T}$ ($D = l_e v_F^N / 3$ is the diffusion constant of normal conductor), whereas in a ballistic system the thermal coherence length depends on the Fermi velocity of the N interlayer v_F^N and is determined by $\xi_T = \hbar v_F^N / k_B T$.

It is worth mentioning that to be able to consider a SNS junction as a Josephson junction all characteristic length scales of the junction should be smaller than the phase coherence length L_φ and thermal coherence length ξ_T .

The superconducting coherence length ξ_S : is the size of a Cooper pair, $\xi_S = \hbar v_F / \Delta$ where Δ is the superconducting energy gap.

The normal coherence length ξ_N : is the characteristic length scale inside the N region where the electron-hole coherence holds. In a case of a diffusive SNS junction, $\xi_N = \sqrt{\hbar D / \Delta}$ while in a ballistic case can be determined by $\xi_N = \hbar v_F^N / \Delta$. Here, Δ is the superconducting energy gap.

Furthermore, the SNS junctions can be classified as long or short, according to the mutual relation between the coherence length ξ_N and the distance between the electrodes, L . A junction is in the short regime if the length is smaller than the coherence length, $L < \xi_N$; with $L > \xi_N$ it is in the long regime. Junctions are further classified to be in the dirty $l_e \ll \xi_N$ or clean limit $l_e \gg \xi_N$.

A characteristic energy called the Thouless energy E_{Th} is associated with the junction: it is proportional to the inverse of the charge crossing rate of the N region $E_{Th} = \hbar / \tau$. In a diffusive system $\tau = L^2 / D$ while for a ballistic junction $\tau = L / v_F^N$.

The Thouless energy E_{Th} is an important characteristic energy scale in proximity-induced SNS junctions: the characteristic $I_C R_N$ product is determined by the Thouless energy for long junction ($E_{Th} \ll \Delta$) whereas it is governed by the superconducting gap Δ in short junctions ($E_{Th} \gg \Delta$)¹¹⁵. For the sake of clarity, these different regimes are summarized in Table. 4.2.

Table 4.2: Different transport regimes of a SNS junction.

Transport Regime	Short	Long	ξ_N	ξ_T	E_{Th}
Ballistic	$L < l_e, \xi_N$	$\xi_N < L < l_e$	$\hbar v_F^N / \Delta$	$\hbar v_F^N / k_B T$	$\hbar v_F^N / L$
Diffusive	$l_e < L < \xi_N$	$\xi_N, l_e < L$	$\sqrt{\hbar D / \Delta}$	$\sqrt{\hbar D / 2\pi k_B T}$	$\hbar D / L^2$

4.4 CRITICAL CURRENT IN SNS JOSEPHSON JUNCTIONS

Examining the critical current I_C of mesoscopic Josephson junctions and its evolution in temperature $I_C(T)$ allows one to get some insights into the nature of Josephson coupling and the transport regime in the weak link. In this Section, we will look at the temperature dependence as well as the amplitude of the critical current in four possible junctions: short/ballistic, short/diffusive, long/ballistic and long/diffusive.

4.4.1 SHORT-BALLISTIC JUNCTIONS

In short Josephson junctions with normal channel L shorter than the superconducting coherence length ξ_N , the superconducting current inside the weak link is established by a single pair of Andreev Bound states (ABS) ^{116,117} for each channel. The ABS energies have been derived separately by Caroli et al. ¹¹⁸ and Pannetier and Courtois ¹¹⁵. For each transmission channel, the ABS lie at energies $\pm E$ inside the superconducting gap. The \pm sign refers to the oppositely flowing Josephson current. The energy dependence of an ABS, with respect to the phase difference between the electrodes φ is a periodic function and is given by ^{116,117}

$$E = \pm\Delta\sqrt{1 - \mathcal{T}\sin^2(\varphi/2)}, \quad (4.9)$$

where \mathcal{T} is the transmission coefficient. Fig. 4.8(a) shows the Andreev bound states for different values of \mathcal{T} . The value of the gap between two Andreev states at $\varphi = \pi$ depends on the transparency of the interface, \mathcal{T} .

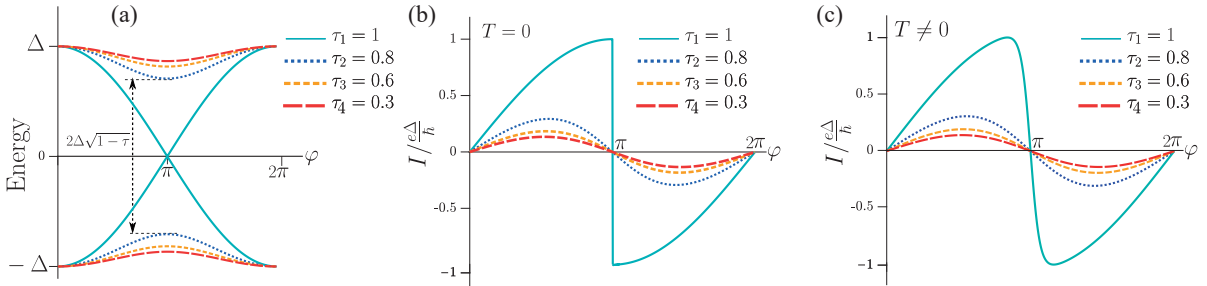


Figure 4.8: (a) Bound state energy versus superconductor phase difference φ for different interface transparencies values \mathcal{T} , (b) current-phase relation of a short ballistic junction at $T = 0$ for different values of \mathcal{T} , (c) the current-phase relation shown in plot 4.8(b) for nonzero temperatures ($T \neq 0$).

From Eq. 4.9, one derives the CPR of the junction

$$I(\varphi) = -\frac{2e}{\hbar} \frac{dE}{d\varphi} = \frac{e\Delta}{2\hbar} \frac{\mathcal{T} \sin \varphi}{\sqrt{1 - \mathcal{T} \sin^2(\varphi/2)}}. \quad (4.10)$$

Fig. 4.8(b) plots Eq. 4.10, for different value of transmission coefficients. At $T \neq 0$, the Eq. 4.10, becomes

$$I(\varphi) = -\frac{2e}{\hbar} \tanh\left(\frac{E}{k_B T}\right) \frac{dE}{d\varphi} = \frac{e\Delta}{2\hbar} \tanh\left(\frac{\Delta\sqrt{1 - \mathcal{T} \sin^2(\varphi/2)}}{2k_B T}\right) \frac{\mathcal{T} \sin \varphi}{\sqrt{1 - \mathcal{T} \sin^2(\varphi/2)}}. \quad (4.11)$$

Here, the hyperbolic tangent function (\tanh) term arises from the temperature dependence of the Fermi-Dirac distribution of the electron density of states. The resulting CPR, Eq. 4.11, is shown in Fig. 4.8(c). Eq. 4.11 is a special case of the more general expression derived by Beenakker¹¹⁹ when the supercurrent is carried by a normal conductor with N quantum channels given by the expression

$$I(\varphi) = \frac{e\Delta}{2\hbar} \sum_{n=1}^N \frac{\mathcal{T}_n \sin \varphi}{[1 - \mathcal{T}_n \sin^2(\varphi/2)]^{1/2}} \tanh\left(\frac{\Delta}{2k_B T} [1 - \mathcal{T}_n \sin^2(\varphi/2)]^{1/2}\right), \quad (4.12)$$

where N is the number of conducting channels $\mathcal{T}_n (n = 1, 2, \dots, N)$.

For a fully ballistic junction with ideal interfaces, ($\mathcal{T}_n = 1$), the supercurrent carried by each channel is given by

$$I_C = \frac{\pi\Delta}{eR_N}, \quad (4.13)$$

where $R_N = h/2e^2$ is the quantum resistance.

4.4.2 LONG-BALLISTIC SNS JUNCTION

Similar to the short ballistic SNS junction, ABS also occur in the long ballistic SNS junctions, with the difference that in the long junction limit, there are ABS with energies at zero-phase $E_{ABS}(\varphi)$ smaller than the superconducting gap Δ .

Since in long junctions, the Thouless energy is smaller than the superconducting gap Δ , the upper limit for the critical current in a long ballistic SNS junction ($\xi \ll L \ll l_e$), is given by the Thouless energy¹²⁰

$$I_C = \frac{E_{Th}}{eR_N}, \quad (4.14)$$

where $E_{Th} = \frac{\hbar v_F^N}{L}$.

4.4.3 SHORT-DIFFUSIVE SNS JUNCTION

For a short diffusive SNS junction ($l_e \ll L \ll \xi$), Kulik and Omelyanchuk¹²¹ used the Usadel equations¹²² and developed the KO-I theory to calculate the relationship between the supercurrent and the phase difference φ

$$I(\varphi) = \frac{4\pi k_B T}{eR_N} \sum_{\omega_n > 0} \frac{\cos \frac{\varphi}{2}}{\sqrt{\Delta^2 \cos^2 \frac{\varphi}{2} + \omega_n^2}} \arctan \frac{\Delta \sin \frac{\varphi}{2}}{\sqrt{\Delta^2 \cos^2 \frac{\varphi}{2} + \omega_n^2}}, \quad (4.15)$$

where $\omega_n = (2n + 1)\pi k_B T$ are the Matsubara frequencies. At temperatures close to T_C , the CPR becomes sinusoidal and reads as

$$I(\varphi) = \frac{\pi \Delta}{2eR_N} \sin \varphi. \quad (4.16)$$

4.4.4 LONG-DIFFUSIVE JUNCTIONS

In a long diffusive *SNS* junction, the Thouless energy is smaller than the superconducting energy gap $E_{Th} < \Delta$ and the critical current of the junction can be calculated by using the quasi-classical Usadel equations^{123,124}. The Usadel equations^{122,125} are the simplifications of quasi-classical Gork'ov equations valid in the diffusive *SNS* junctions. Wilhelm et al.¹²⁶ used quasi-classical Green's function in the dirty limit and found the current has Ambegaokar-Baratoff type dependency and can be expressed by

$$I = \frac{64\pi T}{eR_N} \sum_{\omega_n} \frac{d}{\xi_{\omega_n}} \Gamma \exp\left(-\frac{L}{\xi_{\omega_n}}\right) \sin(\varphi), \quad (4.17)$$

where R_N is the Drude resistance of the junction, $\xi_{\omega_n} = \sqrt{D/2\omega_n}$, Δ is the superconducting order parameter, $\omega_n = (2n + 1)\pi T$ are the Matsubara frequencies and Γ is defined as

$$\Gamma = \frac{\Delta^2}{\left(\omega_n + \Omega_n + \sqrt{2(\Omega_n^2 + \omega_n \Omega)}\right)^2}. \quad (4.18)$$

where $\Omega = \sqrt{\omega_n^2 + \Delta^2}$.

Zaikin and Zharkov¹²⁷ used the Usadel approach and found out that in the long junction regime, the upper limit for the critical current is proportional to $E_{Th} = \hbar D/L^2$ as

$$I_C = \frac{10.82}{eR_N} E_{Th}. \quad (4.19)$$

Table. 4.3 summarizes the amplitude of the critical current I_C of various *SNS* junctions.

4.5 THEORETICAL MODEL FOR JOSEPHSON CURRENT IN A *SINI'S* JUNCTION

To get more information about the transport regime in the *SNS* junctions we studied the behavior of the Josephson current as a function of the temperature. Here, we consider a general *SINI'S* case where a *SNS* junction contains insulating barriers *I* and

Table 4.3: The maximum critical current I_C of different regimes of SNS junctions.

	Short	Long
Ballistic	$I_C = \pi\Delta/eR_N$ ¹²⁸	$I_C = E_{Th}/eR_N$ ¹²⁰
Diffusive	$I_C = 2.07\Delta/eR_N$ ¹²¹	$I_C = 10.82E_{Th}/eR_N$ ¹²³

I' at the NS interfaces. The insulating layers are responsible for scattering of electrons at the interfaces and should be considered when the transparency between the S and N layers is not unity.

In most practical cases, the Fermi-wavelength λ_F is much smaller than the characteristic lengths, e.g. the superconducting coherence length ξ_N and the London penetration depth λ_L , and it is possible to exploit the quasiclassical formalism of Eilenberger functions¹²⁹ † to study and describe the Josephson current in clean SNS junctions.

More recently, Galaktionov and Zaikin¹³¹ generalized the clean limit theory of Eilenberger equations for $SINI'S$ junctions with an arbitrary junction's length and with interface transparencies \mathcal{T}_1 and \mathcal{T}_2 ranging from 0 to 1. They found that the supercurrent can be evaluated from

$$I_J(\varphi) = \frac{4ek_B T}{\hbar} \frac{1}{M} \sin \varphi \sum_{\omega_n > 0} \int_0^1 d\mu \mu \frac{t_1 t_2}{\sqrt{Q(\varphi, \mu)}}. \quad (4.20)$$

Here, $M = k_F^2 W h / 2\pi$ is the number of conducting channels contributing to the current where k_F is the Fermi wave vector. In Eq. 4.20, $t_{1,2} = \mathcal{T}_{1,2} / (2 - \mathcal{T}_{1,2})$ being the barrier strengths and Q reads as

$$Q(\varphi, \mu) = [t_1 t_2 \cos \varphi + \left(1 + (1 + t_1 t_2) \frac{\hbar^2 \omega_n^2}{\Delta^2}\right) \cosh [2\omega_n t_0(\mu)] + (t_1 + t_2) \frac{\hbar^2 \Omega_n \omega_n}{\Delta^2} \sinh [2\omega_n t_0(\mu)]^2 - (1 - t_1^2)(1 - t_2^2) \frac{\hbar^4 \Omega_n^4}{\Delta^4}]. \quad (4.21)$$

Here, l_e is the mean free path of the N, Δ is the superconducting order parameter, $\omega_n = \pi k_B T (2n + 1) / \hbar$ are the Matsubara frequencies, $\hbar \Omega_n = \sqrt{\hbar^2 \omega_n^2 + \Delta^2}$, h is the thickness of the normal conductor, W and L are the junction width and length, respectively.

The supercurrent is carried mostly by the ABS resonances and the Eq. 4.21 describes the properties of every resonances considering interface transparencies $\mathcal{T}_{1,2}$. In Eq. 4.20,

†The Eilenberger transformed the Gor'kov equations¹³⁰ into a much simpler set of integrated Green's functions.

the total current is obtained by summing over all Matsubara frequencies of each ABS resonances which formally extends to infinity. In practice, however, one can cut the summation at sufficiently high maximum number N where the summation converges. N , in principle, depends on the temperature and the superconducting gap and can be roughly estimated by $N = \Delta/2\pi T$.

In Eqs. 4.20 and 4.21, $\mu = \frac{k_x}{k_F} = \sin\theta$, where θ is the angle between the speed of electron and the line normal to the leads edges. Consequently, $t_0(\mu)$ is the time-of-flight of electrons moving along the straight line connecting the two superconducting leads to having the angle θ and takes the form

$$t_0(\mu) = \frac{l_e}{(1 - \mu^2)v_F \left(\sqrt{1 + \frac{l_e^2}{L^2(1-\mu^2)}} - 1 \right)}. \quad (4.22)$$

In a clean junction, the mean free path is much larger than the junction length and it is possible to consider $l_e = \infty$ in Eq. 4.22. Consequently, the time-of-flight of electrons can be obtained by

$$t_0(\mu) = L/v_F \sqrt{1 - \mu^2}. \quad (4.23)$$

In contrast, the electron time-of-flight in a diffusive junction t_0 only depends on the junction length L and the diffusion constant D and does not depend on μ . The t_0 is given by

$$t_0 = \frac{L^2}{D}. \quad (4.24)$$

Eventually, the normal state resistance of the junction is given by

$$R_N = \frac{2\pi\hbar}{Me^2} \left(\frac{1}{\mathcal{T}_1} + \frac{1}{\mathcal{T}_2} + \frac{3L}{4l_e} - 1 \right), \quad (4.25)$$

where M is the number of conducting channels, $\mathcal{T}_{1,2}$ are the interface transparencies at both ends. The Eq. 4.25 is indeed the sum of three resistances in series: two barrier resistances and the resistance of the diffusive conducting channel. The last factor, -1 , is a correction term, which is important in a clean system and for high transparency of the barriers.

We apply the Eq. 4.20-4.25 to assess the transport properties of YBCO/Au/YBCO junctions, where YBCO is the superconducting electrodes and Au acts as the normal conductor with I and I' the barriers with the interface transparencies \mathcal{T}_1 and \mathcal{T}_2 .

The current-phase relation introduced in Eq. 4.20 for the *SINI'S* junctions, covers both ballistic junctions of arbitrary length as well as diffusive short junctions. However, the long diffusive junctions with a Thouless energy smaller than the superconducting

gap energy can not be fitted with this relation. The ratio of junction length L and mean free path l_e indicate if the junction is in the ballistic or diffusive regime.

In order to implement the Eq. 4.20 to study our junctions, we are required to first define the following parameters: barrier transmissions \mathcal{T}_1 and \mathcal{T}_2 , thickness of the gold film connecting the leads h , mean free path in gold l_e , zero temperature value of the superconducting gap in YBCO Δ_0 , critical temperature of YBCO electrodes T_C , inter-distance between the superconducting leads L , width of the junction W . Among these parameters, some of them are not known to us and the fitting of $I_C(T)$ measurement allows us to get more insight into parameters like the interface transparencies of the barriers and/or the junction length.

In the fitting procedure, for temperature T_0 , the critical current can be found as $I_C(T_0) = \max[I_J(\varphi, T_0)]$ by numerically computing the phase φ_0 where the CPR, Eq. 4.20, is maximum. To do so, one needs to solve the $\frac{\partial I_J}{\partial \varphi}|_{\varphi_0} = 0$, to determine the value of φ_0 where the $I_J(\varphi, T_0)$ is maximum. Then, by inserting the φ_0 into the CPR, the critical current I_C is obtained. Similarly, to construct the $I_C(T)$ for the entire temperature spectrum, this scheme should be repeated for the full range of temperature. Note that in the numerical fitting process, we have to consider a finite number of Matsubara frequencies ω_n , and larger number of ω_n improves the accuracy of the fitting.

This page intentionally left blank.

5

YBCO film growth

5.1 YBCO THIN FILM GROWTH USING PULSED LASER DEPOSITION

Many techniques, such as rf-magnetron sputtering, pulsed laser deposition (PLD), chemical vapor deposition (CVD), molecular beam epitaxy (MBE), high pressure DC sputtering, thermal co-evaporation, solution deposition have been used to grow high quality YBCO thin films. Among these deposition techniques, PLD and sputtering have demonstrated to be the most effective and reliable methods to grow stoichiometric YBCO films.

In this work, all the YBCO films were deposited by the PLD technique. Fig. 5.1 shows a sketch of a PLD unit we have used. The PLD chamber is a part of a cluster deposition system and it is connected to the metal sputter chamber and the oxide sputter chamber through a high vacuum (UHV) buffer line which makes it possible to *in-situ* deposit multi layers of metals and oxides.

5.2 GROWING *c*-AXIS YBCO ON MgO (110) SUBSTRATE

The choice of the substrates is very important to grow high quality and epitaxial YBCO thin films. The basic requirements for the substrates are:

- 1– Crystallographic lattice match between the film and the substrate.
- 2– Similar thermal expansion coefficients of the YBCO film and the substrate.
- 3– No chemical interaction at the interface between film and substrate.
- 4– Low value of dielectric constants for microwave applications.

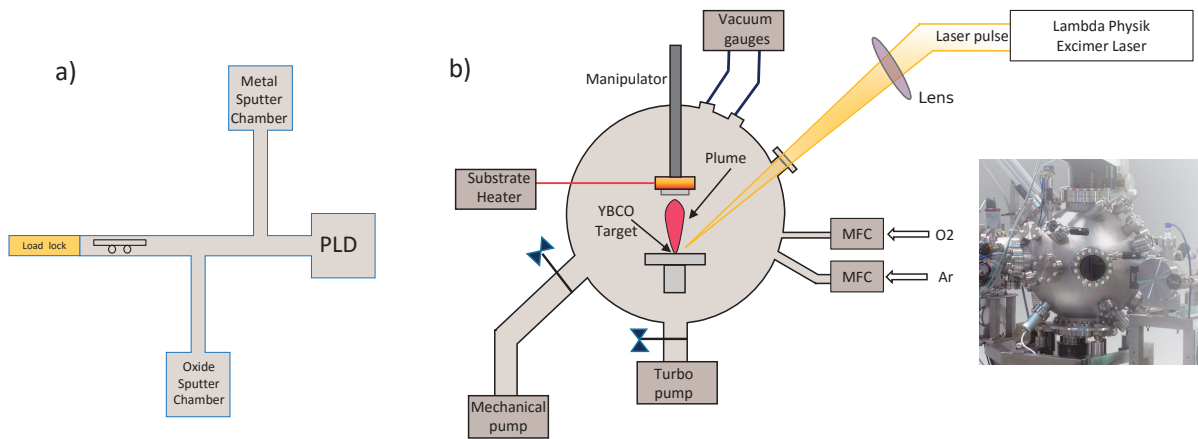


Figure 5.1: a) Sketch of the DCA deposition system with load-lock chamber and a buffer-line connecting the metal sputter, the oxide sputter and the PLD chambers. b) The schematic of the PLD system used for growing YBCO materials. The energetic laser pulses hit the target and evaporate the material from its surface ("ablation"). The vaporized material contains neutrals, ions, electrons etc. The ablated material then condenses on the substrate leading to the growth of thin films of the target material.

Substrates like LaAlO_3 (LAO), SrTiO_3 (STO) and MgO are commonly served as the substrates for growing YBCO films. In this thesis, the substrate used for growing *c*-axis YBCO films is MgO with a (1 1 0) surface. It has a rectangular lattice structure ($[0, 0, 1] = 4.21 \text{ \AA}$, $[1, 1, 0] = 5.96 \text{ \AA}$).

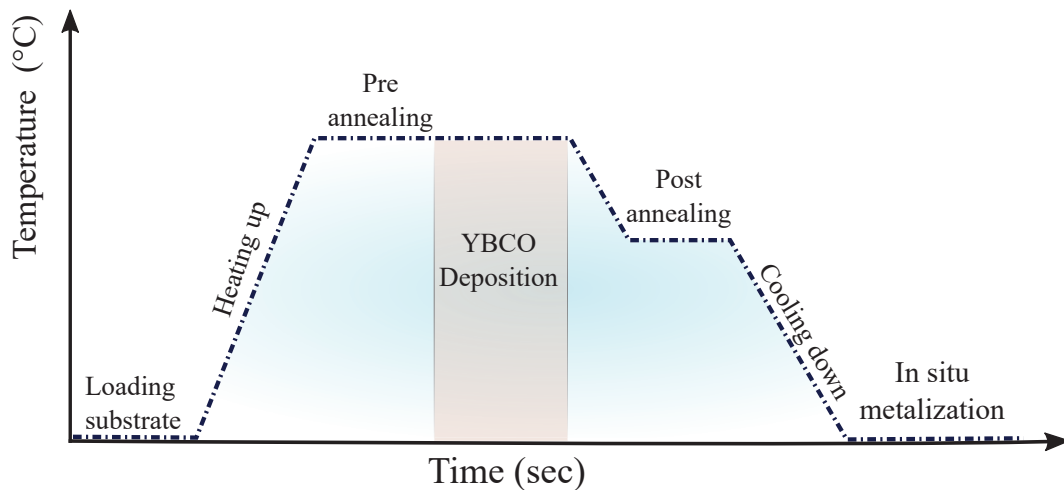


Figure 5.2: Schematic representation of the deposition cycle for growing *c*-axis oriented YBCO films

The PLD growth of *c*-axis YBCO films is schematically depicted in Fig. 5.2. A great deal of time has been devoted to optimize the YBCO growth on MgO substrates.

Table 5.1 summarizes the optimized deposition parameters for growing high quality epitaxial c -axis YBCO films on (1 1 0) MgO substrates.

Table 5.1: Deposition conditions optimized for the epitaxial growth of YBCO thin film by PLD.

Deposition parameters	Value
T_{sub}	750°C
R_h	20° C/min
$T_{pre-ann}$	750°C
$t_{pre-annealing}$	2 hours
p_{O_2}	0.6 mbar
f_L	10 Hz
d	54 – 55 mm
J	1.38 J/cm ²
R_{dep}	0.55 Å
$T_{post-ann}$	760 °C
$t_{post-ann}$	1 hour
p_{ann}	960 Torr
R_{cd}	10°C/min

The surface morphology was investigated by SEM, and surface roughness was measured by AFM (See Fig. 5.3). The as-grown c -axis YBCO films show smooth surfaces with a few holes and an average roughness of 1.5 – 2 nm. We found that, the time of substrate pre-annealing strongly reduces the surface roughness of the YBCO films.

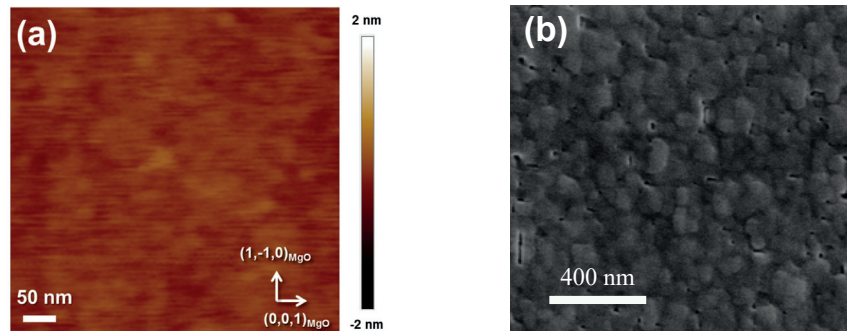


Figure 5.3: a) AFM and b)SEM image of the surface of a YBCO film on MgO (1 1 0) substrate.

The resistance-temperature $R(T)$ measurement is used as a standard characterization of the transport properties of the YBCO film. The $R(T)$ of a typical YBCO film is shown in Fig. 5.4(a). The temperature T_C , defined at the onset of the superconducting transition, is ≈ 84.5 K (see Fig. 5.4(b)), below the T_C of the bulk, but still among the highest values reported in literature so far for the YBCO films on MgO substrates. The homogeneity of the films is proven by a rather sharp transition with a width ΔT

calculated ≈ 0.8 K.

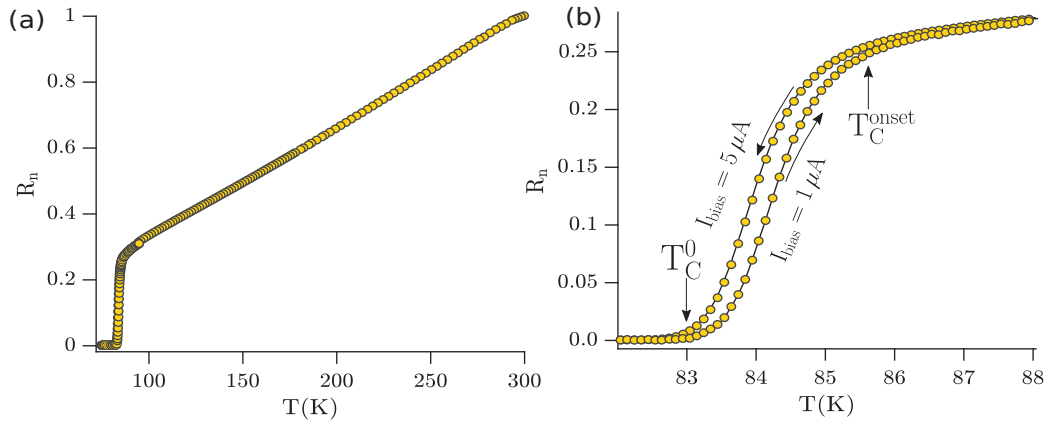


Figure 5.4: (a) The normalized resistance-temperature measurement of a 50 nm thick YBCO film on MgO (1 1 0) substrate, (b) The R-T measurement at the transition temperature T_C for $I_{bias} = 1, 5 \mu A$.

The structural properties have been determined by X-Ray Diffraction (XRD) analysis. Symmetric θ - 2θ scan confirms that the films are highly crystalline and c -axis oriented (see Fig. 5.5).

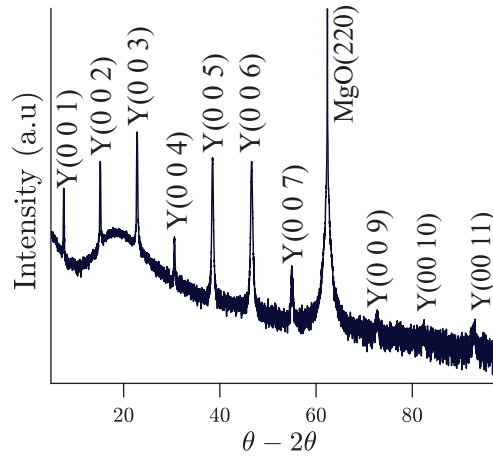


Figure 5.5: The $\theta - 2\theta$ XRD scan of the YBCO film shows only the 00ℓ YBCO reflections.

5.3 GROWING a -AXIS YBCO ON SLGO SUBSTRATE USING PBCO BUFFER LAYER

a -axis YBCO films are in principle more suitable for the fabrication of hybrid devices. The reason is twofold: first, to have a strong proximity coupling at the SN interface, it is important that the order parameter (OP) is maximum at the interface. As shown schematically in Fig. 5.6(a), in planar nanogap based a -axis YBCO hybrid junction, the

CuO_2 planes are in contact with the interface barrier. For the c -axis film, instead, the CuO_2 planes are parallel to the barrier (see Fig. 5.6(b)) and the coupling to the barrier is through the c -axis.

Another element that matters is the coherence length which in the $a - b$ planes is one order of magnitude higher than the one along the c -axis ξ_c . Consequently, in case of a non-ideal/stoichiometric and disordered YBCO region in contact with a normal barrier, the longer coherence length increases the probability of Cooper pair tunneling through the barrier.

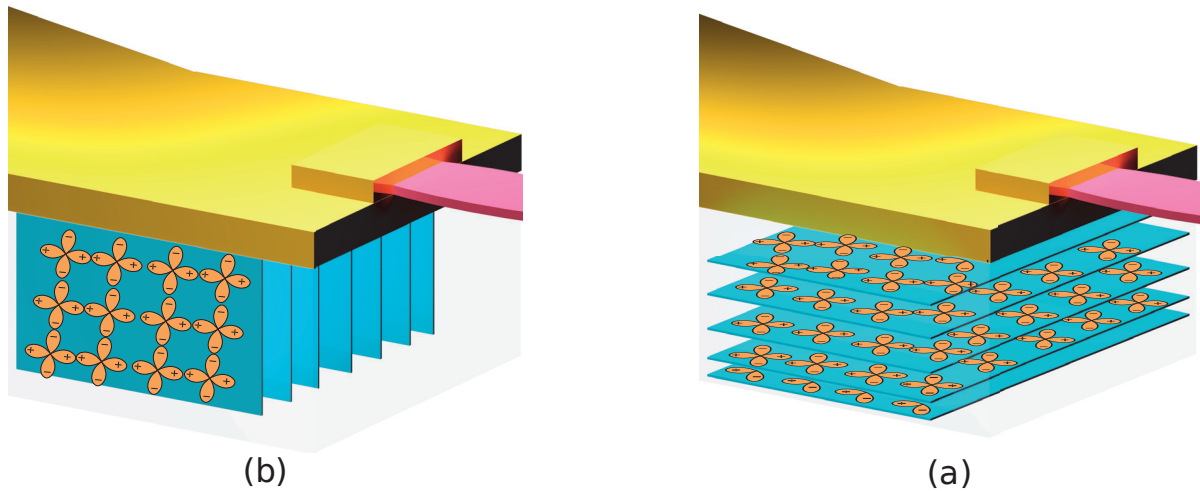


Figure 5.6: Schematic representation of a hybrid junction with (a) a -axis YBCO film electrode, (b) c -axis YBCO film electrode. The orientation of the d -wave order parameter is also shown.

It has been shown that there are two main methods to grow a -axis YBCO films:

- **A self template:** A thin YBCO film is first grown at a temperature [600–650°C] on substrates like NdGaO_3 , SrTiO_3 and LaAlO_3 . At such a low temperature the a -axis growth is more favorable. Because of the a -axis YBCO self-template, the quality of the first layers is generally poor. The substrate temperature is then increased to the usual condition for c -axis growth and the film will continue to grow a -axis. This ensures the growth of high quality films^{132–134}.

- **Using a buffer layer:** Table. 5.2 compares the crystal parameters of different substrates used in growing a -axis YBCO films. Among them, it is shown that a very high quality a -axis YBCO films can be obtained by using SrLaGaO_4 substrate with a buffer layer of $\text{PrBa}_2\text{Cu}_3\text{O}_{7-x}$ ^{135,136}.

Table 5.2: Comparison of different substrates suitable for growing a -axis YBCO films.

Substrate	Crystal structure	Lattice orientation	a	b	c	Dielectric constant
MgO ¹³⁷	Cubic	(001)	4.213	—	—	9.8 ¹³⁸
SrTiO ₃	Cubic	(001)	3.905	—	—	300 at Room T 10 ⁴ at Low T ¹³⁸
NdGaO ₃	Orthorhombic	(001)	5.431	5.499	7.710	20 ¹³⁸
LaGaO ₄	Orthorhombic	(001)	5.487	55.520	7.752	25 at RT ¹³⁹
SrLaGaO ₄	Tetragonal	(001)(100)	3.843	—	12.681	25 along c -axis 6.24 along a -axis ¹⁴⁰
YBa ₂ Cu ₃ O _{7-γ}	Orthorhombic		3.883	3.818	11.681	

In this work we developed the process of growing very high-quality a -axis oriented YBCO films on (100) SrLaGaO₄ substrate using PBCO buffer. The SrLaGaO₄ substrate is indeed the best choice for growing a -axis YBCO films since the lattice mismatch between the SrLaGaO₄ substrate and PBa₂Cu₃O_{7- γ} buffer layer is very small, about -0.7% , and the matching between the substrate SrLaGaO₄ and YBCO film is less than 0.6% . Moreover, the thermal expansion coefficient difference between the film and substrate is very important to reduce the thermal stresses in film and substrate. As shown in Table. 5.3 the thermal expansion coefficients for the in-plane and out-of-plane directions of the SrLaGaO₄ substrate and YBCO film are very similar.

Table 5.3: The thermal expansion coefficients in a/b- and c-direction of SrLaGaO₄ and YBCO are nearly the same.

direction	SrLaGaO ₄ (ppm/K)	YBa ₂ Cu ₃ O _{7-γ} (ppm/K)
a/b-axis	10.05	10
c -axis	18.94	17

In what follows, we explain in detail the growth procedure of a -axis YBCO films. We used single crystal (100) SrLaGaO₄ substrates. Then we have used a 200 nm thick PBCO buffer layer, deposited by rf sputtering (rf power = 50 W, at 830°C, $p_{O_2} = 0.1$ mbar) on top of a SrLaGaO₄ (100) substrate. The sample is then transferred *in situ* to the pulsed laser deposition (PLD) chamber, where a 50 nm thick YBCO film is deposited at a temperature of 790°C, in a 0.82 mbar O₂ atmosphere. While the sample is heated to reach the deposition temperature, the O₂ pressure is kept at 300 Torr, to avoid oxygen out diffusion from the PBa₂Cu₃O_{7- γ} layer which could favor the nucleation of c -axis domains in the YBa₂Cu₃O_{7- γ} layer. Fig. 5.7 summarizes the various steps required to grow high quality a -axis YBa₂Cu₃O_{7- γ} films.

5.4 CHARACTERIZATION OF a -AXIS ORIENTED YBCO FILMS

The structural properties of the films have been analyzed by X-ray diffraction (XRD). In the symmetrical $2\theta - \omega$ scans, only the (ℓ 00) reflections of YBCO - in addition to

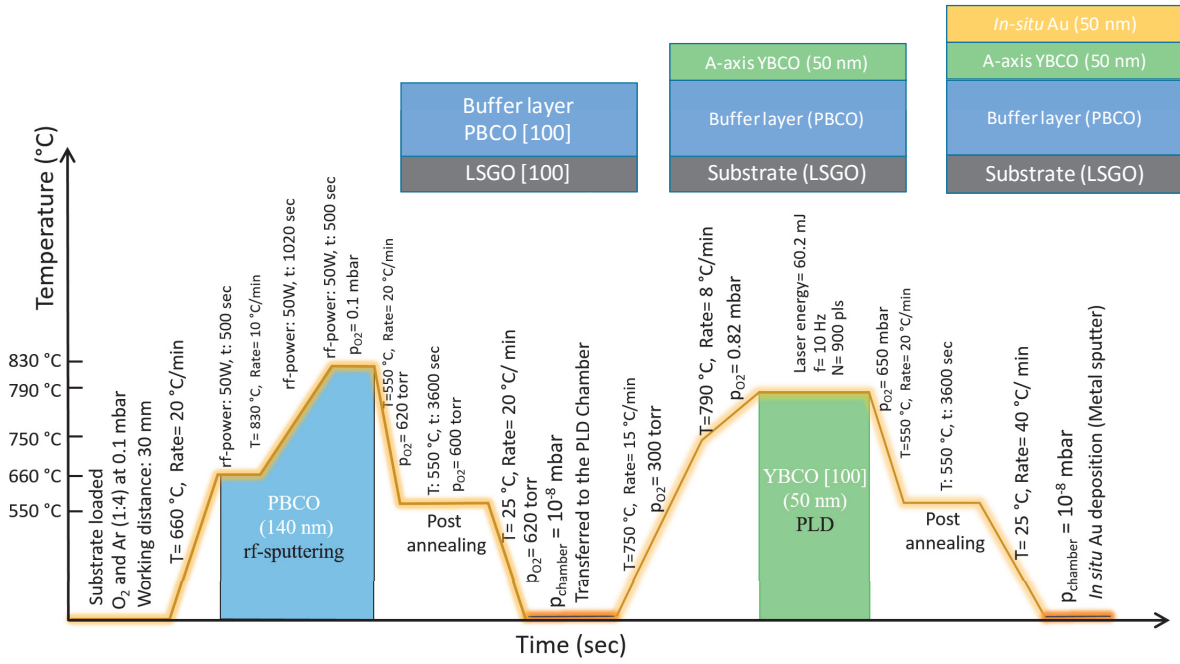


Figure 5.7: Thin film growth cycle for sputter deposition of a PBCO buffer layer and PLD deposition of *a*-axis YBCO films (50 nm).

the $(\ell 0 0)$ reflections of the PBCO buffer layer - can be observed (Fig. 5.8 and inset therein), confirming that the films are highly crystalline, and purely *a*-axis oriented.

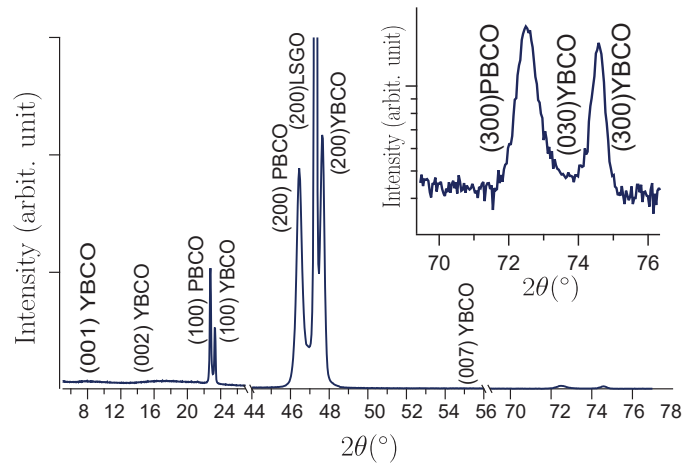


Figure 5.8: 2θ - ω XRD pattern of the 50 nm thick YBCO films grown on (1 0 0) SLGO substrate, by using a 200 nm PBCO layer as a buffer. From the figure, it is evident that not only the $(00n)$ peaks are missing, confirming the absence of *c*-axis oriented grains, but also the $(0m0)$ reflections related to a *b*-axis orientation of the YBCO unit cell (see inset).

To explore the in-plane texture of these films, ϕ scans of the $(1 0 2)$ YBCO reflections have been performed. Only two peaks are present, with a symmetry of 180° (see

Fig. 5.9): this evidence confirms that the b -axis and the c -axis of YBCO are not exchanged (the film is untwinned), in agreement with previous results on a -axis YBCO films reported in literature^{141,142}.

Fig. 5.10(a) shows a typical SEM image of a -axis grown films. A granular structure is visible, characterized by elongated domains, typical of a -axis films¹³⁶, oriented along the $[0, 1, 0]$ YBCO direction (b -axis).

Fig. 5.10(b) shows the resistance versus temperature $R(T)$ of a typical thin a -axis film measured along the b -axis (blue squares) and the c -axis (yellow squares) direction. The evolution of the resistance in temperature is anisotropic: The resistance along the b -axis direction exhibits a linear temperature dependence in full range of temperature, from room temperature (300 K) down to the T_C , which is a typical behavior of optimally doped films¹⁴³. While the range of linearity decreases for the resistance along the c -axis, it shows a downward bending with the temperature. This is a characteristic of underdoped YBCO films.

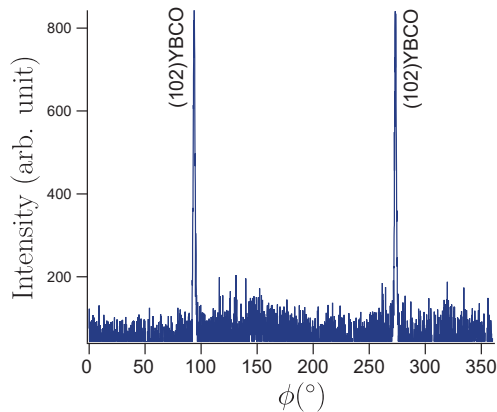


Figure 5.9: XRD ϕ scan of the YBCO (1 0 2) reflections confirms the untwinned nature of our a -axis YBCO films.

For this film, we measured a critical temperature $T_C \approx 88$ K with a transition broadening $\Delta T_C \approx 3$ K for both in-plane directions (see the inset of Fig. 5.10(b)).

5.5 GROWING ULTRA-THIN c -AXIS YBCO FILMS ON MgO (1 1 0)

We have grown ultra-thin c -axis YBCO films down to 3 nm on MgO (1 1 0) substrates. For each film, we first pre-annealed the MgO substrate at the deposition temperatures for 2 hours and then deposited the YBCO thin film using the deposition parameters listed in Table. 5.1. To preserve the superconducting properties of the ultra thin YBCO films a 50 nm Au film is *in-situ* sputtered at very low power ($P= 10$ W).

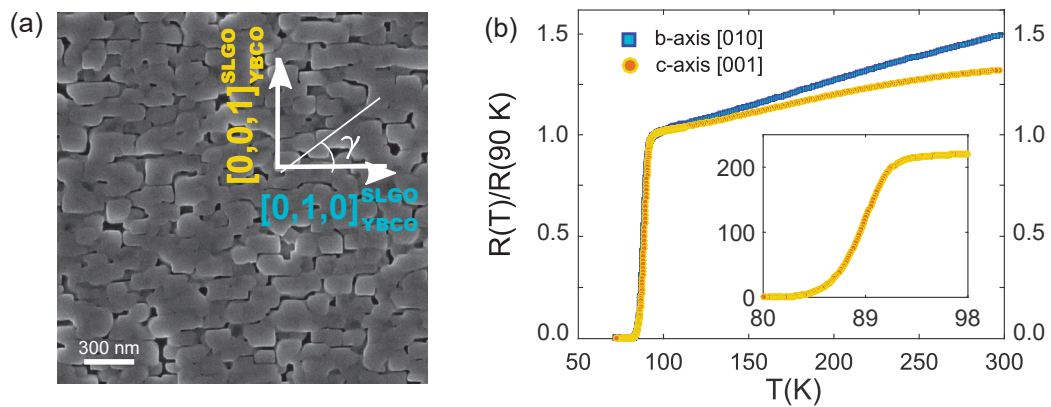


Figure 5.10: (a) SEM image of an *a*-axis YBCO film. The *c*-axis and *b*-axis and in-plane γ is shown in the figure. (b) The resistance-temperature of an *a*-axis grown film, measured both along the $[0 1 0]$ (blue squares) and $[0 0 1]$ (yellow circles) YBCO direction. The film exhibits the critical temperature T_C of ≈ 88 K. The inset shows the RT of the film at temperature close to T_C .

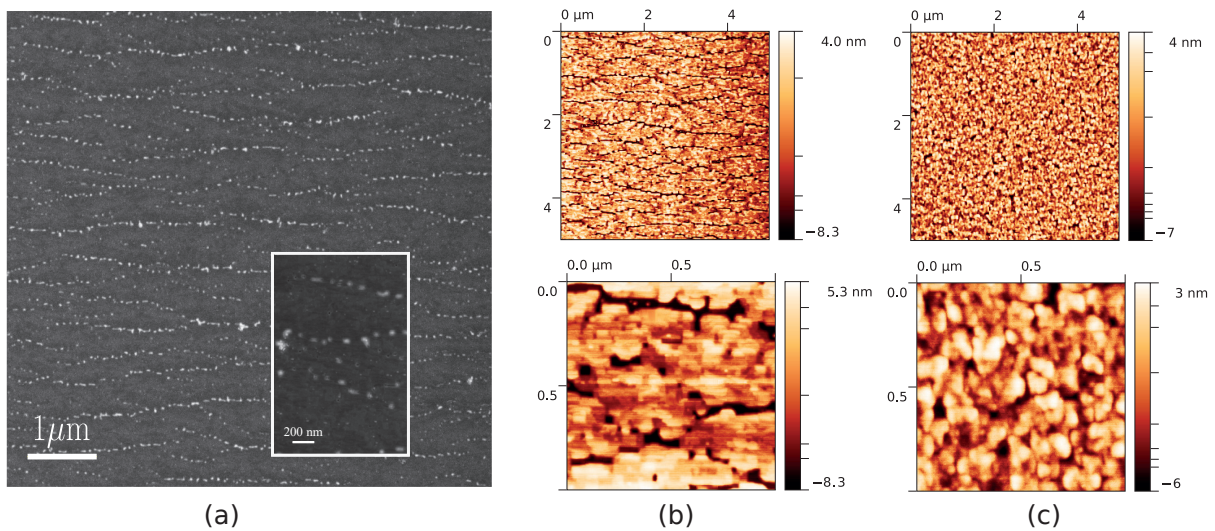


Figure 5.11: (a) SEM image of a 10 nm thick YBCO film deposited on MgO substrate. (b) AFM image shows the surface profile of a 5 nm thick YBCO film. (c) AFM picture of a 10 nm thick YBCO film.

The thickness, surface morphology and roughness of our films were investigated using AFM and SEM imaging. We observed that the average roughness of our films are lower for thicker films. Fig. 5.11(a) shows the SEM a 10 nm thick YBCO film.

The AFM images for 5 nm and 10 nm thick YBCO films are shown in Fig 5.11(b-c), respectively. In very thin films (3–5 nm thick films), preferential elongated grains which follow the morphology of the annealed substrate are very visible along the b/a -axis of the YBCO film. AFM measurements show that the elongated grains are separated by deep "valleys" which reach the substrate for 5 nm thick films (not complete coalescence of the grains). The density and depth of "valleys" visible in the 5 nm thick films, reduced significantly in the 10 nm thick films.

Fig. 5.12, shows the resistive transition of bare films of 10, 20, 30 and 50 nm thick films. The $T_{C_{onset}}$ of the films slightly decreases with the film thickness, while the transition broadening increases considerably by reducing the thickness. For films with thicknesses below 10 nm, we *in-situ* sputtered 50 nm thick Au layer after the YBCO film deposition. The T_{C_0} decreases almost linearly with decreasing the thickness down to 5 nm which corresponds approximately to 4 unit cells. For the 3 nm thick film, which only has two complete atomic layers, the T_{C_0} drops abruptly to 14.5 K.

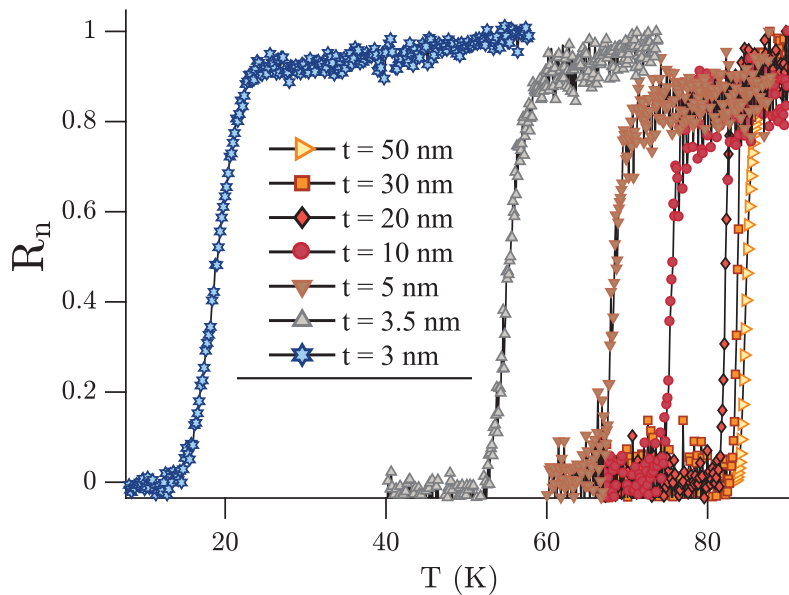


Figure 5.12: Normalized $R_n - T$ measurements of bare YBCO films with various thicknesses down to 3 nm.

6

Nanofabrication processes

The fabrication of YBCO/Au nanogap interfaced with an "exotic" metal or a semiconductor requires various e-beam lithography. The first is to open a nanogap in a film covered with Au. In principle, at this stage a flake or a nanowire could be transferred into the nanogap and anchored/contacted with the electrodes. However, this procedure would imply the direct contact of the YBCO sides of the nanogap with resists and chemicals which would seriously damage the exposed YBCO enlarging the effective size of the nanogap.

We have therefore engineered a procedure where the YBCO/Au nanogaps are first encapsulated with a Pt/Au bilayer before being exposed to further processing. This requires a second e-beam lithography to reopen the nanogap after deposition of the thin Pt/Au bilayer. At this point, the encapsulated nanogap is fully protected and ready to be interfaced with any kind of materials which would require a further third lithographic step.

6.1 FABRICATION DETAILS OF YBCO NANOWIRES

In this section, we describe in details the fabrication process of YBCO nanowires encapsulated with a Pt/Au bilayer. The proposed fabrication process follows the same fabrication steps required to realize encapsulated YBCO nanogaps. To demonstrate the effectiveness and reproducibility of this approach we have fabricated and characterized three different sets of nanowires, which can be described as follows:

- **1EBL devices.** In these samples, nanowires capped with Au are completely fabricated in a single lithography step. As they experience the minimum number of fabrication steps, we considered them as "reference" systems concerning the best superconductive properties one can achieve in a YBCO nanostructure under specific oxygen doping conditions.
- **2EBL devices.** These samples experienced two lithography steps. The first lithography process is required to pattern the nanowire capped with Au and another one for connecting the nanowire to the outer bonding pads employing a lift-off procedure. In the lift-off process, the edges of nanowire which are unprotected get in direct contact with e-beam resist and other chemicals.
- **3EBL devices.** A three lithography process was performed to encapsulate YBCO nanowire with a Pt/Au bilayer. Although, one could argue that it is possible to make protected YBCO nanowires with two e-beam lithography steps, we intentionally fabricated them in three steps to emulate the fabrication procedure necessary to obtain YBCO nanogap-based hybrid devices.

A Diamond-Like Carbon (DLC) mask is deposited on a bilayer Au/YBCO and used to define the nanostructures. The process flow to realize the 1EBL nanowires is schematically illustrated in Fig. 6.1(a-g)^{144–146}. One crucial step to preserve the superconducting properties of YBCO during the fabrication process is to keep the baking temperature of the resist below 90 °C. We found out that this temperature strongly minimizes the oxygen out-diffusion from YBCO nanostructures. As shown in Fig. 6.1(h), the final shape of the nanowire is trapezoidal as a consequence of the Ar⁺ ion milling process. From AFM analysis, we have estimated the angle between the substrate surface and the nanobridge sidewalls to be approximately 75 °¹⁴⁶.

To investigate the extension of the damaged region in the electrodes, once the YBCO is in contact with resist and, in general, with chemicals (such as water, solutions and removers), we have fabricated 2EBL YBCO nanowires. The details of fabrication process are illustrated in Fig. 6.2(a-d). Here, the sides of YBCO are not protected during fabrication. To realize these samples we have first fabricated nanowires following the 1EBL procedure by using a layout where the current is fed into the nanowire through the same large electrodes where the voltage drop is measured (see Fig. 6.2(a)). Then with a second EBL, where the resist gets in contact with the sides of the YBCO nanostructure, the narrow Au voltage probes are defined using a lift-off process (see Fig. 6.2(d)).

To preserve the YBCO nanowire from being damaged by chemicals and resist we have encapsulated the nanowire with a thin bilayer of Pt/Au. The fabrication process of the 3EBL nanowires is schematically depicted in Fig. 6.3.

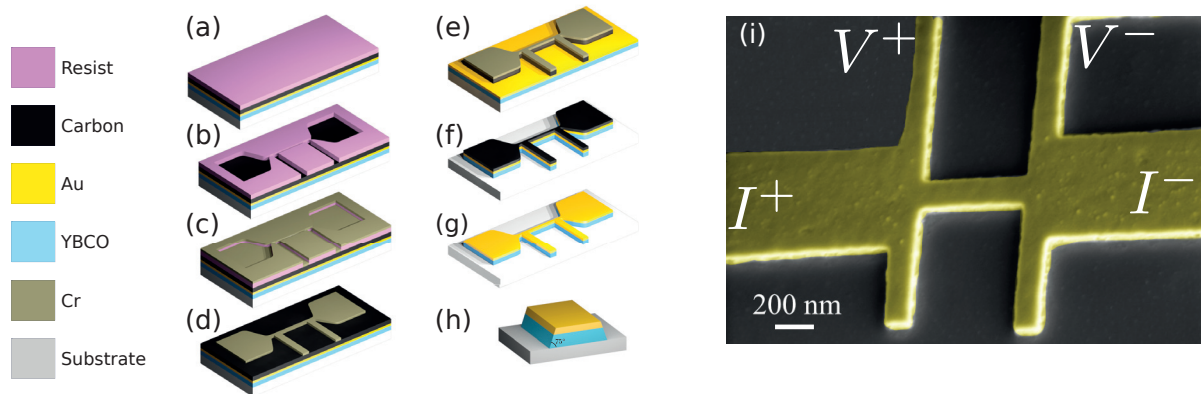


Figure 6.1: Process flow for defining YBCO 1EBL nanowires: (a) Single layer positive electron beam resist (thinned ZEP 520A in Anisole) is spun and baked at 85 °C, (b) the resist is exposed and then developed, (c) a 12 nm Cr film is used to metalize the entire sample, (d) the lift-off in acetone allows removing the Cr from the non-exposed areas, (e) reactive ion etching in oxygen removes the DLC film from the regions not covered by Cr, (f) the sample is etched using a gentle Ar-ion beam milling at 5°¹⁴⁶, (g) the fabrication of 1EBL devices is complete after stripping the residual DLC film in oxygen plasma, (h) Corresponding cross section of the device. (i) Scanning Electron Microscopy picture of the final device. In this configuration, the current is fed through the two wider electrodes, while the voltage drop across the nanowire is measured by the two narrower electrodes.

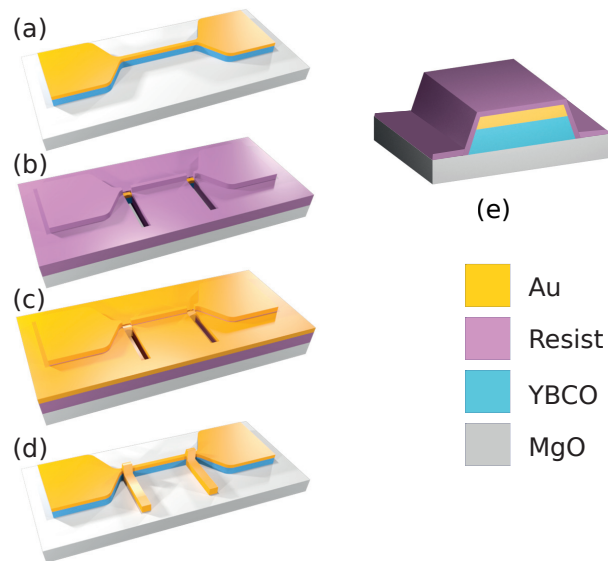


Figure 6.2: Fabrication process for defining 2EBL devices: (a) A YBCO nanowire capped with 20 nm in-situ Au is fabricated using top-down approach as described in Fig. 1(a-g), (b) single layer ZEP 520A resist is spun and exposed. (c) Metallization of the bilayer Au/YBCO with Pt/Au, (d) the 4-probe electrodes connecting nanowire to the bonding pads are defined by the lift-off technique. (e) The cross section of the device with a uniform coverage of the device with resist.

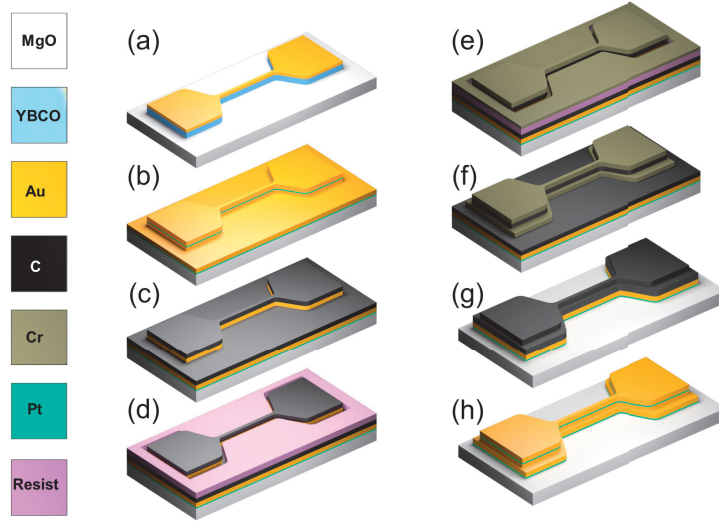


Figure 6.3: Fabrication flow to cover the edges of the nanowire with Pt/Au bilayer: (a) free standing YBCO nanowire capped with Au as fabricated with 1EBL, (b) the entire sample is covered by a sputter deposited bilayer of Pt/Au, (c) DLC carbon serving as a hard etching mask is deposited by PLD, (d) single layer, diluted resist (ZEP 520A: Anisole) is spun, exposed and developed, (e) Cr is deposited on the top of the sample, (f) Cr mask is obtained by the lift-off process, (g) the etching Cr-DLC mask is defined by stripping in O_2 plasma the regions not covered by Cr, (h) gentle Ar milling is used to remove Pt/Au film from the substrate regions. The residual DLC film on top of the nanostructure is removed in O_2 plasma.

Here, the nanowires are fabricated with the same method as 1EBL devices (Fig. 6.3(a)). Then a thin sputter-deposited film of Pt (10 nm) is used to improve the interface adhesion of the Au film on the MgO substrate. A 50 nm thick Au film is then sputtered on the entire chip including the side walls of YBCO structures (Fig. 6.3(b)). A pattern with slightly larger (30 – 50 nm) with respect to the already patterned nanowire layout is transferred in the second EBL procedure. This is done to ensure that all the YBCO edges remain protected by Pt/Au after the Ion milling etching of the Pt and Au layers (Fig. 6.3(h)).

The third and last EBL step is performed to define the narrow voltage probes (see Fig. 6.4(a-d)). With this type of electrodes configuration the temperature dependence of the resistive transition involves only the transition of the nanowire and not that of the wide electrodes.

6.2 FABRICATION DETAILS OF THE Au/YBCO INTERFACE RESISTANCE DEVICES

The Josephson coupling across a nanogap is strongly dependent on the interface transparency between the Au and YBCO, which determines the strength of the proximity effect in the Au layer.

The transmission line method (TLM), a classical method for measuring the interface contact resistances between two layers, has been used to measure the interface

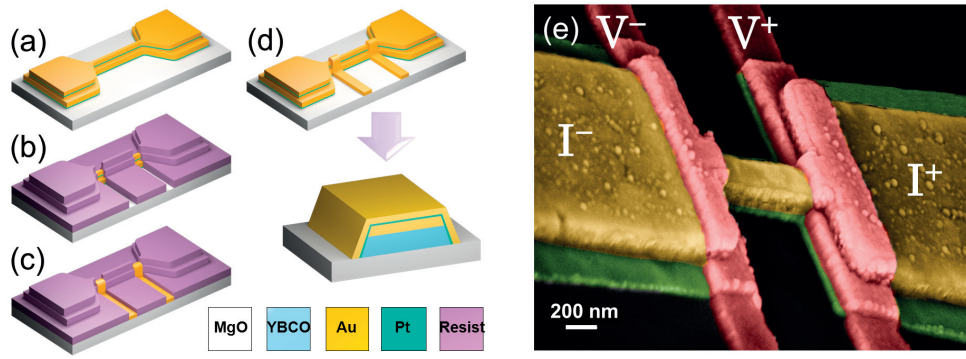


Figure 6.4: Schematic sketch of the process flow to fabricate the narrow voltage probes on the encapsulated YBCO/Au nanowires: (a) encapsulated Au/YBCO nanowire, (b) resist is spun, exposed and developed, (c) bilayer of Pt/Au is evaporated, (d) the fabrication of the sample is completed by the lift off of the Pt/Au layers. (e) SEM image of a 3EBL nanowire.

resistance between Au and YBCO. The theoretical basis of the TLM contact characterization method will be discussed in details in Section. 8.1. In brief, the TLM structure measures the total resistance of a system (both the electrical resistivity and the specific contact resistance (ρ_C) of the interfaces). The system we have analyzed consists of a series of identical $\text{YBa}_2\text{Cu}_3\text{O}_{7-\gamma}$ wires of width w_{YBCO} , spaced at varying intervals d_1 , d_2 , d_3 , which are connected by a Au bar of width w_{Au} .

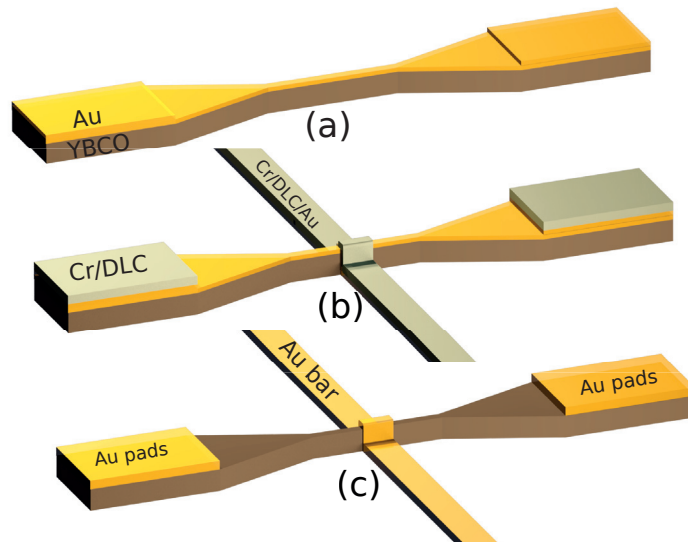


Figure 6.5: Schematic of process illustrating the fabrication of transmission line method structure for measuring the interface resistance between YBCO and Au. (a) The e-beam lithography is used to pattern the YBCO/Au film into the nanowire, (b) The entire sample is sputtered with Pt/Au bilayer and then the Au bar and Au pads are defined. (c) the carbon mask layer is removed by the oxygen plasma and then, by continue the Ar^+ ion milling, the Au layer from the YBCO nanowire is etched.

Three main fabrication steps are necessary to realize a TLM configuration (see Fig. 6.5):

- Patterning the *in-situ* Au/YBa₂Cu₃O_{7- γ} film into nanowires (see Fig 6.5(a)). We fabricated YBCO nanowires with different widths ranging from 100 nm to 500 nm. Later on in Section. 8.1, it will be clear that having junctions with different widths allows us to get more insight from the interface resistance of the top and sides of the YBCO/Au junction.
- Sputtering a bilayer of Pt/Au films and define Au bar connecting the wires employing e-beam lithography and etching through the C hard mask (see Fig 6.5(b)).
- Performing Ar⁺ ion milling to etch the Pt/Au and define Pt/Au bars. Once we etch Pt/Au layers we continue etching the Au on the top of the YBCO electrodes while it is completely removed (see Fig 6.5(c)).

Fig. 6.6 shows the SEM image of the final device.

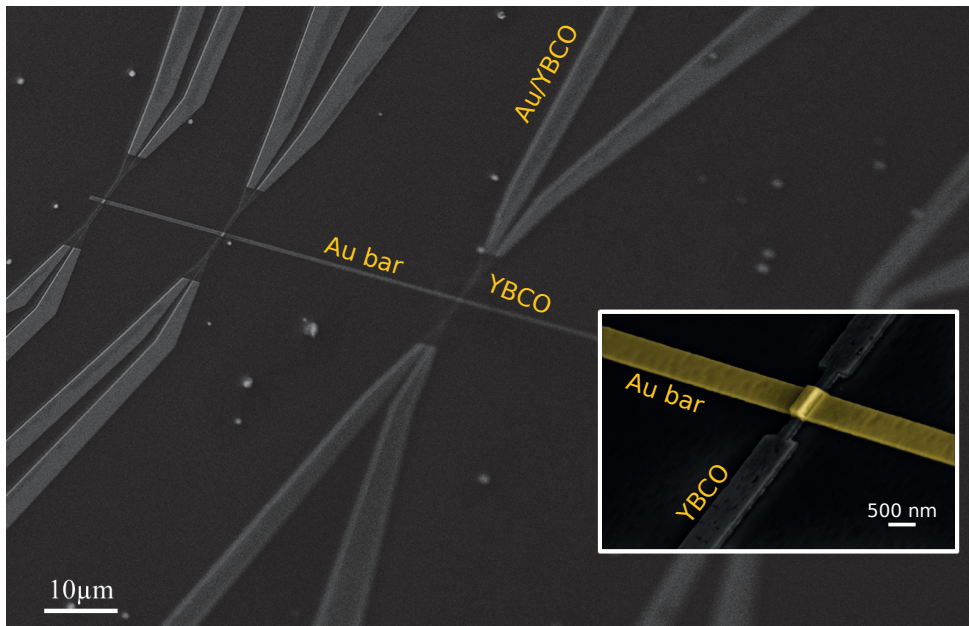


Figure 6.6: SEM image of TLM configuration to measure Au/YBCO interface resistance

6.3 FABRICATION DETAILS OF THE YBCO-AU-YBCO JUNCTIONS

Here, we discuss the novel fabrication process to realize high quality nanogap-based Josephson junctions. In this section, we briefly describe the fabrication process of mak-

ing planar YBCO-Au-YBCO junctions.

The fabrication process involves three EBL steps which are schematically depicted in Fig. 6.7(a)-6.7(c). Details on the fabrication are mentioned in Section 6.1.

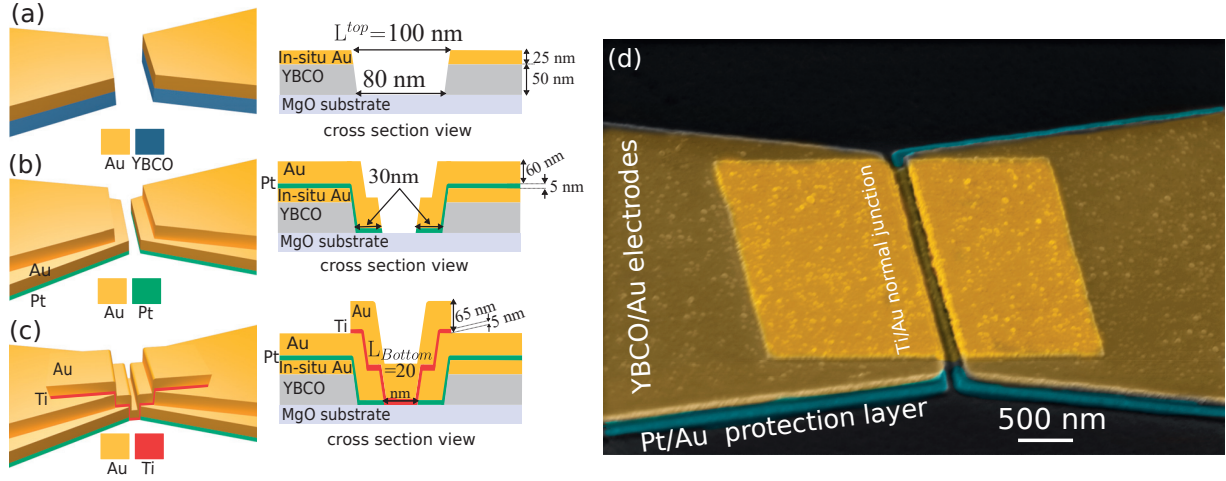


Figure 6.7: Schematic sketch of the process flow to fabricate the encapsulated YBCO/Au/YBCO junctions: (a) Nanogap formation: the pattern is transferred by the EBL to a diamond-like carbon mask and then to the Au/YBCO films by Ar^+ ion milling. Here, the top lateral spacing between the electrodes is 100 nm ($L^{\text{top}} = 100$ nm) but due to the line edge roughness, intrinsic of e-beam lithography process, and the edge's slope, the spacing between two YBCO electrodes at the bottom of the trenches shrinks to approximately 80 nm. (b) Encapsulation of the nanogap by patterning of the bilayer of Pt/Au (5 nm/60 nm). (c) Definition of the SNS junction. The distance L_{bottom} between the protected Au/YBCO electrodes is about 20 nm. (d) SEM image of a final SNS junction.

Briefly, to realize our devices, first a nanogap structure is defined on a high-quality, epitaxial *c*-axis-oriented 50-nm-thick $\text{YBa}_2\text{Cu}_3\text{O}_{7-\delta}$ films capped with 20 nm thick Au layer using EBL lithography. Then, a sputtered Pt/Au bilayer (5 nm/50 nm) films covered the entire chip including the side walls of YBCO nanogaps. A second EBL procedure is used to encapsulate the YBCO nanogaps. The transferred pattern is slightly larger (30 – 50 nm) with respect to the already-patterned nanogaps layout. The third and last EBL step is performed to define the Au normal metal to bridge the two YBCO electrodes. A SEM image of the typical 3EBL YBCO nanogap-based junction is shown in Fig. 6.7(d).

This page intentionally left blank.

7

Transport characterization of encapsulated YBCO nanowires

In this chapter we first focus on the electrical properties of nanowires fabricated with the three different procedures discussed in Ch. 6. We assess the damage induced by the nanofabrication procedure on the side and top of the 1EBL and 3EBL nanowires and discuss the role of an ozone treatment to restore the superconducting properties of the damaged region.

7.1 CRITICAL CURRENT DENSITY J_C AS A FUNCTION OF THE NANOWIRE WIDTH AND LENGTH

We assessed the superconducting performances of 1EBL, 2EBL, and 3EBL nanowires by studying their superconducting transport properties as a function of widths and lengths in the range of 60-700 nm and 1-10 μm . It is worth mentioning that the results, we present here, for each fabrication procedure are all from the same chip. All the measurements are carried out in a ^3He cryostat with a base temperature of 300 mK.

Fig. 7.1(a) shows the extracted critical current density J_C of different nanowires with $L = 1 \mu\text{m}$. As expected, the nanowire processed with one EBL step experienced a reduced number of fabrication steps and showed the maximum critical current density. The J_C of $6.1 \times 10^7 \text{A/cm}^2$ is obtained for a 200-nm-wide. (Fig. 7.1(a), blue circles). The reason that the highest J_C does not happen for the narrowest wire could be due to the very thin Au capping layer, 20 nm, we used as a YBCO protection layer (which is in the direction of our final goal to realize superconducting hybrid junctions). This

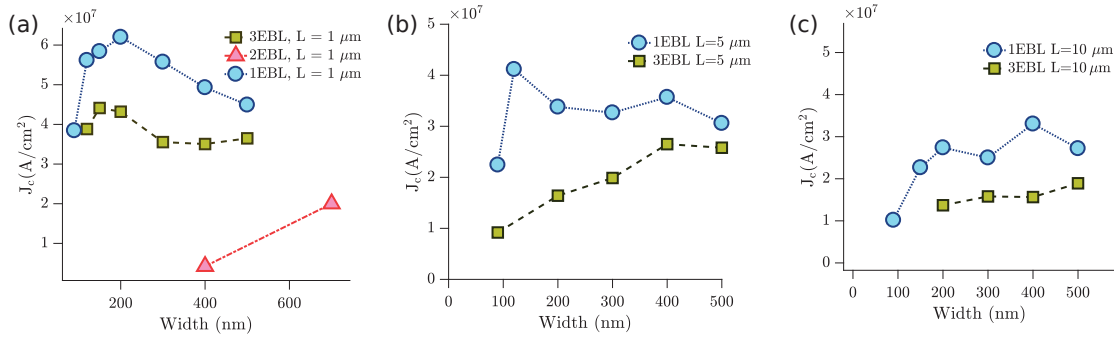


Figure 7.1: Critical current density J_C versus width w for 1EBL, 2EBL, and 3EBL nanowires with length (a) $L = 1 \mu\text{m}$, (b) $L = 5 \mu\text{m}$, (c) $L = 10 \mu\text{m}$

is because the superconducting proximity effect in nanogap-based Au/YBCO devices will be induced through the Au layer. A thinner Au capping layer will allow a stronger superconducting coupling through a normal barrier. In the recent study, Nawaz et al.¹⁴⁵ showed that that 50 nm is the minimum thickness of the Au capping required to preserve the pristine superconducting properties of the nanostructures.

For 1EBL samples, for widths above 200 nm, the J_C decreases by increasing the nanowire width which can be ascribed to current crowding effects¹⁴⁷. Current crowding effect can arise when the current passes at sharp edges in superconducting wire which leads to a decrease of the total critical current^{148,149}.

Fig. 7.1(b-c) shows the critical current density J_C for $5 \mu\text{m}$ and $10 \mu\text{m}$ long wires. It is clear that the maximum J_C value for 1EBL is reduced for a longer nanowire length (blue circles) and is almost independent of the width above 200 nm. The reason is that at such extended lengths, it is very possible that the critical current is mostly limited by the inhomogeneities in the YBCO film, rather than the current crowding effect.

The same J_C trend is also observed for 3EBL devices (see Fig. 7.1(a-c) green squares). For the 3EBL nanowires, the maximum critical current density J_C of $4.5 \times 10^7 \text{ A/cm}^2$ is achieved for a 150-nm-wide and 1- μm -long nanowire and is only about 20% lower than the values obtained for 1EBL. This proves that the superconducting characteristics of the encapsulated YBCO nanowires are well preserved even after several lithography processes which were demanded to cover the edges of the nanostructures with the Pt/Au bilayer.

As shown in Fig. 7.1(a), the 2EBL devices showed a very different behavior compared to the 1EBL and the 3EBL devices. First, the 2EBL devices do not show any superconducting transition for widths below 400 nm. This is due to the fact that in the 2nd EBL step, the resist and other chemicals get in direct contact with the edges of the patterned YBCO nanowire and deteriorate the superconducting properties of YBCO nanostructure significantly. This means that the damaged non-superconducting region extends approximately for about 200 nm from both lateral sides of the nanowire.

Therefore, YBCO nanogaps fabricated with 2EBL procedure would have an effective length $L_{\text{eff}} = 400 \text{ nm}$ larger than the geometrical-nominal one, which would make it very hard to observe the proximity-induced superconductivity in hybrid junctions¹⁵⁰. A significant reduction in J_C values is noticeable for the 2EBL nanowires with widths larger than 400 nm, in line with damaged nanostructures.

7.2 ESTIMATE THE LATERAL DAMAGE OF 1EBL AND 3EBL NANOWIRES

The realization of YBCO hybrid junctions is based on the fabrication of nanogaps. It is very crucial to understand how large is the degraded region of the YBCO electrodes. In our nanowires where the widths are much larger than the coherence length ξ , vortex crossing from one edge of wire to the other, perpendicular to the bias current, is the dominant mechanism of dissipation^{150–153} (see Section.3.2). We further characterize the nanowires fabricated with 1EBL and 3EBL devices, by measuring the resistance versus temperature $R(T)$.

Fig.7.2(a) shows the superconducting transition of both 1EBL and 3EBL devices of comparable widths. The change of resistance takes place over definite temperature interval which is a function of the nanowire width.

By fitting the $R(T)$ of nanowires using the thermal activation vortex entry (TAVE) model one can find the actual width of the sample. In this model, the thermal activation is responsible for the vortices to overcome the energy barrier and enter the superconductor.

The total measured resistance of 1EBL and 3EBL nanowires, close to transition, can be expressed as the parallel combination of two resistances. The first, R_v , is associated to the thermally activated vortex-entry resistance, and the second, R_{sh} , to the shunt resistance of the gold capping layer. Therefore, the total resistance can be written as:

$$R(T) = [R_v^{-1}(T) + R_{sh}^{-1}]^{-1}, \quad (7.1)$$

The value of R_{sh} corresponds to the resistance value measured at the onset of the superconducting transition, and R_v can be expressed as^{75,154}:

$$R_v(T) = 7.1 R_{\square} \frac{l\xi(T)}{\left(\frac{w_b+w_t}{2}\right)^2} \left(\frac{\epsilon_0(T)}{k_B T}\right)^{3/2} \exp\left(-\frac{U_{max}(T)}{k_B T}\right), \quad (7.2)$$

with

$$U_{max}(T) = \epsilon_0(T) \left(\frac{w_b \ln \frac{1.47 w_b}{\pi \xi(T)} - w_t \ln \frac{1.47 w_t}{\pi \xi(T)}}{w_b - w_t} - 1 \right). \quad (7.3)$$

In equations (7.2) and (7.3), R_{\square} and l are respectively the sheet resistance and the length of the wire, k_B is the Boltzmann constant and $\epsilon_0(T) = \Phi_0^2 t / 4\pi\mu_0 \lambda_L^2(T)$ is the

characteristic energy of a vortex in thin films, $\Phi_0 = h/2e$ is the superconducting flux quantum, and μ_0 is the vacuum permeability.

We've used the two fluid model temperature dependence for the temperature dependence of the London $\lambda_L(T) = \lambda_0 (1 - (T/T_C)^2)^{-1/2}$ where λ_0 is the zero temperature values of the London penetration depth. An approximated temperature dependence for the coherence length can be achieved from the Ginzburg-Landau depairing current density $J_d = \Phi/3\sqrt{3}\pi\mu_0\lambda_L^2(T)\xi(T)$ ¹⁵⁵, Eq. 3.12, and the Bardeen relation¹⁵⁶ for the temperature dependence of depairing current density $J_d(T) \propto (1 - (T/T_C)^2)^{3/2}$ characteristic of our nanowires¹⁴⁵ and almost all YBCO nanowires reported in literature¹⁵⁷. Therefore, the temperature dependence of the coherence length is given by $\xi(T) = \xi_0 (1 - (T/T_C)^2)^{-1/2}$, where ξ_0 represents the zero temperature values of the coherence length.

In recent studies^{153,158}, we have shown that by applying the TAVE model, the $R(T)$ measurements of YBCO nanowires with 1EBL and capped with a 50 nm thick Au layer can be fitted using a vortex entry model¹⁵⁴ by considering geometrical dimensions. In the fitting, we considered λ_0 (≈ 270 nm) and ξ_0 (≈ 2.5 nm) which are the typical values for YBCO thin films^{159,160}.

Eqs. 7.2 and 7.3 are the modified form of the expression we have previously adopted to the case where the cross-section of the nanowires is considered trapezoidal^{153,161}. Therefore, we have introduced the top width w_t and the bottom width w_b where $w_t > w_b$.

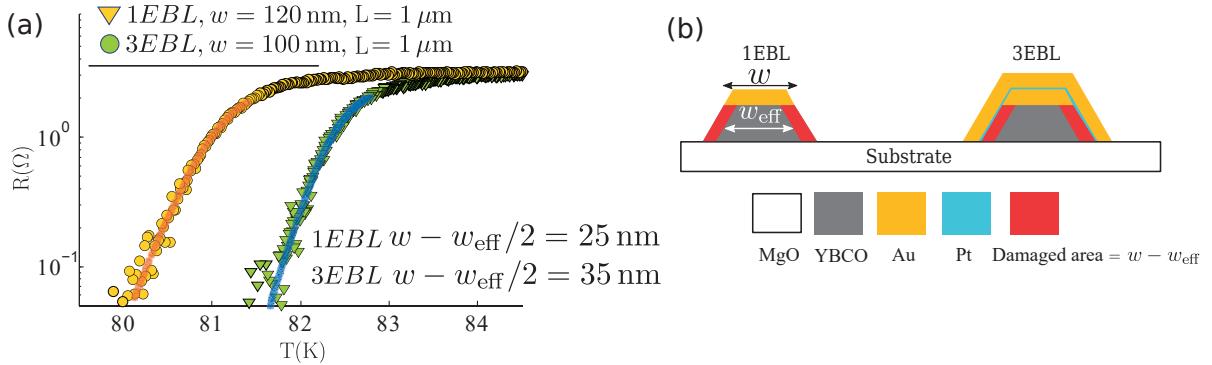


Figure 7.2: Resistance-temperature dependence of a 1EBL nanowire (green triangles) and of a 3EBL nanowire (yellow circles), having a comparable width with similar length. The nanofabrication processes cause local inhomogeneities and the oxygen out-diffusion in YBCO nanostructures which implies that a difference between the geometrical and effective widths should be considered for 1EBL and 3EBL nanowires. The measurements have been fitted with the thermally activated vortex-entry model (solid lines) using the typical values of λ_0 and ξ_0 for YBCO thin films and the same T_{C0} for both nanowires. We found damaged regions of 25 and 35 nm per edge for 1EBL and 3EBL devices, respectively. (b) Sketch of damaged area for 1EBL and 3EBL nanowires.

According to Eq. 7.2, by decreasing the nanowire width w and thickness t , the superconducting transition becomes broader.

As mentioned earlier, we used very thin Au capping layer compared to the state of the art nanowires fabricated with 50 nm Au. The superconducting transition of 1EBL

nanowires can be very well fitted with Eq. 7.2 by assuming a ≈ 25 nm damage on both lateral sides (see Fig. 7.2(b)), i.e. an effective width w_{eff} smaller than the geometrical one. Here, we considered the typical values for λ_0 (≈ 270 nm) and ξ_0 (≈ 2.5 nm) as we used in previous reports^{153,158}.

As expected, the 3EBL devices showed a larger broadening compared to 1EBL nanowires (see Fig. 7.2(a)). The transition broadening for the 3EBL nanowires can however be nicely fitted with the TAVE model (Eqs. 7.1-7.2) by assuming a damage of about 35 nm for each side which is slightly larger than the extracted damaged for the 1EBL nanowires. Such a small difference between the two systems can be explained by considering that local inhomogeneities and oxygen-out diffusion become more relevant as a consequence of multiple lithographic procedures. Similar to the 1EBL fitting process, we kept $\lambda_0 = 270$ nm and $\xi_0 = 2.5$ nm.

Here it is worth pointing out that the obtained w_{eff} from the $R(T)$ fitting, should be viewed as a measure of the non-homogeneities of the superconducting properties at temperatures close to T_C^{onset} . Particularly the "damaged" regions are affected by non-stoichiometric or oxygen-depleted paths which could be considered as superconducting regions with reduced T'_C where $T'_C < T_C$. Therefore, the damaged regions with possible superconducting transition T'_C do not provide supercurrent at temperatures close to T_C and consequently do not contribute to the fluctuation regime determining the broadening of the $R(T)$ transition.

Nevertheless, it is highly likely that at lower temperatures these regions contribute to the superconducting transport properties of the nanowire. One way to verify this scenario is by calculating the effective critical current density J_C^{eff} of the nanowire at $T = 300$ mK considering the effective width w_{eff} extracted from the $R(T)$ fitting. Table. 7.1 presents the J_C^{eff} at 300 mK for 1EBL and 3EBL nanowires (shown in Fig. 7.1) calculated considering w_{eff} expected from the fit and compares them with the low temperature limit of the Ginzburg-Landau depairing critical current density $J_{\text{dep}}^{\text{GL}}$ which has a value of $\approx 6 \cdot 10^7$ A/cm². Here, for calculating the $J_{\text{dep}}^{\text{GL}}$ we considered $\lambda_0 \approx 270$ nm and $\xi_0 \approx 2.5$ nm³⁶.

The values of J_C^{eff} are about 50% larger than the theoretical depairing value. Therefore, one can conclude that the w_{eff} at 300 mK has to be substantially larger than the effective width w_{eff} extracted from $R(T)$ measurements at temperatures close to T_C and consequently the damaged regions on both sides of the nanowires can be considered to have $T'_C < T_C$ and do contribute to the superconducting transport at lower temperatures.

Table 7.1: Critical current densities $J_C = I_C(T = 300 \text{ mK})/w$ of 1EBL and 3EBL nanowires ($L = 1 \mu\text{m}$), measured at 300 mK and presented in Fig. 7.1(a), are compared to the effective critical current densities $J_C^{eff} = I_C(T = 300 \text{ mK})/w_{\text{eff}}$. Here the effective width is given by $w_{\text{eff}} = w - 50 \text{ nm}$ for the 1EBL nanowires and by $w_{\text{eff}} = w - 70 \text{ nm}$ for the 3EBL nanowires. These J_C^{eff} values are higher than measured critical current density J_C in the low temperature limit, assuming $\lambda_0 \approx 270 \text{ nm}$ and $\xi_0 \approx 2.5 \text{ nm}$.

device	$J_C = I_C/(w \cdot t)$ (A/cm ²)	$J_C^{eff} = I_C/(w_{\text{eff}} \cdot t)$ (A/cm ²)
1EBL $w = 90 \text{ nm}$	$3.84 \cdot 10^7$	$8.64 \cdot 10^7$
1EBL $w = 120 \text{ nm}$	$5.62 \cdot 10^7$	$9.63 \cdot 10^7$
1EBL $w = 150 \text{ nm}$	$5.84 \cdot 10^7$	$8.76 \cdot 10^7$
1EBL $w = 200 \text{ nm}$	$6.20 \cdot 10^7$	$8.27 \cdot 10^7$
3EBL $w = 120 \text{ nm}$	$3.88 \cdot 10^7$	$9.31 \cdot 10^7$
3EBL $w = 150 \text{ nm}$	$4.41 \cdot 10^7$	$8.27 \cdot 10^7$
3EBL $w = 200 \text{ nm}$	$4.32 \cdot 10^7$	$6.65 \cdot 10^7$

7.3 OZONE TREATMENT

To investigate the significance of oxygen out-diffusion while doing the nanopatterning of YBCO films (mostly during ion milling and resist baking) and if is possible to enhance the superconducting properties of our devices, we promoted an ex-situ ozone treatment^{154,161} which allows us to re-oxygenate the YBCO nanostructures after and/or in the middle of the fabrication process. The ozone treatment has been already used to improve the superconducting properties of YBCO thin films and nanostructures^{162,163}.

We perform the ozone treatment by heating up the sample at a temperature $T \sim 150 \text{ }^\circ\text{C}$ inside a chamber which is equipped with an ultraviolet (UV) lamp. The chamber is then filled with oxygen gas at atmospheric pressure. When oxygen atoms are exposed to UV light, they absorb photons, dissociate and react with other oxygen molecules/atoms to form ozone O_3 . The sample is kept for 2 hours in such an environment, then cooled down slowly. It is then kept at room temperature for 2 more hours in ozone atmosphere.

7.3.1 OZONE TREATMENT ON BARE YBCO FILMS

We begin by assessing the effectiveness of ozone treatment on the superconducting properties of a 50 nm thick c -axis YBCO film, deposited on a MgO (110) substrate. As discussed in Ch. 5, by changing the deposition conditions (i.e. p and T) one can obtain YBCO films with different level of doping. In this study, we first finely tuned the deposition conditions to grow overdoped YBCO films and then by reducing the post-annealing oxygen pressure during the cool-down phase, we managed to obtain nearly optimally doped films with a T_C of 89.1 K, which is a record value for YBCO films

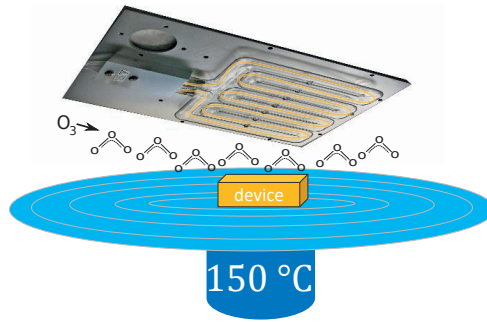


Figure 7.3: Sketch of the ozone system used to re-oxygenate YBCO films and nanostructures. The YBCO films are kept in ozone ambient at 150°C for 2 h. Then the heater is turned off and the ozone flow is kept on for additional 2 hours while the sample is cooling down.

grown on MgO substrates. However, there is still a slight difference between this value of T_C and the T_C of optimally doped bulk YBCO. The lattice mismatch between the in-plane lattice parameters of the YBCO film and the MgO substrate imposes strain to the YBCO film which could lead to a decrease in the T_C of the film. Fig. 7.4 shows the $R(T)$ characteristics of the nearly optimally doped (red diamonds) and overdoped YBCO films (yellow triangles).

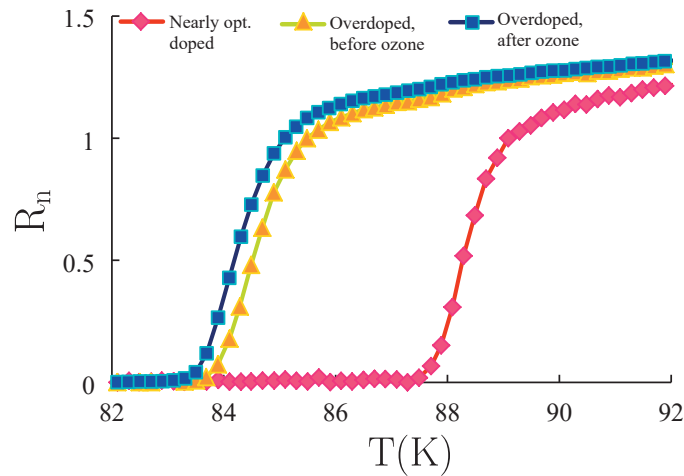


Figure 7.4: Normalized $R(T)$ characteristics of an overdoped 50 nm thick YBCO film grown on MgO (1 1 0) substrate, before (yellow triangles) and after (blue squares) ozone treatment. The transition temperatures are respectively 3.8 K and 4.0 K lower with respect to the nearly optimally doped YBCO film (red diamonds).

By applying the ozone treatment, we managed to increase even further the oxygen doping level of the overdoped YBCO films. As a result, the T_C of the overdoped films slightly decreased by about 0.2 K, which means that the film is more overdoped (see blue squares in Fig. 7.4).

To confirm we are adding up oxygen to the film, we have studied the structural

properties of the thin YBCO films by performing X-ray diffraction (XRD). The increase in oxygen doping is accompanied by a compression of the c -axis length¹⁴³ which can be also detected in X-ray spectra.

Fig. 7.5 shows the symmetrical 2θ - ω scans on the nearly optimally doped films and on the overdoped film, both before and after the ozone treatment. The 2θ - ω scans show only the (00ℓ) reflections which is a confirmation that the films are c -axis oriented and highly crystalline. Though all the XRD patterns look similar, their (00ℓ) peak positions differ slightly. One can estimate the c -axis length of the YBCO films from the position of each (00ℓ) peak. We have observed that the value of the c -axis length decreases with increasing oxygen doping (moving from the nearly optimally doped to the overdoped sample) reinforcing the fact that the films with a reduced T_C are in the overdoped regime (see Fig. 7.5 and the corresponding inset).

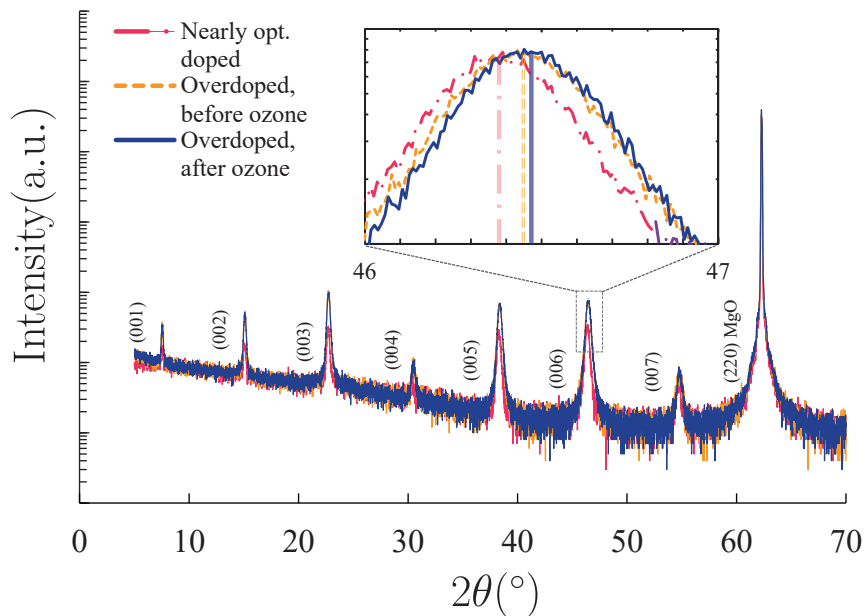


Figure 7.5: $2\theta - \omega$ X-ray diffraction pattern of a nearly optimally doped (red dash-dotted line) and of the overdoped YBCO film, before (yellow dashed line) and after (blue solid line) the ozone treatment (the same films as Fig. 7.4). Only the (00ℓ) YBCO reflections, typical of c -axis grown films, are observed. The increase in oxygen doping is associated with the shrinkage of the c -axis length. This fact is clear in the (006) reflections of the three films. The inset shows the enlarged (006) peak. A compression of the c -axis of the overdoped films with respect to the nearly optimally doped film is observed. The same trend is observed for the overdoped film after ozonation.

Table. 8.2 summarizes the extracted values of the c -axis length from several (00ℓ) peaks. The compression of 0.009 of the c -axis value confirms the further increase of the oxygen doping after the ozonation. This observation supports the effectiveness of the ozone treatment to add oxygen to the YBCO thin film.

Table 7.2: extracted values of the c -axis of YBCO from the XRD $(0\ 0\ \ell)$ reflections of the nearly optimally doped (NOP) film and of the overdoped film, both before (OBO) and after (OAO) the ozone treatment.

Sample	c^{003} (Å)	c^{004} (Å)	c^{005} (Å)	c^{006} (Å)	c^{007} (Å)	c^{avg} (Å)
NOP	11.744	11.743	11.741	11.737	11.742	11.741
OBO	11.727	11.727	11.728	11.726	11.728	11.727
OAO	11.718	11.719	11.719	11.719	11.719	11.719

7.3.2 OZONE TREATMENT ON YBCO NANOWIRES

We have studied the consequence of the ozone treatment on YBCO 1EBL and 3EBL nanowires. Fig. 7.6 summarizes the critical current densities J_C as a function of the width w for 1 μm long 1EBL nanowires before and after ozone treatment. An enhancement in the range 15-20% is clearly visible for all the widths.

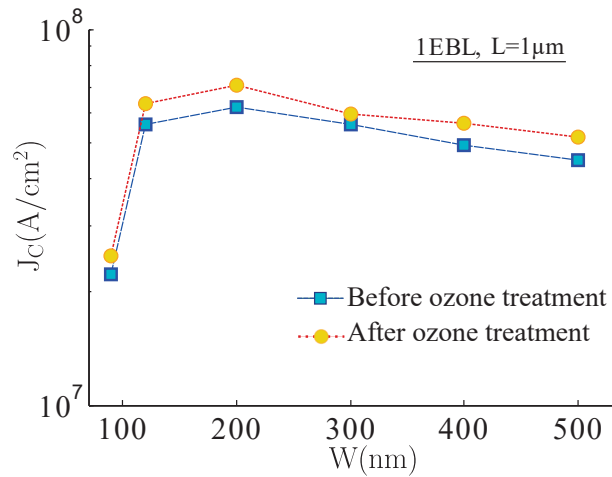


Figure 7.6: Critical current densities J_C of 1 μm long 1EBL nanowires, measured before and after the ozone treatment, as a function of the wire width.

We have also studied the impact of the ozone treatment on the $R(T)$ measurements of 1EBL nanowires fabricated on the overdoped YBCO films. Fig. 7.7 shows the $R(T)$ transition of 1EBL YBCO nanowire before and after the ozone treatment. The oxygenated nanowires show a smaller superconducting broadening which can be fitted with thermally activated vortex entry model, Eqs. 7.1-7.2, considering no lateral damage on the sides. For the same nanowire we had to consider a 15 nm lateral damage to fit the $R(T)$ transition before the ozone treatment.

We have also performed ozone treatment on longer nanowires, and we could observe that the impact of oxygenation is even stronger in the longer nanowires. As already shown in Fig. 7.1(b-c), there is a considerable reduction in the J_C for longer nanowires. One could improve the J_C value significantly by doing the ozone treatment. Fig. 7.8(a) shows the IV and $R(T)$ characteristics of a 90 nm wide and 5 μm long nanowire before

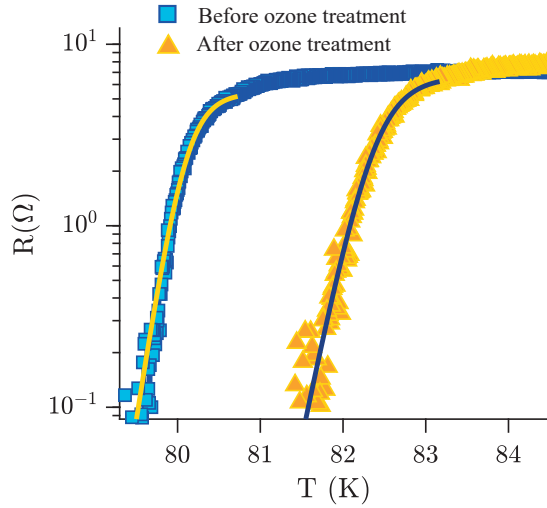


Figure 7.7: The $R(T)$ measurement of 1EBL YBCO nanowire before (yellow triangle) and after (blue squares) ozone treatment. The broadening of the resistance transition becomes sharper and the T_C decreases after ozonation which is a direct indication that the YBCO structures take in oxygen.

and after ozonation. Lower T_C and higher J_C are strictly linked to a shift in the oxygen doping of the YBCO nanostructures towards the overdoped region of the YBCO phase diagram¹⁶¹. The increase of critical current after the ozonation can be up to 200% for $10\ \mu\text{m}$ long nanowires (see Fig. 7.8(b)). Moreover, in very long and narrow 1EBL nanowires the superconducting transition is not only quite broad, but it also presents a bump, which could be associated with deoxygenated regions with the size of the nanowire cross section having a lower critical temperature (see inset of Fig. 7.8). In such cases, the ozonation procedure makes the transition narrower and reduces the bump, making the nanostructure more uniform.

In principle, the 3EBL nanowires could benefit in the same way from the ozone annealing as the 1EBL. However, the ozonation can act differently depending on whether it is performed after the first or the third lithographic step.

As a result of fast oxygen mobility in the a - b planes with respect to the c -axis direction^{163,164}, the oxygenation of nanostructures mostly occurs through the lateral sides of the nanowires. Saying that, the 3EBL nanowires experience the same effect observed in 1EBL ones (see Fig. 7.6) if the ozone treatment being performed after the first lithographic step, before the wire is encapsulated by the Pt/Au bilayer.

The impact of ozonation on already encapsulated nanowires (3EBL) is quite different. For such a structure, the Pt/Au which is used as the encapsulation layer act as a barrier possibly blocking oxygen from entering into the YBCO nanostructure. The T_C of such nanowires increases after ozone treatment with a slight reduction in the

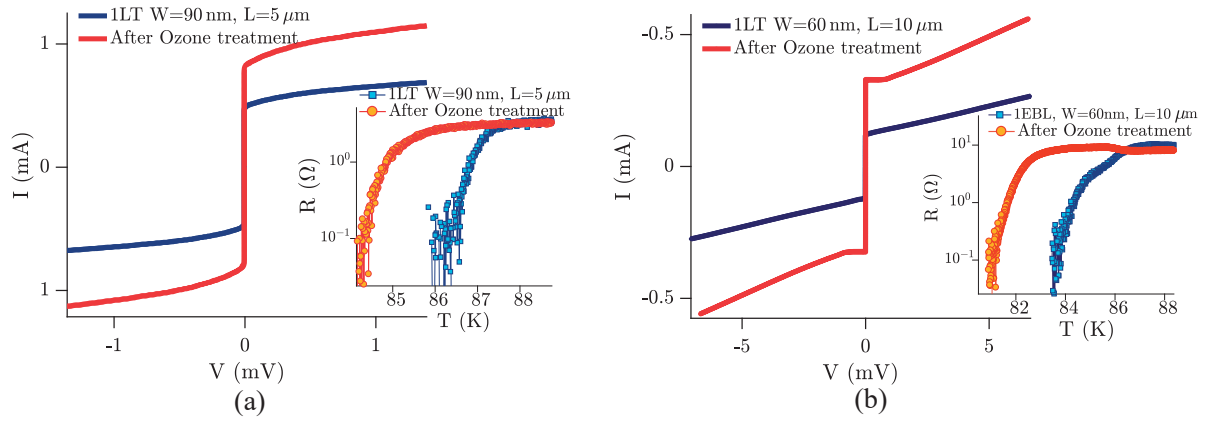


Figure 7.8: Current Voltage characteristic of a (a) 90 nm wide and 5 μm long (b) 60 nm wide and 10 μm long 1EBL nanowire before and after ozone treatment. The insets shows the resistive transition of the same nanowires before and after ozonation is shown. As a consequence of ozone treatment decreases T_C in the range of 2-3 K.

superconducting transition broadening (see Fig. 7.9). Applying the thermally activated vortex entry model on the $R(T)$ measurements revealed that the damaged region reduced by 5-10 nm from both sides of the nanowire after undergoing the ozone treatment (solid lines in Fig. 7.9).

Moreover, by looking into the IVCs of the 3EBL we realize that the IVCs of the 3EBL nanowires before and after ozone treatment are quite similar; in some case the J_C is slightly reduced. This manifestation suggests that the ozone treatment does not increase the oxygen content, but it homogenizes the oxygen content within the encapsulated YBCO nanostructures.

In some cases, the ozone treatment is capable of healing the highly damaged YBCO nanowires. Fig. 7.10 shows the IVC of a 90 nm wide and 10 μm long nanowire, which is characterized by a residual resistance. However, after the ozone treatment, because of the homogenization of the oxygen content through the YBCO film, the IVC of the nanowire shows a well-defined superconducting transition.

One can conclude that, even though the ozone treatment in 3EBL nanowires does not increase the oxygen content of the YBCO nanowire, it homogenizes its stoichiometry, redistributing the oxygen atoms and healing regions where the superconductivity is absent. This picture is supported by the slight increase of T_C signifying a lower global oxygen doping due to the redistribution of oxygen atoms in the damaged regions and the consequent reduction of J_C .

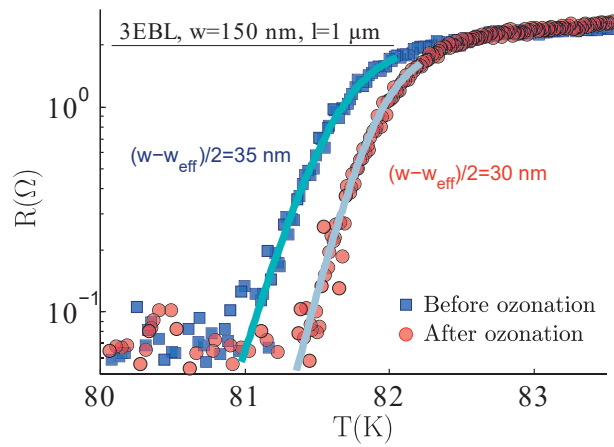


Figure 7.9: Resistance versus temperature of a 3EBL nanowire before and after the ozone treatment. Differently from the 1EBL nanowires the main effect is an increase of the critical temperature. In addition, a reduction of 0.2 K in the transition broadening is visible: the data after ozonation can be fitted with the vortex entry model, assuming a reduced damage of the nanostructure on the sides with respect to that we can estimate before the ozone annealing (the blue and gray lines represent the two fits to the data).

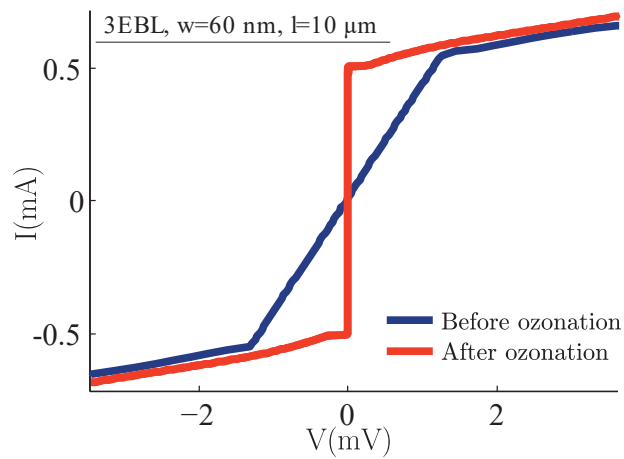


Figure 7.10: IV characteristic measured before and after the ozone treatment on a 90 nm wide, 10 μm long 3EBL nanowire: as a consequence of the ozonation, the wire, which previously exhibits a residual resistance in his IVC present a supercurrent at zero voltage.

8

Transport characterization of YBCO-Au-YBCO junctions

As already shown in Ch. 7, we successfully managed to fabricate YBCO nanowires encapsulated with the Pt/Au bilayer to avoid the YBCO nanostructures being in direct contact with any chemicals or resists in subsequent fabrication steps. Furthermore, we showed that the value of the critical current densities J_C of the so-called 3EBL nanowires are very close to the J_C values of the nanowires fabricated in a single EBL process (1EBL or "reference" nanowires).

In addition to preserving the superconducting properties of YBCO during fabrication, one needs also to be sure that high transparency interfaces are formed between YBCO and in-situ Au film as well as YBCO and Pt/Au layer, since the proximity-induced gap inside the normal region strongly depends on the interface transparency of the junction.

In this chapter, we first investigate the interface contact resistance in a YBCO/Au junction, applying the transfer line method (TLM) configuration. Then, we look into YBCO/Au/YBCO junctions and discuss their transport properties.

8.1 YBCO/AU INTERFACE CONTACT RESISTANCE

To measure the contact resistance between the *in-situ* Au and $\text{YBa}_2\text{Cu}_3\text{O}_{7-\gamma}$, we fabricated four $\text{YBa}_2\text{Cu}_3\text{O}_{7-\gamma}$ nanowires, in parallel with each other and spaced $30\ \mu\text{m}$, $60\ \mu\text{m}$ and $90\ \mu\text{m}$ from each other respectively. A gold bar perpendicular to the wires connects the YBCO electrodes making a TLM configuration (see section 6.2 for more

details regarding the fabrication process). A schematic representation of the interface contact resistance configuration is given in Fig. 8.1(a). The equivalent electrical circuit consists of two Au/YBa₂Cu₃O_{7- γ} interface resistances $R_{C_{1,2}}$ and the gold bar resistance $R_{Au} = r_{Au}l$ where r_{Au} is the Au resistance per unit length and l is the length of the gold bar connecting the two YBCO nanowires (see Fig. 8.1(b)). Therefore we have:

$$R_{tot} = r_{Au}l + R_{c_1} + R_{c_2}. \quad (8.1)$$

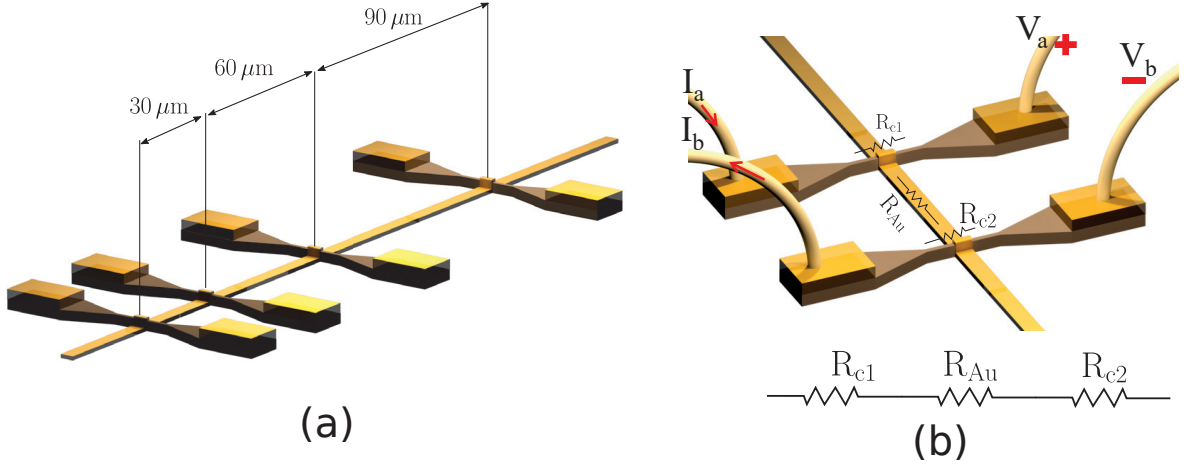


Figure 8.1: (a) Schematic presentation of the TLM configuration to measure the interface contact resistance in YBCO/Au interfaces, (b) the resistance between two nanowires consists of three resistances in series: two Au/YBCO contact resistances and the Au bar resistance connecting two nanowires.

As can be seen from Eq. 8.1, R_{tot} varies linearly with the length of the Au bar and consequently, by measuring the resistance between the different wires in all possible configurations (corresponding to the length of the gold bar being 30 μm , 60 μm , 90 μm , 150 μm , and 180 μm) and plotting them as a function of the length between the wires, one could obtain, in principle, the contact resistance $R_c = R_{c_1} + R_{c_2}$ as the intercept of the y -axis in a linear fit of R_{tot} as a function of the length l .

Beyond measuring the total Au/YBCO contact resistance, one can also distinguish the contributions of the top and the sides of the wires to the total contact resistance. Fig. 8.2 shows the AFM image of an Au/YBCO junction and its equivalent circuit.

The total interface contact resistance consists of three resistances in parallel, as illustrated in Fig. 8.2. Therefore, the total contact conductance is given by

$$G_c^{tot} = 2G_c^{side} + G_c^{top} = 2G_c^{side} + g_c^{top}A, \quad (8.2)$$

where G_c^{side} and G_c^{top} are respectively the conductance of the side and the top contacts. Accordingly, g_c^{top} is the contact conductance of the top interface per unit area A . The

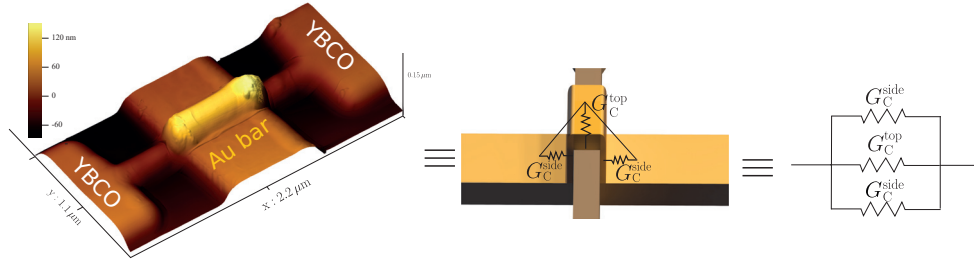


Figure 8.2: The AFM image and the equivalent schematic presentation of a single Au/YBCO junction. The total interface conductance G_C^{tot} is a sum of two interface conductances of the side contact G_C^{side} and the interface conductance of the top contact G_C^{top} .

side contact conductance can be extracted from the intercept of the linear fit of G_C^{tot} as a function of the top area, while the slope gives the contact conductance of the top surface per unit area.

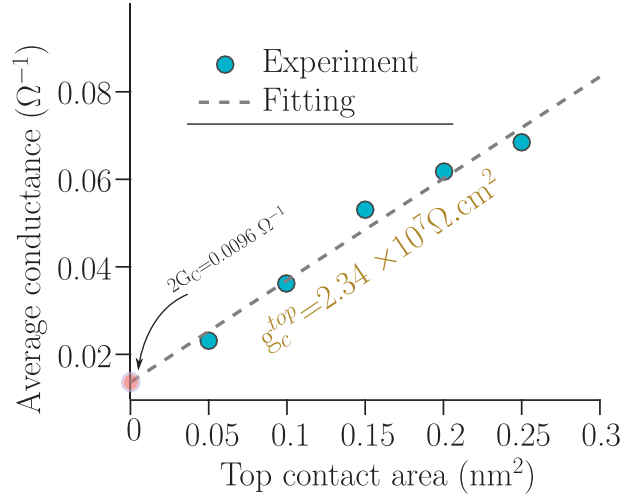


Figure 8.3: The average total conductance as a function of the area of top contact. The slope of the linear fit corresponds to the conductivity of the top surface.

Fig. 8.3 shows the average value of the interface conductance as a function of the top contact area of the YBCO/Au contact estimated from the low-bias conductance values. We extract the top and side contact values $\rho_c^{top} = 4.27 \times 10^{-8} \Omega \text{ cm}^2$ and $\rho_c^{side} = 5.14 \times 10^{-8} \Omega \text{ cm}^2$, respectively, where $\rho_c^{top, side}$ are resistance times unit area. These values are among the best reported in the literature¹⁶⁵⁻¹⁶⁷, corroborating the potentiality of the nanogap for proximity hybrid devices. This result is quite encouraging considering that the top Au/YBCO interface is made *in-situ* while the side one is formed after the etching of the YBCO nanowires.

The measured conductance is the combination of two *SN* junctions connected in a

back to back configuration (see Fig. 8.4). The $G(V)$ characteristic of the measured SN contacts revealed an anomalous voltage dependence (blue line in Fig. 8.4) which could be fitted with V^α with $\alpha = 0.5$ in the low-bias regime (dotted yellow curve in Fig. 8.4). This kind of dependence has been previously observed in amorphous $\text{Ge}_{1-x}\text{Au}_x$ films¹⁶⁸ suggesting that the density of states of the compound is in proximity of the metal-insulator transition. In our case, the total conductance is the contribution of both the top and side contacts. In particular, the side interface undergoes an oxygen loss during the patterning of the nanowire which leads to a YBCO layer at the interface which could have degraded superconducting properties and possibly close to the metal-insulator transition.

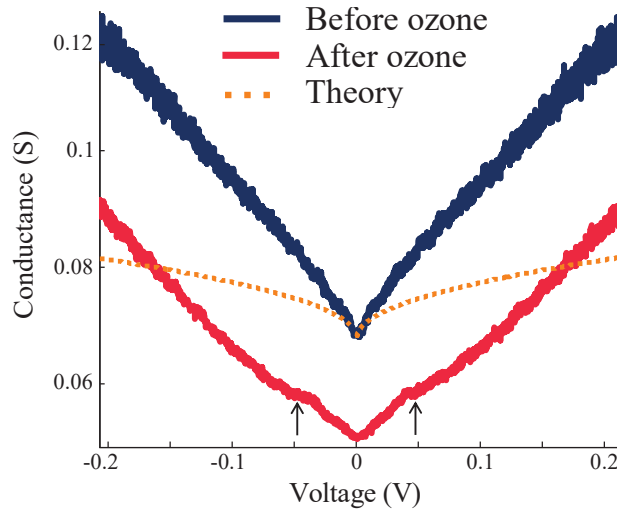


Figure 8.4: Typical conductance of the YBCO/Au junction as a function of the voltage across the junction before (blue) and after (red) ozone treatment. After ozonation, the conductance showed the superconducting gap at $V = 50$ mV which is associated with two SN junctions.

After ozone treatment the low-bias conductance anomaly disappeared and, instead, the junction showed a clear tunnel-like behavior in its $G(V)$ curve with the distinct appearance of a gap structure at $V \sim 50$ mV which is twice the value of the YBCO gap at the optimally doped regime. This value is consistent with the fact that the measurement involves two interfaces in series. The appearance of the superconducting gap feature in the conductance curve is a strong indication of a restored Au/YBCO interface.

In addition to the occurrence of the superconducting gap in the $G(V)$ curve, we also observed that the value of the conductance is reduced after the ozone treatment. The reason is unclear. A possible explanation is that the ozonation is performed after the fabrication is completed. From the work on the nanowires we have learned that at this stage it is the temperature (150°C) rather than the ozone that has an important role,

leading to a redistribution of oxygen inside YBCO. It is possible that this redistribution restores the superconductivity in close proximity of the interface while still leaving a depleted region within ξ (from the interface) which leads to a tunnel barrier.

8.2 TRANSPORT PROPERTIES OF YBCO-AU-YBCO JUNCTIONS

The fabrication process of making planar YBCO-Au-YBCO junctions is based on the encapsulation method and fully discussed in Section. 6.3. Fig. 8.5 shows the schematic and the SEM image of a final YBCO-Au-YBCO junction. Here, we will study the transport properties of these junctions.

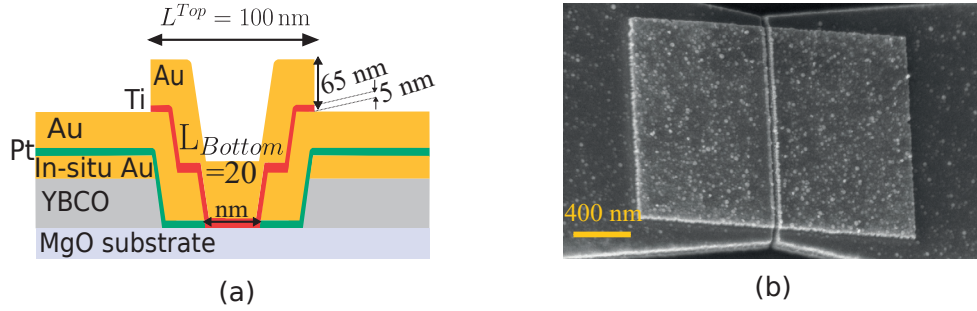


Figure 8.5: (a) schematic presentation of the SNS junction with $L^{Top} = 100$ nm. (b) Typical SEM image of a YBCO-Au-YBCO junction.

We have characterized the transport properties of several YBCO-Au-YBCO junctions with widths $2 \mu\text{m}$ and $3 \mu\text{m}$ and different interdistance lengths ranging from 60 nm to 120 nm. All the measurements were performed in a ^3He cryostat with a base temperature of 300 mK (see Appendix. D).

Fig. 8.6 shows the current-voltage characteristics of a junction (SNS #1) with width $w = 2 \mu\text{m}$ and a separation $L^{Top} = 100$ nm for the range of temperature (5 – 78 K). We have measured a critical current density $J_C = 1.45 \text{ MA/cm}^2$ at $T = 5 \text{ K}$ and $J_C = 38 \text{ kA/cm}^2$ at $T = 73 \text{ K}$. A clear transition from a flux-flow like behavior at very low temperature to a Resistively Shunted Junction (RSJ) behavior at temperature close to T_C of the device ($T_C = 75 \text{ K}$) is observed. This phenomenology is often observed in magnetically long junctions when the Josephson penetration depth λ_J is much longer than the width w ¹⁶⁹.

Since the YBCO film thickness is smaller than the London penetration depth λ_L , the Josephson penetration depth has to be calculated by considering non-local electrodynamics^{84,90–93}. At low temperature ($T = 5 \text{ K}$) we obtained, using Eq. 3.17, $l_J = \Phi_0/4\pi\mu_0\lambda_L^2 J_C \sim 210 \text{ nm}$. For the same junction, this value raises to about $1.5 \mu\text{m}$ at high temperature ($T = 73 \text{ K}$) where the junction behaves more like a magnetically short junction ($w \sim 2l_J$).

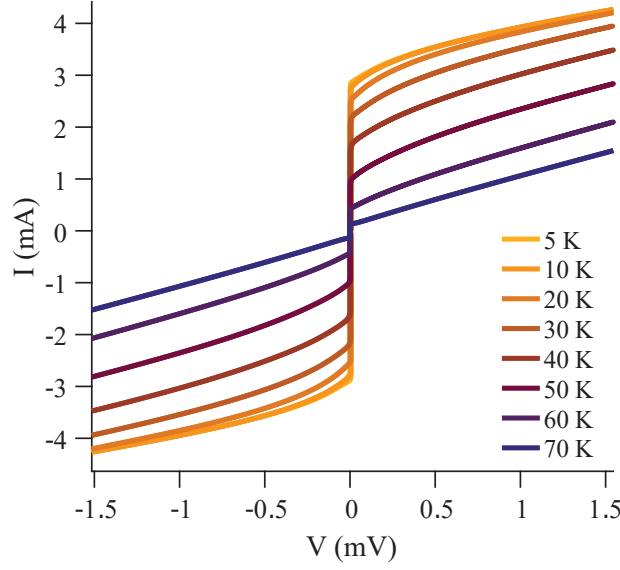


Figure 8.6: Current-voltage characteristic of the junction SNS #1 at various temperatures.

For the junction (SNS #1), we applied an external magnetic field normal to the film and measured the current-voltage characteristics (IVCs). From all those IVCs at various magnetic fields we then calculated the logarithmic differential conductance of the junction as a function of the applied magnetic field and current of the junction. Fig. 8.7(a-f) shows the magnetic measurements at different temperatures.

As just mentioned, at low temperatures the junction is in the long limit ($w \gg l_J$) and due to the self-field effect, the magnetic pattern $I_C(B)$ is slanted and a maximum of the critical current modulation does not occur at $B = 0$ T (see Fig. 8.7(a-b)). While at higher temperatures, the SNS junction behaves as a junction in the intermediate regime ($w \sim 4l_J$) and we observe a close to Fraunhofer-like dependence of the Josephson current^{36,81,170} as shown in Fig 8.7(c-d).

From the magnetic pattern at $T = 73$ K, one can determine a magnetic modulation period $\Delta B \sim 1$ mT (distance between the side lobes) which is in agreement with the predicted value for the thin-film planar junctions, Eq. 3.20, $\Delta B \sim 1.84\Phi_0/w_J^2$ ⁸⁹ considering $w_J \sim 1.95 \mu\text{m}$.

In this limit, since the junction width w is still comparable with the Josephson penetration depth l_J , the influence of the Josephson current induced magnetic field is considerable and one expects the screening currents around the junction resulting in the critical current to drop linearly with increasing the applied magnetic field as $I_C(B) = I_C(0)(1 - |B|/B_C)$ ^{83,169,171}. As a result, the position of the first minimum in the $I_C(B)$ pattern is larger than the ΔB .

Let's now look at another SNS junction (SNS #2) with the same width w but with an electrode interdistance of $L^{Top} = 120$ nm. The magnetic pattern of the junction for

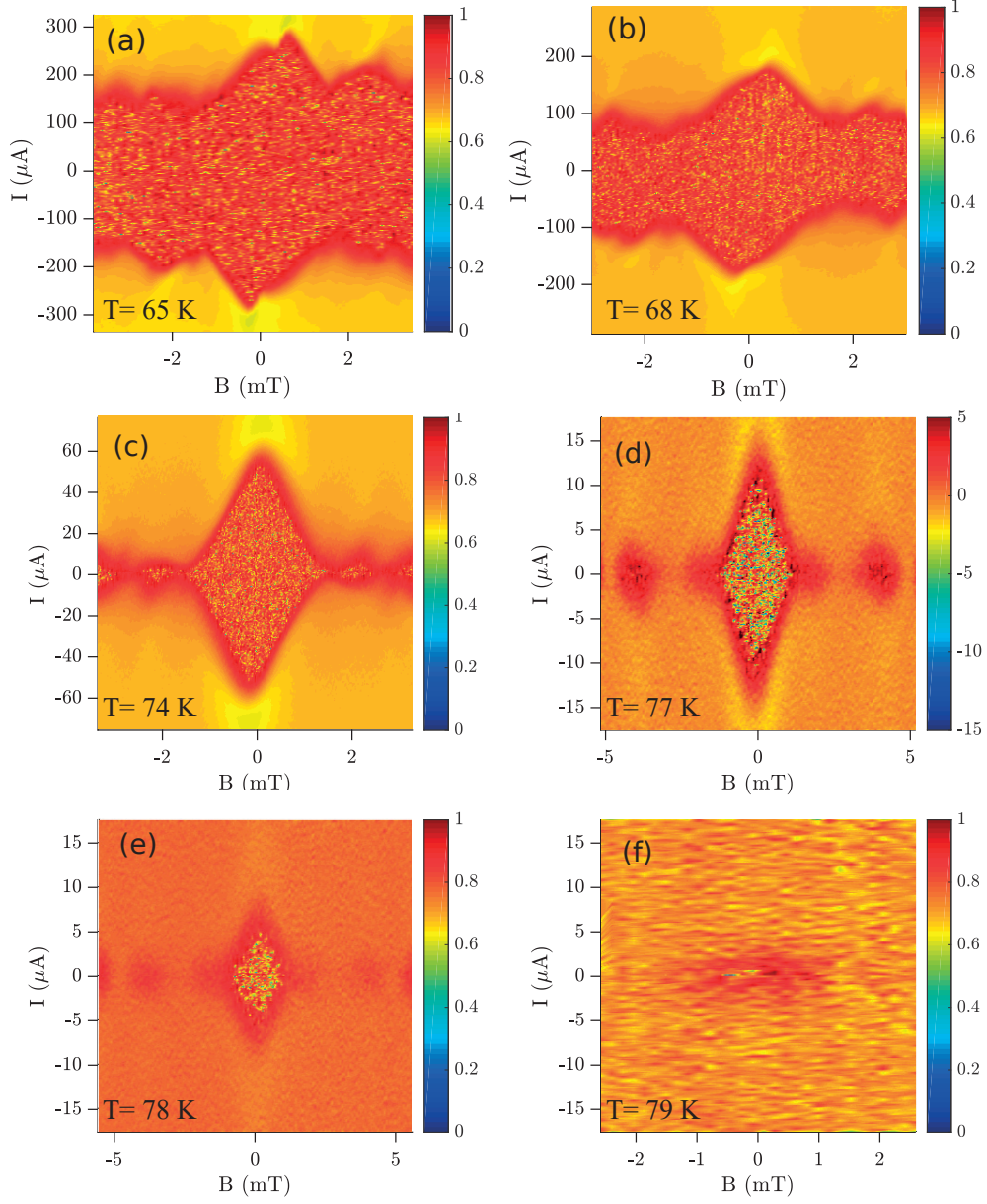


Figure 8.7: Normalized logarithmic conductance map as a function of bias current and external magnetic field for an SNS junction with width $w = 2 \mu\text{m}$ and $L^{Top} = 100 \text{ nm}$ at several temperatures: (a) $T = 65 \text{ K}$, (b) $T = 68 \text{ K}$, (c) $T = 74 \text{ K}$, (d) $T = 77 \text{ K}$, (e) $T = 78 \text{ K}$, (f) $T = 79 \text{ K}$.

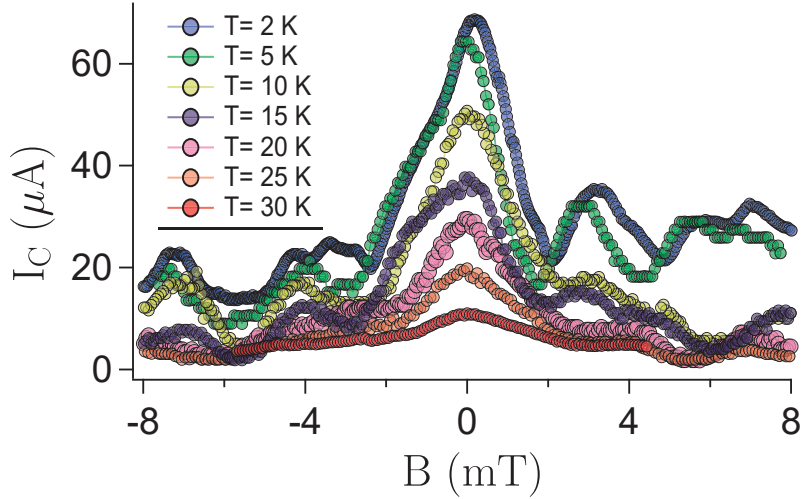


Figure 8.8: The magnetic modulation of the critical current at a series of temperatures for the junction with $w = 3 \mu\text{m}$ and $L^{T_{op}} = 120 \text{ nm}$ (SNS#2).

a range of temperatures is shown in Fig. 8.8. We observe a Fraunhofer-like dependence in the range of temperature from 2-30 K.

Due to the longer gap, the SNS junction showed a reduced critical current density $J_C = 35 \text{ kA/cm}^2$ at $T = 5 \text{ K}$ which is associated with a Josephson penetration depth of $l_J = 1.55 \mu\text{m}$. The value of l_J is close to the width of the junction already at low-temperature. Moreover, one can obtain the $\Delta B \approx 2.7 \text{ mT}$ suggesting an effective width of $w = 1.18 \mu\text{m}$ which is not too far from the geometrical width.

8.3 SHAPIRO STEPS

As discussed in Section. 3.5, the appearance of Shapiro steps in the current-voltage characteristics is an important tool to study the dynamic properties of a Josephson junction.

Fig. 8.9(a) shows the suppression of the Josephson current for the junction (SNS #1) as a function of the applied microwave at a fixed power. We can see that at $f = 3.11 \text{ GHz}$ the suppression of I_C is strong which indicates that at this frequency the coupling is very effective. Fig. 8.9(b) shows the IV characteristics of the junction at different amplitude of the rf-signal ($f = 3.11 \text{ GHz}$). The power dependence of the critical current and the height of the first two Shapiro steps are shown in Fig. 8.9(c). Fig. 8.9(d) shows the 2D logarithmic differential conductance map as a function of the bias current and $P^{1/2}$ at the fixed frequency ($f = 3.11 \text{ GHz}$)*. Higher order Shapiro steps can be observed.

*Here P is the microwave power at the output of the microwave source.

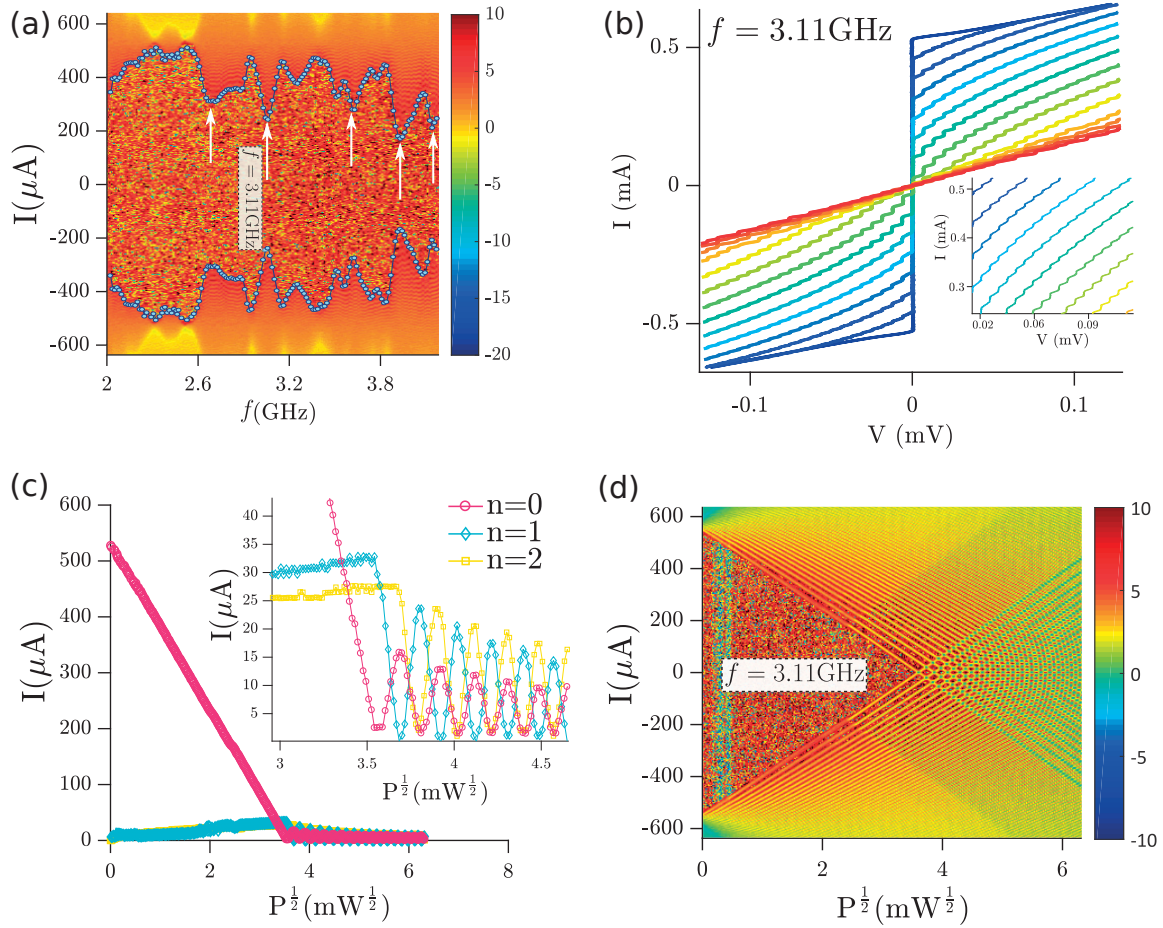


Figure 8.9: (a) Logarithmic differential conductance map as a function of irradiated microwave frequency f and of the junction current taken at 65 K. The envelope of the curve is the frequency dependence of the critical current (white circles). (b) IV characteristics of the junction taken at $f = 3.11\text{GHz}$ for various microwave irradiation powers. The appearance of Shapiro steps is very clear at $V_n = n\Delta V$ where $\Delta V = 6.44\ \mu\text{V}$. (c) Power dependence of the critical current ($n = 0$) and the height of the 1st and 2nd Shapiro steps. (d) Logarithmic differential conductance map as a function of the microwave irradiation power and the junction current taken at $f = 3.11\text{GHz}$. Above measurements are for the junction (SNS #1).

In different samples, we have also observed anomalous half-integer Shapiro steps in the current-voltage characteristics. Fig. 8.10 shows the IVCs of a SNS junction ($w = 2 \mu\text{m}$ and $L^{Top} = 100 \text{ nm}$) under microwave excitation at the frequency $f = 1 \text{ GHz}$ (colored lines). The half-integer Shapiro steps are better visible on the differential conductance curve.

The formation of the half-integer Shapiro steps in SNS junction has been already reported in long planar HTS SNS junction¹⁷² and attributed to the $\sin(2\varphi)$ term in the current-phase relation of the junction. In our junction the high transparency of the YBCO/Au interfaces could lead to an unconventional CPR with a pronounced second harmonic term.

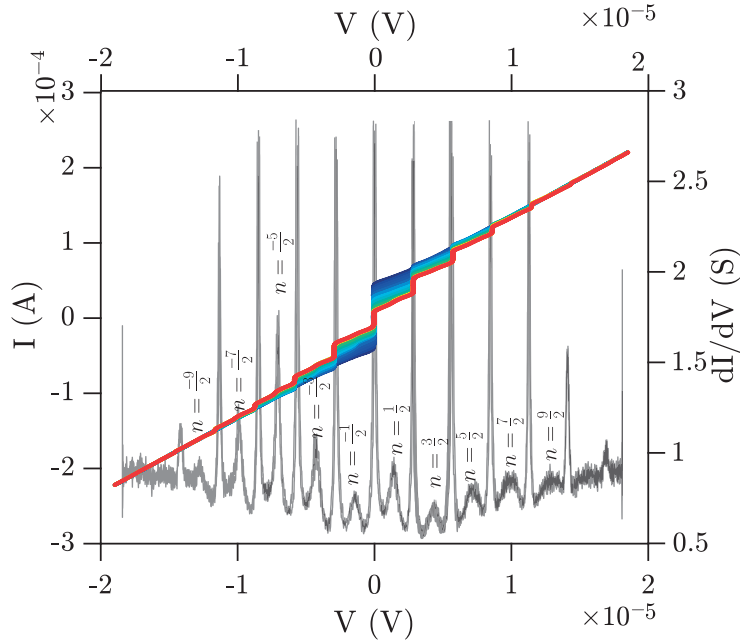


Figure 8.10: IV characteristics of the SNS junction under microwave irradiation ($f = 1 \text{ GHz}$) for different rf power (the irradiation frequency is 1 GHz). Pronounced Shapiro steps are clear with a separation of $\Delta V = 2.1 \mu\text{V}$. These current steps are also visible as peaks in differential conductance (dI/dV). Beside the steps at $n\Delta V$ where $n = \pm 1, \pm 2, \dots$, the occurrence of half-integer Shapiro steps at ($n = \pm \frac{1}{2}, \pm \frac{3}{2}, \dots$) is also clear.

8.4 TEMPERATURE DEPENDENCE OF THE CURRENT IN YBCO-AU-YBCO JUNCTIONS

As we discussed in Ch. 4, by studying the behavior of the Josephson current as a function of the temperature, we can get information on Cooper pair transport through the normal conductor. Here we discuss three SNS junctions with different electrode distance L . To analyze the $I_C(T)$ dependence we have used the SINI'S theoretical model discussed in Section. 4.5.

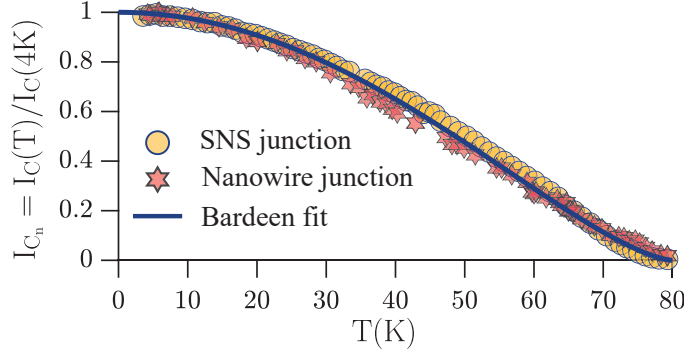


Figure 8.11: Normalized critical current as a function of temperature for a YBCO-Au-YBCO junction with $L^{Top} = 60$ nm (yellow circles), and of a YBCO nanowire with $w = 90$ nm (red hexagram). The Bardeen expression is also shown (navy dark blue solid line).

Let's first analyze the $I_C(T)$ of a SNS junction with a very short electrode distance. Fig. 8.11 shows the normalized $I_C(T)/I_C(4K)$ of an SNS junction with $L^{Top} = 60$ nm and $w = 3 \mu\text{m}$ (Yellow circles). The $I_C(T)$ characteristic of this junction is very similar to the one of a nanowire with $W = 90$ nm, where W is the width of the nanowire (red stars). Using the expression $I_C(T)/I_{C_0} = (1 - (T/T_C)^2)^{3/2}$ †¹⁵⁶, calculated by Bardeen we can nicely interpolate both curves for the full range of temperatures (dark blue solid line).

This evidence leads us to conclude that the electrodes forming the YBCO nanogap are possibly shorted. Here we discuss plausible scenarios which could be responsible for the occurrence of these shorts.

As a result of Ar ion milling, necessary to fabricate YBCO nanogaps, the sidewalls of YBCO electrodes have finite slope. In Fig. 6.7(c) we have shown that this effect together with the unavoidable line edge roughness due to e-beam lithography procedure, result in a distance of the electrodes, in the bottom of the trench of approximately 20 nm for nominal nanogap of $L^{Top} = 100$ nm. It is therefore quite possible that nanogaps with nominal $L^{Top} = 60$ nm are shorted at the bottom.

As a rough estimation of the thickness of the leftover YBCO layer at the bottom of the trench connecting the electrodes, one can assume that the SNS junction critical current $I_C = 12.1$ mA is due to a YBCO nanoshort at the bottom of the nanogap. Considering that nanowires made with 3EBL procedure have $J_C \sim 50$ MA/cm² (see Fig. 7.1(a)) a critical current of 12 mA is achieved for thickness $t' \sim 4 - 5$ nm of YBCO (considering $w = 3 \mu\text{m}$ which is the width of the junction). This tiny leftover YBCO layer can be the result of a high aspect ration trench where the width of the gap is only

†It is shown that the Bardeen relation for temperature dependence of the critical current is valid for YBCO nanowires¹⁴⁵.

half of the initial YBCO/Au thickness.

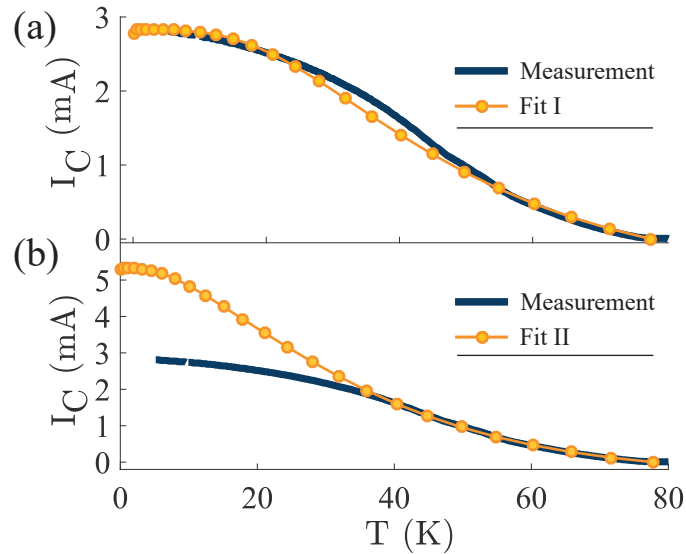


Figure 8.12: Measured (blue line) and theoretical (yellow circles) $I_C(T)$ for the junction (SNS #1). The Fitting parameters are listed in the Table. 8.1

Fig. 8.12 shows the critical current as a function of the temperature for the device (SNS #1) with $L^{Top} = 100$ nm. To fit $I_C(T)$ measurement with Eq. 4.20, we assumed a value $\Delta \approx 16.5$ meV for the superconducting energy gap at the interface YBCO/Au in agreement with and what we have found experimentally¹⁵⁴ and what is reported by Sharoni et al.¹⁷³. As many parameters are involved in the SINIS model, there is not a unique set that can fit our data (see Table. 8.1).

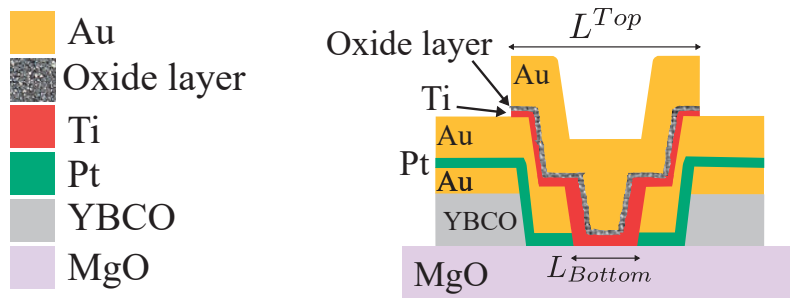


Figure 8.13: Cross section of a SNS junction. Because of the ozone treatment on our SNS junctions, it is plausible that a very thin oxide is formed at the Ti/Au interface. The oxide layer makes the transport of Cooper pairs more desirable through the Ti layer.

In Fig. 8.12(a), by assuming two different transparencies at the SN interfaces we managed to achieve a good agreement between our data and the theory. From the fitting (see parameters for the Fit I in Table. 8.1), we learned that the proximity current

is through the thin Ti layer which we employed as a sticking layer. Indeed the extracted thickness of the bridging value is the same as the thickness of the Ti film.

The obtained junction length L is comparable with the one extracted at the bottom edge of the nanogap L_{Bottom} (see Fig. 8.13). This scenario could be due to the ozone treatment on our junction. Even though the ozone treatment is needed and is expected to improve the degraded YBCO layer at the interface, on the other hand, it could be responsible for the formation of a very thin oxide at the Ti layer. Because of this extra barrier, the Cooper pair transport is more favorable through the Ti in contact with the substrate (see Fig. 8.13).

Table 8.1: Fitting parameters used in the fit I and II for the junction (SNS #1). Here h is the thickness of superconducting channel and $\mathcal{T}_{1,2}$ are the transparencies of Au/YBCO interfaces.

	L (nm)	w (nm)	h (nm)	\mathcal{T}_1	\mathcal{T}_2	Δ_0 (meV)	T_C (K)	l_e (nm)
Fit I	11.5	500	5	0.18	1	16.5	77.8	5
Fit II	13	500	5	0.55	0.55	16.5	77.8	5

Although this fit looks very promising, we cannot trust it completely. The reason is twofold. First, the huge discrepancy in the interface transparency values \mathcal{T}_1 and \mathcal{T}_2 cannot be easily justified considering the fabrication process. Moreover, we don't expect any good theoretical fit at low temperatures. This is because the junction is in the long junction limit at low temperatures and it also shows a slanted magnetic pattern (see 8.7(b)) which is an indication that it behaves more like an asymmetric in-line junction (see Fig. 3.6). Although our SNS junction doesn't have an in-line configuration, the small value of l_J at low temperatures together with possible nonuniformity of the interface transparency may result in an inhomogeneous J_C which makes the junction to emulate an in-line behavior. It is known that, in this regime, the critical current is saturated for $w > 4l_J$ ^{81,83,87} and I_C does not anymore scale with the junction width w .

Considering these facts, we have fitted the high-temperature region of the I_C measurement by considering quite transparent and identical interfaces. (see Fig. 8.12(b)). The obtained parameters for this fit are listed in Table. 8.1 (Fit II). The fit is reasonable in the high-temperature regime where the junction is in short limit. The higher expected theoretical values compared with the experimental ones at low temperatures supports the fact that the junction is in long junction limit and it is not possible to fit the $I_C(T)$ measurements in the low-temperature regime. Furthermore, in this case we get that the Cooper pair transport is through the Ti layer and also the length of the junction is comparable to what is expected from geometrical considerations.

Fig. 8.14 shows the $I_C(T)$ dependence for the junction (SNS #2) with $L^{Top} = 120$ nm. For this junction, we considered the same T_C value as for the junction (SNS #1). The fitting parameters for this junction are listed in Table. 8.2.

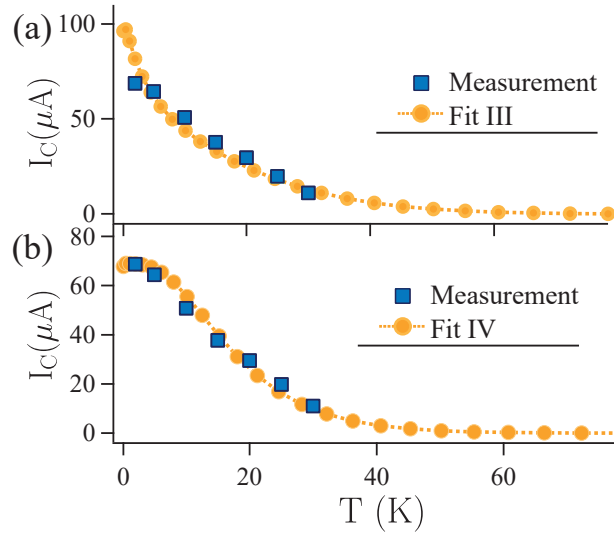


Figure 8.14: Measured (blue squares) and theoretical (yellow circles) critical current vs temperature for the junction (SNS #2) discussed in Fig. 8.8.

Using $L \approx 17$ nm and $h = 5$ nm, we get a good agreement between experiment and theory by considering identical transparencies. The extracted value of the thickness h reinforces the argument that the leading transport channel is through the 5 nm thick Ti layer at the interface with the substrate. Furthermore, comparing the obtained length for the junction (SNS #1) (Table. 8.1), the increase in the L to about 20 nm (Table. 8.2), is in line with the fact that the top length L^{Top} is 20 nm larger for the junction (SNS #2). Also for this junction a reasonable fit can be obtained by considering asymmetric barriers' transparencies.

Therefore, by using a double barrier SINI'S model, we have studied the transport properties of the critical current in temperature. The results of the fitting suggest that the Cooper pair transport is mainly across the 5 nm Ti sticking layer due to the ozone treatment. This circumstance should be considered for further implementation of this nanogap in complex devices.

Table 8.2: Fitting parameters used in the fit III and IV for the junction (SNS #2).

	L (nm)	w (nm)	h (nm)	\mathcal{T}_1	\mathcal{T}_2	Δ_0 (meV)	T_C (K)	l_e (nm)
Fit III	17	500	5	0.09	0.09	16.5	77.8	5
Fit IV	20	500	10	0.0122	1	16.5	77.8	73

9

In-plane transport anisotropy of a -axis oriented YBCO nanodevices

The superconducting YBCO has an anisotropic crystal structure with a poor coupling between the CuO_2 planes along the c -axis which results in a weak superconductivity along this direction.

In this Chapter, we will discuss the measurements of nanowires and nanoSQUIDs fabricated on untwinned a -axis YBCO films oriented at different in-plane angles γ with respect to the $[0,1,0]$ direction of the LSGO substrate.

9.1 STUDY OF THE IN-PLANE ANISOTROPY IN a -AXIS YBCO NANOSTRUCTURES

Some studies have been reported on the anisotropy of critical current density of YBCO films^{174–177}. In the work carried out by Dinger et al.¹⁷⁴, the anisotropic behavior of the critical current density and the critical field of single crystals of YBCO have been demonstrated.

In this work, we studied the in-plane anisotropy of the critical current density in nanoscale a -axis systems. To do this, we have patterned, on the same chip, nanowires and Dayem bridge nanoSQUIDs protected by a Au capping layer with width down to 65 nm at different in-plane angles γ with respect to the $[001]$ direction of the substrate. The fabrication details are fully described in Ch. 6.

Fig. 9.1 shows the SEM image of a typical nanowire along the b - and c -axis. For the nanowires along the b -axis direction, $\gamma = 0^\circ$, the supercurrent is passing along the a - b planes. While the current is along the c -axis direction for $\gamma = 90^\circ$.

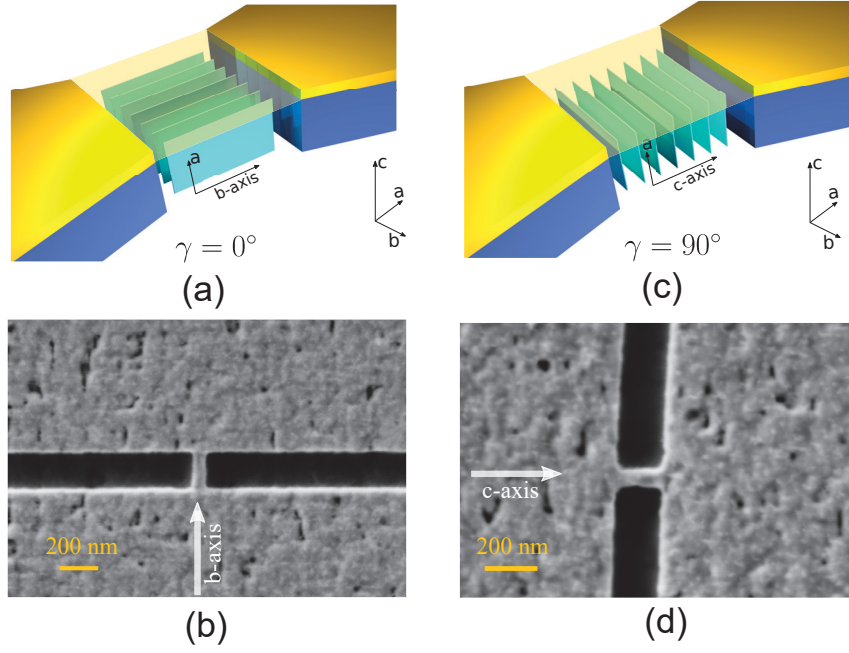


Figure 9.1: (a) Schematic representation of a *b*-axis aligned YBCO nanowire, where the current flowing from one electrode to the other is in the *a*-*b* planes. (b) Scanning electron microscopy image of a nanowire with width $w = 65$ nm patterned along the *b*-axis and (d) *c*-axis.

The critical current density, $J_C = I_C/(w \cdot t)$ for 140 nm wide nanowires patterned at different in-plane angles γ is shown in Fig. 9.2. A clear anisotropy of the critical current density is visible: for $\gamma = 0^\circ$, the J_C is maximum and as the γ increases it reduces and eventually by approaching to $\gamma = 90^\circ$, the value of J_C drops by one order of magnitude.

The J_C dependence on γ is a result of the anisotropy of the coherence length ξ and of the London penetration depth λ_L in the *a*-*b* plane and in the *c*-axis direction.

Considering an anisotropic thin ($t < \lambda_L$) superconductor and applying the approach discussed by Bulaevskii et al.⁷⁵, one can calculate the critical current densities for a wire ($w > 4\xi$) oriented along the *b*-axis (for $\gamma = 0^\circ$)

$$J_C^b \propto \frac{\Phi_0}{\lambda_b \lambda_c \xi_c}, \quad (9.1)$$

and for a wire oriented along the *c*-axis for $\gamma = 90^\circ$

$$J_C^c \propto \frac{\Phi_0}{\lambda_b \lambda_c \xi_b}. \quad (9.2)$$

Here, the product $\lambda_b \cdot \lambda_c$ in the dominator reflects the fact that the circulating screening current of the Abrikosov vortex is flowing in the $[100]$ planes of the crystal. i.e. along

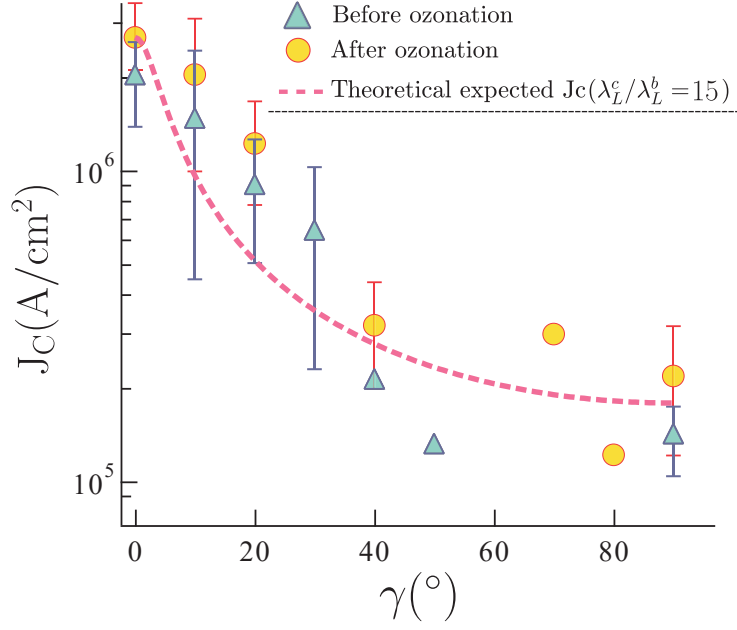


Figure 9.2: Average critical current density J_C vs the angle γ for the 140 nm wide a -axis YBCO nanowires before (blue triangles) and after (orange circles) the ozone treatment. For each angle, the error bar, related to the broadening of the distribution of the J_C values measured on identical nanowires, is equal to 2σ . The theoretical J_C^λ related to a London anisotropy $\lambda_c/\lambda_b = 15$ is shown as a solid line.

the b - and c -axis. In Eqs. 9.1 and 9.2, the relevant coherence length is along the direction of the vortex entry path which is perpendicular to the current flow.

Moreover, the thermodynamic critical magnetic field can be given by

$$B_C^{th} = \frac{\Phi_0}{2\sqrt{2}\pi\lambda_L^b\xi_b} = \frac{\Phi_0}{2\sqrt{2}\pi\lambda_L^c\xi_c}. \quad (9.3)$$

From Eq. 9.3 and Ref. ¹⁷⁸ one can obtain the following equality between the London penetration depth and the coherence length for b - and c -axis

$$\frac{\lambda_c}{\lambda_b} = \frac{\xi_b}{\xi_c}. \quad (9.4)$$

Inserting Eq. 9.4 in Eqs. 9.1 and 9.2 results in

$$\frac{J_C^b}{J_C^c} = \frac{\lambda_c}{\lambda_b}. \quad (9.5)$$

For a generic γ we need to consider an effective London penetration depth ($\lambda_{\text{eff}}(\gamma) = \sqrt{\lambda_b^2 \cos^2 \gamma + \lambda_c^2 \sin^2 \gamma}$) calculated in Ref. ^{178,179}. We therefore have

$$\frac{J_C(\gamma)}{J_C^b} = \frac{\lambda_b}{\lambda_{eff}} = \frac{1}{\sqrt{(\cos^2 \gamma + (\frac{\lambda_c}{\lambda_b})^2 \sin^2 \gamma)}}. \quad (9.6)$$

In Eq. 9.6 the $J_C(\gamma)$ is dependent on the ratio λ_L^c/λ_L^b which can be calculated roughly from the magnetic field modulation of nanoSQUIDs (see Fig. 9.6). We fabricated Dayem bridges nanoSQUIDs formed by two 65 nm wide nanowires oriented along b/c -axis. In our nanoSQUIDs, because of the very narrow bridges, the total loop inductance L_{loop} is dominated by the kinetic inductance which can be determined by λ_L^b and λ_L^c .

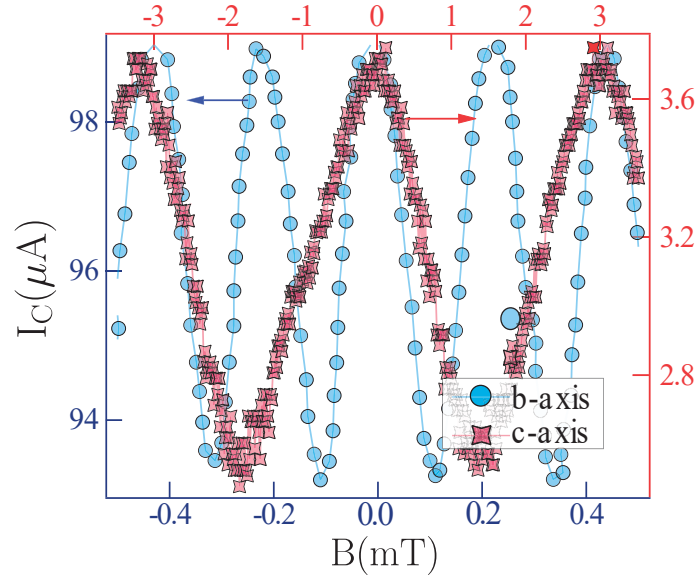


Figure 9.3: Critical current modulation as a function of an externally applied magnetic field for b -axis (blue circles) and c -axis (red squares) aligned 65 nm wide Dayem bridge nanoSQUIDs ($T = 4$ K).

The experimental loop inductance can be estimated from the relation $L_{loop}^{exp} = \Phi_0/\Delta I_C$, where Φ_0 is the magnetic flux quantum and ΔI_C is the magnetic field modulation depth $\Delta I_C = I_C^{max} - I_C^{min}$ ¹⁰¹.

The inductance of the loop can be also calculated numerically by solving the Maxwell and London equations for two SQUID geometries^{101,180} (aligned along b or c). Choosing $\lambda_L^b = 280$ nm and $\lambda_L^c = 4.2$ μ m (as the only two fitting parameters in the simulation) the experimental and numerical loop inductances are in very good agreement for both configurations. This leads to a $\lambda_L^b/\lambda_L^c \approx 15$ which allows to determine the expected $J_C(\gamma)$ through Eq. 9.6. It is shown as a dashed line in Fig. 9.2. The expected $J_C(\gamma)$ is in good agreement with the measured behavior.

9.2 RESISTANCE VS. TEMPERATURE OF NANOWIRE ALONG $\gamma = 0^\circ$ AND $\gamma = 90^\circ$

We have characterized our nanostructures along $\gamma = 0^\circ$ and $\gamma = 90^\circ$ by measuring the $R(T)$ of 65 nm wide nanowires (see Fig. 9.4).

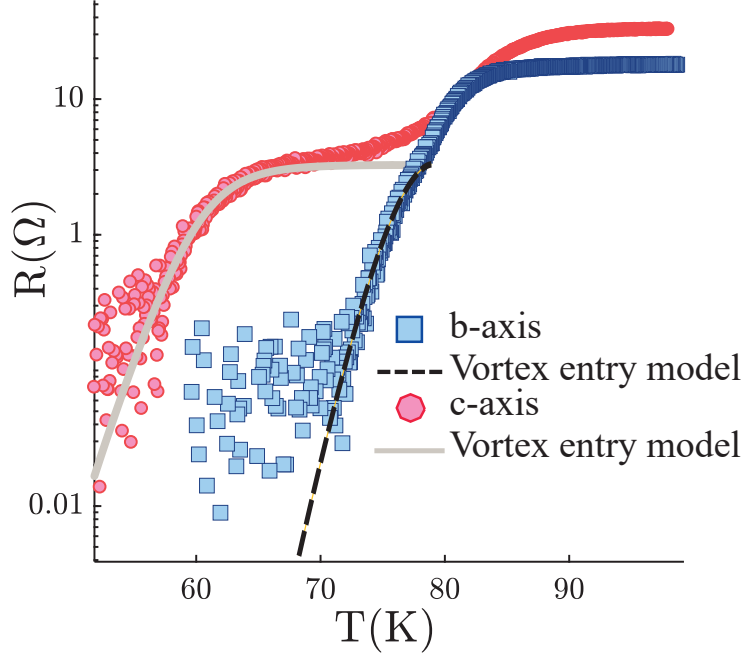


Figure 9.4: Resistance-temperature for a nanowire along b -axis (blue squares) and c -axis (red circles).

The $R(T)$ measurements show two resistance drops: the first one (at a higher temperature) which is sharper, happens when the wide electrodes undergo the superconducting transition. The second one, broader (at a lower temperature) represents the superconducting transition of the nanowires.

In our nanowires, the width is much larger than the superconducting coherence length ($w \gg 4.4\xi(T)$ up to $T \approx T_C$), we can therefore fit the superconducting transition of the nanowires along the b -axis and the c -axis employing the thermally activated vortex-entry (TAVE) model^{79,80} which is discussed in Section. 3.2 and is already used in Ch. 7. For completeness we report here again the expression of $R(T)$:

$$R(T) = R_{\square} \sqrt{2\pi} (1 + \pi) \frac{l\xi}{w^2} \left(\frac{\epsilon_B(T)}{k_B T} \right)^{\frac{3}{2}} \exp \left[-\frac{\epsilon_B(T)}{k_B T} \ln \frac{1.47w}{\pi\xi} \right], \quad (9.7)$$

where R_{\square} is the sheet resistance of the wire, and $\epsilon_0(T) = \Phi_0^2 t / 4\pi\mu_0 \lambda_L^2(T)$ is the characteristic energy giving the magnitude of the potential barrier for the vortex entry. As shown in Fig. 9.5, the Abrikosov vortices acquire an elliptic-like shape¹⁸¹.

We assume that the London penetration depth and the coherence length along b -axis

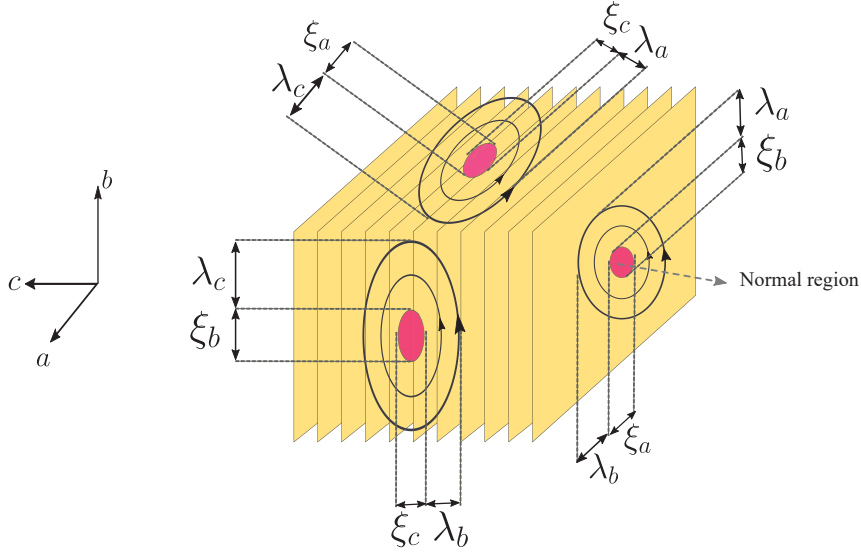


Figure 9.5: Sketch of Abrikosov vortices in an anisotropic superconductor such as YBCO.

have the same temperature dependence and are given by:

$$\lambda_L^2(T) = \lambda_b(0)\lambda_c(0)/(1 - T^2/T_C^2), \quad (9.8a)$$

$$\xi_{ab,c}^2(T) = \xi_{ab,c}^2(0)/(1 - T^2/T_C^2), \quad (9.8b)$$

where $\lambda_b(0)$, $\lambda_c(0)$, $\xi_b(0)$ and $\xi_c(0)$ represent the zero-temperature values.

By considering nanowire dimensions very close to the geometrical ones, we have fitted the broadening of the superconducting transition of both the nanowire along the b -axis, $\gamma = 0^\circ$, and the c -axis, $\gamma = 90^\circ$ (see the solid lines in Fig. 9.4). For $\gamma = 0^\circ$ in the expression 9.7 we have to use ξ_c and $\lambda_L^2 = \lambda_b\lambda_c$ as fitting parameter while for $\gamma = 90^\circ$ we need to use ξ_b and $\lambda_L^2 = \lambda_b \cdot \lambda_c$ to fit the $R(T)$ measurement (see Fig. 9.5). Table 9.1 summarizes the parameters used to fit the $R(T)$ measurements.

The extracted values of $\lambda_b(0)$ and $\lambda_c(0)$ are in line with those determined from the modulation depth of the nanoSQUIDS. We also obtained a value of 2.8 nm for the zero temperature superconducting coherence length along the b -axis which is very close to the one associated to nanostructures patterned using c -axis films^{152,154,158}.

Table 9.1: Summary of the parameters used in the thermally activated vortex entry model to fit the $R(T)$ of the nanowires shown in Fig. 9.4.

Nanowire	t (nm)	l (nm)	w (nm)	T_C (K)	R_\square (Ω)	R_{sh} (Ω)	$\xi_b(0)$ (nm)	$\xi_c(0)$ (nm)	$\lambda_b(0)$ (nm)	$\lambda_c(0)$ (μm)
[0, 1, 0]	45	100	55	80.4	80	8.5	—	0.55	280	4.2
[0, 0, 1]	45	100	45	80.0	250	3.3	2.8	—	280	4.2

9.3 EFFECT OF OZONE TREATMENT ON SUPERCONDUCTING PROPERTIES OF NANOWIRES

To restore the oxygen content close to the optimal doping, we have annealed the sample for 2 hours at 150 °C in a chamber filled with ozone, with a procedure already successfully used for nanowires patterned on *c*-axis YBCO films as discussed in section 7.3.1.

Fig. 9.6(a) shows the IV characteristics of a 65 nm wide wire along the *c*-axis before and after the ozone treatment. As a consequence of the ozonation, the critical currents of the nanowires increases up to a factor 5 while the superconducting transition broadening becomes sharper and the critical temperature T_C significantly increases. (see Fig. 9.6(b)). We also observe that by performing the ozone treatment, one can heal the strongly damaged regions in such a way that a resistive section inside the nanowire turns superconducting (see Fig. 9.6(c)).

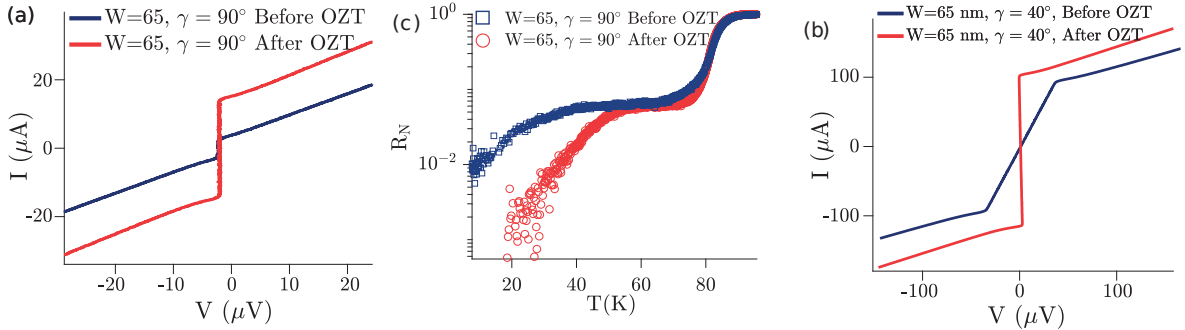


Figure 9.6: The effect on ozone treatment on (a) the current-voltage (b) resistance-temperature characteristics, (c) the nanowire which showed a series resistance in its IVC becomes superconducting after ozonation.

9.4 TEMPERATURE DEPENDENCE OF THE LONDON PENETRATION DEPTH

We can obtain the temperature dependence of the London penetration depth λ_L along the *c*-axis, by extracting the screening inductance factor β_L from the magnetic modulation of the critical current density of the nanoSQUID along the *c*-axis for several temperatures.

Fig. 9.7(a) shows the critical current of the nanoSQUID along the *c*-axis, as a function of an externally applied magnetic field for different temperatures. One can calculate the screening factor of the SQUID as $\beta_L^{\text{exp}} = I_c^{\text{max}}(T)/\Delta I_C(T)$. The screening factor can be expressed as $I_C^{\text{max}}(T)L_{\text{Loop}}^{\text{exp}}(T)/\Phi_0$, where $L_{\text{Loop}}^{\text{exp}}$ is the total inductance of the nanoSQUID loop which in our case is dominated by the kinetic inductance. The total inductance can be evaluated numerically, $L_{\text{loop}}^{\text{num}}$ through solving the Maxwell and London equations describing the Meissner state on our nanoSQUID geometry. One can determine the $\lambda_c^{\text{exp}}(T)$ as a variable to best interpolate $L_{\text{Loop}}^{\text{num}}$ with $L_{\text{Loop}}^{\text{exp}}$. Fig. 9.7(b) (circles) shows the extracted value of $\lambda_c(T)$. The temperature dependence of

the $\lambda_c(T)$ can be described by the Gorter-Casimir two fluid approximation $\lambda_c(T) = \frac{\lambda_c(T=0)}{\sqrt{1-(T/T_C)^p}}$ (Eq. 9.8a) with an arbitrary exponent p to fit the data. As shown in Fig. 9.7(b), there is good agreement between the extracted λ_c^{exp} and theoretical $\lambda_c(T)$, by considering $p = 2.8$. This value is not too far from the value $p = 2$ used to fit the $R(T)$.

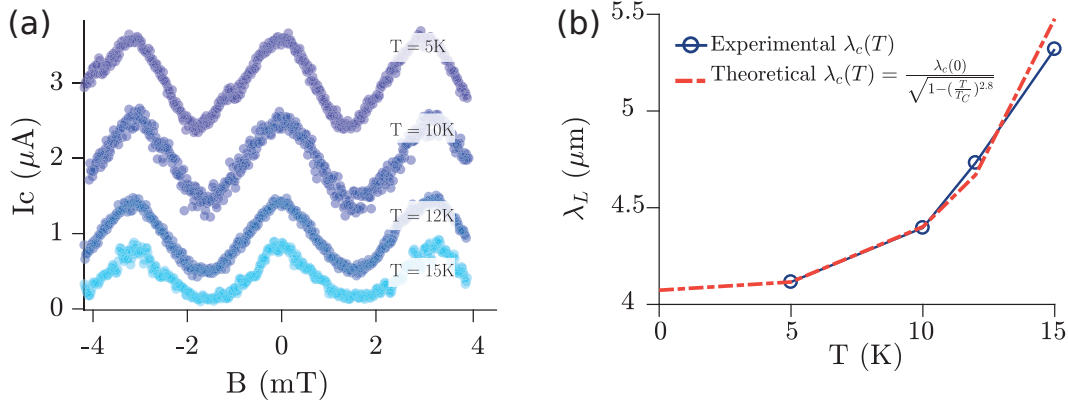


Figure 9.7: (a) Critical current as a function of the applied magnetic field $I_C(B)$ measured at temperatures $T=5\text{ K}, 10\text{ K}, 12\text{ K}, 15\text{ K}$ (b) Comparison between the experimental (circles) and the theoretical (triangles) values of $\lambda_L(T)$ within the Gorter-Casimir model as a function of the temperature considering $\lambda_0 = 4.1\ \mu\text{m}$ and $p = 2.8$.

9.5 HALF INTEGER SHAPIRO-LIKE STEPS IN UNDERDOPED a -AXIS NANOWIRES

To get more insights into the transport along the c -axis, in a regime of strong confinement of the a - b planes, we have studied the phase dynamics of the c -axis nanowires, by applying microwave radiation. As a consequence of the synchronization of the motion of Abrikosov vortices to the frequency of the applied microwave radiation, Shapiro-like steps at $V_n = n \frac{h f_{MW}}{2e}$ appear in the IV characteristics^{96,97}.

In this section, we consider the rf-effect on the c -axis oriented nanowires, as the b -axis oriented nanowires demonstrated the expected integer Shapiro-like steps both before and after ozone treatment. Fig. 9.8(a) shows the logarithmic differential resistance map as a function of the microwave current, $I_{rf} \propto P^{\frac{1}{2}}$, and the bias current at $f_{MW} = 5.4\ \text{GHz}$ for the nanowire before ozone treatment.

Integer and the half integer Shapiro-like steps are observed in the dI/dV - $V(\Phi_0)$ plot (Fig. 9.8(c)). However, after the ozone treatment the amplitude of the half-integer Shapiro-like steps get substantially reduced (Figs. 9.8(b) and 9.8(d)). The reason that after the ozone treatment, the amplitudes of the half-integer Shapiro-like steps drop significantly could be due to the fact that the ozonation leads to the strong modification of doping level of the nanowire.

There are various theoretical works^{182,183} suggesting the coexistence of a $4e$ superfluid

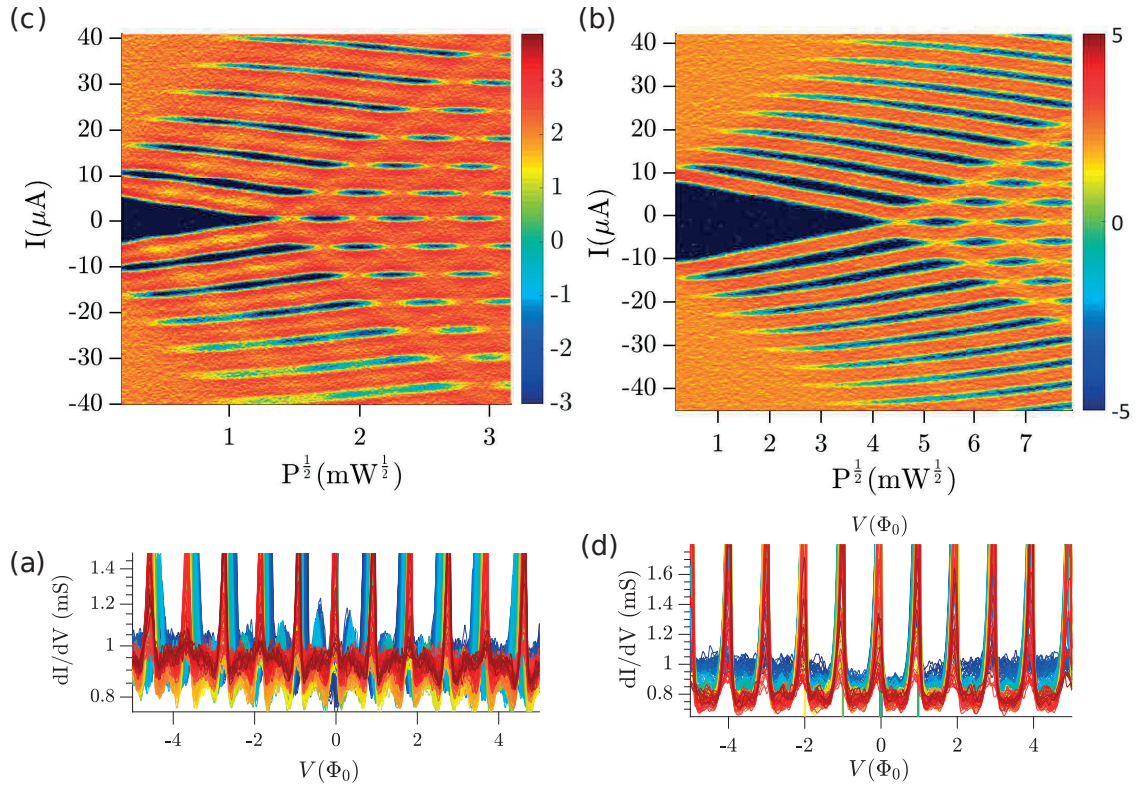


Figure 9.8: Color maps of differential resistance as a function of junction DC bias and radiated microwave field amplitude $P^{1/2}$ at $T = 5$ K for a c -axis orientated nanoSQUID a) before ozone treatment and b) after ozone treatment, c) the conductance plotted as a function of $V(\Phi_0)$ before the ozone treatment, and d) the same measurement after the ozone treatment. The half-integer steps vanished after the sample being oxygenated in the ozone chamber.

and a conventional $2e$ components in underdoped HTS materials. In this case the existence of the $4e$ component would lead to the appearance of half integer Shapiro-like steps. Another possibility for the observation of half-integer Shapiro-like steps in the c -axis nanowires is a reduction of coupling between the a - b planes. In this scenario, a Josephson coupling between the planes could explain the appearance of half-integer Shapiro-like steps¹⁸⁴⁻¹⁸⁶. The underdoped c -axis nanowires can be envisioned as a series of highly transparent Josephson junctions with an unconventional current-phase relation (CPR) with high order harmonics. A finite second harmonic in the CPR would lead to the appearance of half-integer Shapiro-like steps. After ozonation, the oxygen doping level increases and the coupling strength between the CuO_2 planes increases. As a result, the transport is not dominated anymore by the Josephson effect, but by the vortex dynamics. (see Fig. 9.8(d)).

10

Conclusion

In this chapter, we summarize our work and propose possible prospective experiments to proceed and complete our study.

One thing is very clear: if one manages to develop nanogaps employing the superconducting properties of a d-wave superconductor (e.g. YBCO) interfaced with 2-dimensional materials such as graphene, and topological insulators, it is possible to study novel physical phenomena as a result of proximity effect.

However, fabricating such a system due to the nature of high reactivity of the YBCO material turns out to be very challenging. In this work, we studied thoroughly the effect of nanofabrication processing on the superconducting performance of YBCO nanostructures. We confirmed that the encapsulation method is a very promising approach in making hybrid junctions allowing us to protect YBCO from any chemicals which ineluctably affect the YBCO during the fabrication processing. In addition, the YBCO/Au interface showed a very high interface transparency which is imperative for maximizing the superconducting proximity effect inside the interlayer material. To verify this we measured the interface resistance using the transfer line method (TLM) and achieved very low interface resistance varies in the range of $5.10^{-8}\Omega.\text{cm}^{-2}$. This value is among the lowest reported for YBCO/Au junctions.

We furthermore fabricated YBCO-Au-YBCO junctions and successfully showed the proximity effect in these junctions up to $T = 78\text{ K}$. However, in these SNS junctions, we had issues with the purity of the Au film which limited the maximum bridge length to less than 120 nm. Above this value, the Cooper pairs suffer severely from the dephasing due to the magnetic impurities in the Au. We investigated this issue by performing the magnetoresistance of the different Au films we used during the fabrication process (see

Appendix. C).

For these junctions, we used SINI'S model to analyze the $I_C(T)$ measurement and we found that transport is governed by a tiny channel of ~ 10 nm despite the geometrical dimensions of the nanogap which is above 100 nm. This is due to the specifics of nanoprocessing. By reducing the thickness of YBCO films one should be able to get narrower gaps. We demonstrated that we can grow very thin YBCO films down to 3.5 nm. As a future plan, we are going to realize SNS junctions using 10 nm or thinner YBCO films.

A-axis YBCO films have clear advantages to fabricate hybrid junctions. We have grown 50 nm thick *a*-axis oriented $\text{YBa}_2\text{Cu}_3\text{O}_{7-\gamma}$ films on (100) LaSrGaO_4 substrates using $\text{PrBa}_2\text{Cu}_3\text{O}_{7-\gamma}$ as a buffer layer. Furthermore, by patterning YBCO nanowires at a different in-plane angle with respect to the [001] direction of the substrate, we studied the in-plane dependence of the critical current density J_C . The anisotropy of J_C has been elucidated by considering the anisotropy in the coherence length ξ and London penetration depth λ_L .

Possible future work is to study the strength of the induced gap of the *c/a*- axis YBCO in the Au film. This will be done by using ARPES (Angle-resolved photoemission spectroscopy) and neutron scattering measurements. From these last measurements, one can extract the London penetration depth λ and from that, it is possible to get more insight into the induced gap.



Constants-Symbol Definition-Abbreviation

Constants

h	Planck constant	$\simeq 6.63 \times 10^{-34}$ Js
\hbar	Reduced Planck constant	$= h/2\pi \simeq 1.1 \times 10^{-34}$ Js
e	Elementary charge	$\simeq 1.6 \times 10^{-19}$ C
c	Speed of light in vacuum	$\simeq 3 \times 10^8$ m/s
k_B	Boltzmann constant	$\simeq 1.38 \times 10^{-23}$ J/K
$k_F(\text{Au})^{187}$	Fermi wavevector in Au	$\simeq 1.2 \times 10^8$ cm $^{-1}$
$v_F(\text{Au})^{187}$	Fermi velocity in Au	$\simeq 3.8 \times 10^8$ cm/sec
m	Electron mass	$\simeq 9.11 \times 10^{-31}$ Kg
μ_0	Vacuum permeability	$\simeq 4\pi \times 10^{-7}$ H/m
Φ_0	Magnetic flux quantum	$= h/2e \simeq 2.07 \times 10^{-15}$ Tm 2
f_J	Josephson frequency	$= 2eV/h \simeq V \times 483.6$ MHz/ μ V

Symbol Definition

B_C	Critical magnetic field		critical current density
H_C	Thermodynamic critical field	k_B	Boltzmann constant
T_C	Critical temperature	ϵ_B	characteristic energy of a vortex
I_C	Critical current	m^*	Mass of a Cooper pair ($= 2m_e$)
I_r	re-trapping current	m_c	Effective mass along c -axis
J_C	Critical current density	m_{a-b}	Effective mass along ab -axis
J_{dep}	GL depairing current	n_s	Density of Cooper pairs
J_s	Superconducting	e^*	electrical charge

	of a Cooper pair(= 2e)	η	damping coefficient
E	Electric field	τ_J	Josephson constant time
\mathbf{B}	magnetic field	τ_{RC}	RC time constant
λ_L	London penetration depth	\mathcal{T}	SN interface transparency
λ_J	Josephson penetration depth	Z	barrier strength
λ_0	zero temperature value of the London penetration depth	$N_{1,2}$	Density of states
ξ	coherence length	$V(x)$	e-e interaction
ξ_0	zero temperature value of the coherence length	$F(x)$	Condensation amplitude
λ_P	Pearl length	ρ_c	specific resistance of the SN boundary
h	Plank constant	l_e	Mean free path
Φ_0	Flux quantum	$L\varphi$	Phase coherence length
Ψ	wave function	ξ_S	superconducting coherence length
α	GL coefficient	ξ_N	Normal coherence length
β	GL coefficient	D	Diffusion constant
p	Hole concentration	v_F	Fermi velocity
Δ	Superconducting energy gap	E_{Th}	Thouless energy
R_N	Normal resistance	ω_n	Matsubara frequencies
R_{\square}	Surface resistance	t_0	electron time of flight
ω_J	Josephson frequency	T_{sub}	substrate temperature
E_J	Josephson coupling energy	$T_{pre-ann}$	post-annealing temperature
l	junction length	$t_{pre-ann}$	pre-annealing time
w	junction width	f_L	Laser frequency
t	junction thickness	$T_{pre-ann}$	pre-annealing temperature
d_{eff}	effective magnetic thickness	R_{dep}	Deposition rate
P_{rf}	microwave drive power	p_{ann}	Annealing pressure
I_{rf}	microwave drive current	ΔT	transition broadening
ω_{rf}	microwave frequency	ρ	contact resistivity
ω_p	Plasma frequency	ρ_N	Specific normal resistance of a normal conductor
Φ_{ext}	external flux	ρ_S	Specific normal resistance of a superconductor
L	SQUID inductance	ξ_a	coherence length along a
L_g	geometric inductance	ξ_b	coherence length along b
L_k	kinetic inductance	ξ_c	coherence length along c
β_L	SQUID screening inductance	λ_a	London penetration depth along a
β_C	Stewart-McCumber parameter	λ_b	London penetration depth along b
R	resistance	λ_c	London penetration depth along c
C	Capacitance	$R(T)$	resistance-temperature dependence
M	mass of particle		

List of abbreviations

ABS	Andreev Bound State
AC	Alternate Current
AFM	Atomic Force Microscope
BTK	Blonder-Tinkham-Klapwijk
CDW	Charge Density Wave
CPR	Current Phase Relation
DC	Direct Current
DLC	Diamond-like Carbon
EBL	Electron Beam Lithography
GL	Ginzburg-Landau
HTS	High critical Temperature Superconductor
IVC	Current-Voltage Characteristic
JJ	Josephson Junction
LY	Likharev-Yakobson
MBS	Majorana Bound state
PLD	Pulsed Laser Deposition
QHE	Quantum Hall Effect
RCSJ	Resistively and Capacitively Shunted Junction
SEM	Scanning Electron Microscope
SC	Superconductor
ScS	Superconductor-Constriction-Superconductor
SIN	Superconductor-Insulator-Normal
SIS	Superconductor-Insulator-Superconductor
SNS	Superconductor-Normal-Superconductor
SINI'S	Superconductor-Insulator-Normal-Insulator-Superconductor
SQUID	Superconducting QUantum Interference Device
TAVE	Thermally activated vortex entry model
TEM	Transversal Electro-Magnetic
TI	Topological Insulator
XRD	X-Ray Diffraction
YBCO	$\text{YBa}_2\text{Cu}_3\text{O}_{7-\gamma}$

This page intentionally left blank.

B

Mean free path in Au

For the conductivity of metals in the Drude model, we have:

$$\sigma = \frac{e^2 n_e \tau}{m_e} \quad (\text{B.1})$$

From the Matthiessen relation we have (at T=300 K):

$$\frac{1}{l_{300K}} = \frac{1}{l_{e-ph}} + \frac{1}{l_e} \quad (\text{B.2})$$

And from the Drude equation we have:

$$\sigma_{300K} = \frac{n_e e^2 l}{m_e v_F} \quad (\text{B.3})$$

Similarly at T= 4 K we have:

$$l_{4K} = l_e, \quad (\text{B.4})$$

and

$$\sigma_{300K} = \frac{n_e e^2 l}{m_e v_F} \quad (\text{B.5})$$

Dividing Eq. (B.3) and Eq. (B.5) reads:

$$\frac{\sigma_{300K}}{\sigma_{4K}} = \frac{l_{300K}}{l_{4K}} \quad (\text{B.6})$$

Substituting the Eq. (B.2) and the Eq. (B.4) in the Eq.(B.6) gives:

$$\frac{\sigma_{300K}}{\sigma_{4K}} = \frac{(1/l_{e-ph} + 1/l_e)^{-1}}{l_e} = (1 + l_e/l_{e-ph})^{-1} \quad (\text{B.7})$$

Therefore we have:

$$l_e = l_{e-ph} \left(\left(\frac{\sigma_{300K}}{\sigma_{4K}} \right)^{-1} - 1 \right) = l_{e-ph} \left(\frac{\rho_{300K}}{\rho_{4K}} - 1 \right) \quad (\text{B.8})$$

The electron-phonon scattering length l_{e-ph} in Au at $T = 300 \text{ K}$ in Eq. (B.8) is given by:

$$l_{e-ph} = \tau_{e-ph} \times v_F = 3 \times 10^{-14} \times 1.4 \times 10^6 = 42 \text{ nm}. \quad (\text{B.9})$$

The elastic mean free path (at 4k) in Eq.(B.8) becomes:

$$l_e(\text{nm}) = 42 \left(\frac{\rho_{300K}}{\rho_{4K}} - 1 \right) \quad (\text{B.10})$$

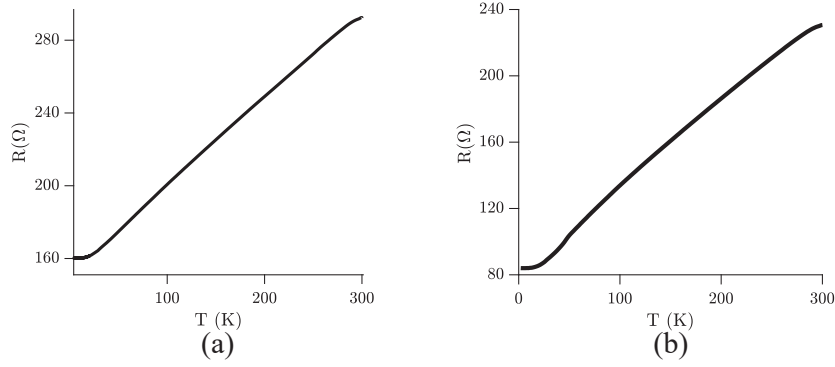


Figure B.1: Resistance-Temperature dependence of the (a) sputtered, (b) evaporated Au films.

We deposited sputtered and evaporated Au films, and fabricated a long Au wire. Fig. B.1 shows the resistance-temperature of sputtered and evaporated Au wires. Using Eq. B.10, one finds the mean free path of 35 nm and 71 nm for sputtered and evaporated Au films, respectively.

C

Characterization of Au quality

One of the main limiting factors in realizing SNS junctions is having a short coherence length ξ_N in the Au interlayer. Therefore, it is important to be sure that the Au normal metal is as pure as possible. To address this issue, we performed magneto-resistance $R(B)$ as well as resistance-temperature measurements on the Au films of different deposition systems. Specifically, we deposited 50 nm thick Au films from the sputtering and evaporated machine. then we patterned them into the wires and performed the measurements. Fig. C.1 (a) shows the $R(B)$ measurements of the sputtered Au at different temperature. The measurements suggest that there are magnetic impurities inside the Au thin film which can be described by the Kondo physics. Fig. C.1 (b) shows the $R(B)$ measurement of the evaporated Au which does not show any sign of magnetic impurities at high fields.

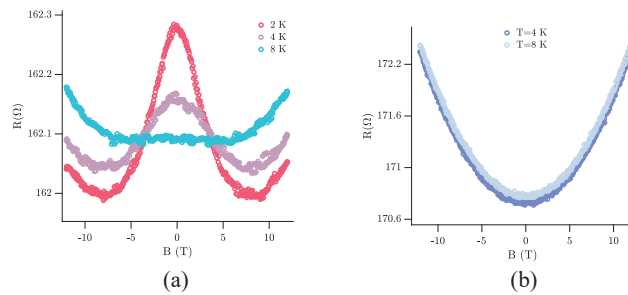


Figure C.1: Magneto resistance measurement of (a) sputtered and (b) evaporated Au film. The magnetic impurities in the sputtered Au layer can be described by the Kondo effect.

This page intentionally left blank.

D

Measurement setup

D.1 280 mK HELIUM FRIDGE

All of the fabricated devices are characterized by cooling down the sample inside the Oxford Heliox VL ^3He cryogenic system. The schematic of the system is shown in Fig. D.1. The fridge works based on the condensation of ^3He . This is possible by releasing the ^3He from the heated inbuilt charcoal absorber while the 1K pot is running by pumping the ^4LHe through the pick-up tube. The liquid ^3He then is collected inside the ^3He pot where the sample is situated. Finally, by removing the heat from the inbuilt charcoal, the vapor pressure reduces on top of the condensed ^3LHe and the temperature of the ^3LHe pot goes down to 280 mK.

D.2 ELECTRICAL MEASUREMENT

All samples are characterized by measuring the current-voltage characteristics (IVC) curves of the devices, which are current biased. The biasing circuit consists of a voltage source connected in series with the bias resistor, R_{bias} . To measure the device's current the voltage drop across the sampling resistor, R_s , which is in series with the device is obtained. The device's voltage is determined by measuring the voltage drop across the device. The measured current and voltage signals are amplified through the SRS560 low noise differential amplifiers and then are connected to the DAQ system for further processing. The schematic of the device biasing and measuring system is shown in Fig. D.2.

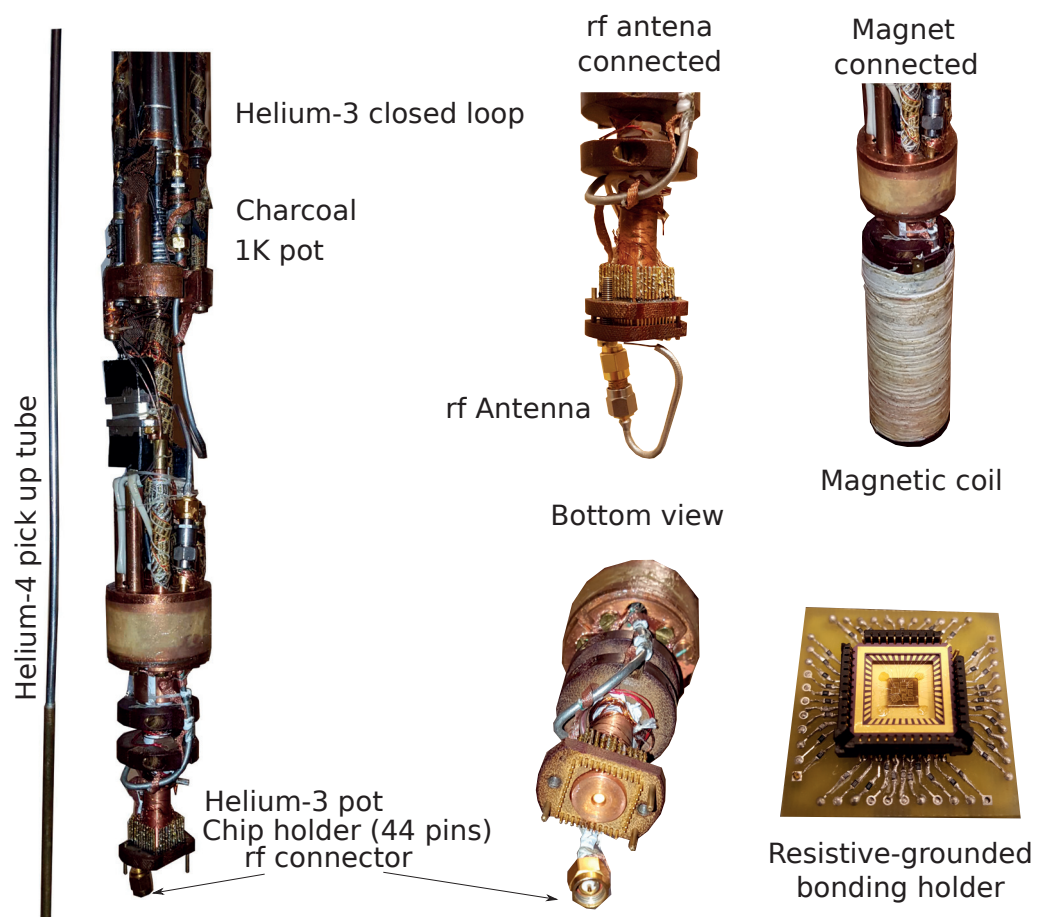


Figure D.1: Sketch of the inset of Heliox-VL ^3He refrigerator: The insert has a sliding cone seal with ^3He sorption pump works with inbuilt heater. The 1 K pot provide necessary cooling temperature requires to condense ^3He gas. The liquid ^3He collected in ^3He pot.

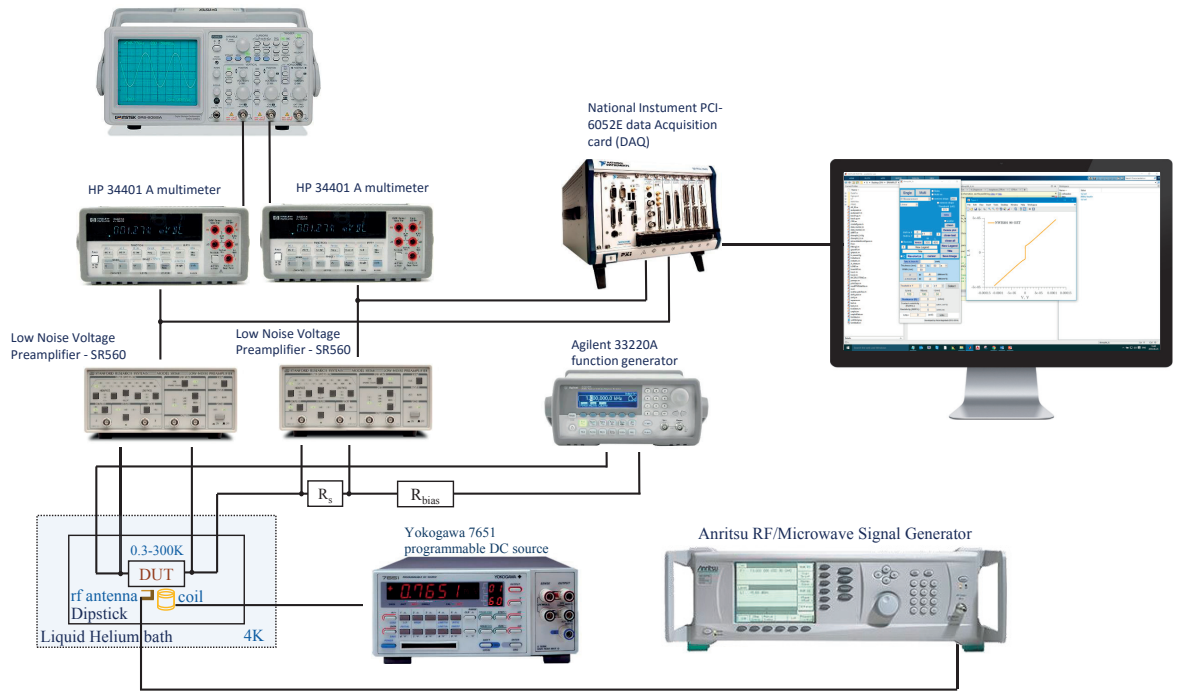


Figure D.2: Electrical measurement setup used for DC characterizing of our devices.

For the magnetic field measurements, the fridge is equipped with the NbTi coil for the application of a magnetic field around 20 mT. The coil is biased with the Yokogawa 7651 programmable DC source.

In order to shine radio frequency, the antenna is placed right above the sample and is connected to the Anritsu microwave generator.

Following electronics were involved during the measurements:

1. HP 34401-A amplifier
2. Stanford research low noise voltage pre-amplifier
3. Agilent 33220A, function generator
4. Yokogawa 7651, programmable DC source
5. National instruments PCI 6052E data acquisition card
6. Anritsu synthesized CW & sweep/signal generators

D.3 DRAWPLOT PLOTTING SOFTWARE

In order to plot and process the measurements, I developed a plotting software, named Drawplot, based on MATLAB. This software enables us to plot different kind of measurements as

listed below:

- IV measurements
- Resistance-Temperature measurements
- Conductance dI/dV and Resistance dV/dI
- rf measurements
- Magnetic field measurements
- Critical Current-Temperature measurement.

E

Nanofabrication processes

In this appendix, we look into the nanofabrication recipes developed and applied for making different junction discussed in this thesis.

Note that the parameters given in this section are specified for the fabrication systems of the Nanofabrication Laboratory at the department of Microtechnology and Nanoscience, Chalmers.

E.1 FABRICATION RECIPE FOR YBCO NANOWIRES/NANOGAP

E.1.1 Substrate cleaning procedure

1165 remover *or* Acetone- heated at 65 ° (5 min)

surface cleaning with a cotton tip

IPA bath

Ultrasonic bath- Maximum power (5 – 10 min)

Rinse in IPA bath and blow dry with N₂

Check under microscope and repeat the cleaning procedure if it is necessary.

E.1.2 Growth of c-axis YBCO films on the MgO substrate (DCA UHV #1142)

After cleaning the MgO substrate, it is loaded inside the DCA ultra high vacuum system. The Deposition conditions are as following.

Deposition temperature	760 °C
Deposition pressure	0.7 mbar
Target-substrate distance	54 mm
Annealing pressure	900 mbar
Cooling rate	5 °C/min

E.1.3 Deposition of in-situ Au film (DCA metal sputter #1144)

A thin layer of Au film is insitu sputtered and acts mainly as the protection layer for YBCO film. The deposition parameters are as following:

Deposition rate	9 Å/sec
Pre-sputtering time	2 min
Au DC-power	50 W
Ar pressure	5 μbar
Ar flow	60 sccm
Final thickness	20 nm

E.1.4 Deposition of diamond-like mask (PLD Carbon System #11413)

We used diamond-like carbon as a hard etching mask. The deposition parameters are as following:

Base pressure	1×10^{-7} mbar
Deposition pressure	3×10^{-4} mbar
Target-substrate distance	50 mm
Laser Energy	90 – 105 mJ
Laser frequency	10 Hz
Deposition time	5 min

E.1.5 preparation of e-beam resist layer(s)

- The double layer resists system (ZEP:copolymer) has the benefit that the selectivity of the developers for top and bottom layer is almost perfect, so the developing time can be tuned based on our needs. The necessary exposure dose and obtainable resolution are equivalent or better

than that of PMMA/Copolymer.

The procedure is as following:

Clean the surface with 5 sec oxygen ashing. Rinse in IPA and blow dry in N₂

Double layer resists

- Copolymer EL2* & ZEP520A diluted 1 : 2 in Anisole
- Copolymer EL4* & ZEP520A diluted 1 : 4 in Anisole
- Copolymer EL6* & ZEP520A diluted 1 : 4 in Anisole

* The bottom Copolymer layer thickness should be > 20% thicker than the thickness of the deposited material to be lifted off.

Using single layer resist system allows you to avoid baking the resist twice and resist baking temperature for the ZEP can be reduce down to 90 °C without compromise.

Single layer resist

- ZEP520A diluted 1 : 4 in Anisole
 - ZEP520A diluted 1 : 2 in Anisole
- Spin both resist layers at 5500 – 6000 rpm for 1 min
Resist copolymer-EL baked at 110 °C for 5 min
ZEP resist baked at 90 °C for 2 min

E.1.6 Electron beam lithography (JEOL JBX-9300FS #217)

Process steps in making the ebeam-lithography are as following:

- 1- Mask preparation with AutoCAD or layout editor
- 2- Proximity correction with PROXECCO¹⁸⁸ or BEAMER
- 3- Writing small structures: $V_{acc} = 100$ kV, aperture 5, $I = 1$ nA, base dose= $160 \mu\text{C}/\text{cm}^2$
- 4- Writing big structures: $V_{acc} = 100$ kV, aperture 7, $I = 10$ nA, base dose= $250 \mu\text{C}/\text{cm}^2$
- 5- Writing huge structures: $V_{acc} = 100$ kV, aperture 8, $I = 35$ nA, base dose= $300 \mu\text{C}/\text{cm}^2$

E.1.7 Resist Development

The resist development is one of the crucial steps in achieving very small and dense structures.

E.1.8 Oxygen ashing (Plasma Therm BatchTop #418 – 419)

- Power 50 W, 250 mTorr Oxygen plasma, for 3 – 5 sec

Develop top resist (ZEP)	
o-xylene	30 sec*
n-amyl acetate	30 sec*
Hexyl acetate (highest resolution)	30 sec*
	Dip in IPA and below dry with N ₂

Develop bottom resist (copolymer)	
H ₂ O:IPA 90 : 10%	80 sec*
H ₂ O:IPA 75 : 25%	60 sec*
MIBK:IPA 1 : 1	60 sec*
MIBK:IPA 1 : 4	70 sec*
	Dip in IPA and below dry with N ₂

*The mentioned development time is the general one, and it will be fine tuned for different patterns

E.1.9 Cr deposition (e-beam evaporator Lesker-1 #451)

- Chamber pressure below 10⁻⁷ mbar
- Masking layer (Cr) 120, Å/sec

E.1.10 Lift-off process

During the lift-off process, the resist under the film is removed with solvent (remover), taking the film with it, and leaving only the film which was deposited directly on the substrate.

Lift-off in 1165 remover*	60 – 75 °C** for t > 15 min
Ultrasonic agitation	low powers for 20 – 30 sec
Rinse in IPA and below dry with N ₂	

*Acetone is not recommended as it does not remove ZEP layer.

** The flash point of the 1165 remover is around 85 °C.

E.1.11 Carbon mask stripping with oxygen plasma

Un-protected carbon layer (by the Cr-layer) can be removed through O₂ plasma etching in the Batchtop system. - Power 50 W*, 100 mTorr Oxygen plasma, for 30 – 35 min *the power can be reduced down to 10 W for specific applications.

E.1.12 Ar-ion milling (CAIBE Oxford Ionfab #417)*

The YBCO and Au layer which are not covered by the C mask, can be etched softly and gently in Ar ion milling system.

Beam voltage	300 V
Acc voltage	300 V
Beam current	5 – 5.3 mA
Stage tilt	5 – 7°
Base pressure	1×10^{-7} mbar
Process pressure	$1.5 - 2.3 \times 10^{-4}$ mbar
Ar flow	4 sccm
Neutralizer	OFF

* in some applications, we used the other Ar ion milling system: CAIBE Oxford Ionfab 300 Plus (416)

E.2 FABRICATION RECIPE FOR ENCAPSULATING NANOWIRES/NANOGAP

In this section, we look into the fabrication steps required in encapsulating YBCO nanowire/nanogap with Pt/Au layer avoiding any chemicals touching YBCO structures.

E.2.1 Sputter deposition of Pt/Au bilayer

Deposition parameters for the Pt layer:

Sputter deposition of Pt layer with the NORDIKO 2000 (# 401)

Base pressure	$< 1.1 \times 10^{-6}$ mbar
Ar flow	50 sccm
rf cleaning	50 W (1 min)
Ar pressure	5 mTorr
deposition time	50 sec

Deposition parameters for the Au layer:

Sputter deposition of Au layer with the FHR MS150 (# 400)

Base pressure	$< 5 \times 10^{-7}$ mbar
Ar flow	40 sccm
rf cleaning	50 W (1 min)
Ar pressure	5×10^{-3} mbar
deposition time	50 sec

The rest of fabrication procedure is summarized as below:

DLC carbon deposition	70 nm
Spin ZEP 1 : 2 Anisole	6000 rpm
bake on hotplate	90 °C
almost perfect sample alignment	
Expose JEOL JBX-9300FS	$V_{acc} = 100$ kV, $I = 1$ nA and 10 nA
Develop in Hexyl acetate	45 – 60 sec
Oxygen ashing	3 – 5 sec
Metalization with Cr layer	10 – 20 nm
Carbon stripping	50 W for 30 – 35 min
Ar ion milling	$V = 100$ V, $I = 5$ mA, for 120 min
Carbon stripping	50 W for 30 – 35 min

E.3 FABRICATION RECIPE FOR DEFINING THE NORMAL LAYER IN SNS JUNCTIONS

This section is to finalize SNS junctions. The fabrication procedure is as following:

Oxygen Ashing	50 W, 20 sec
Rinse in IPA and dry with N ₂	
Spin ZEP	x 2 5000 rpm
Bake on hotplate	90 °C for 2 min
Spin anti-charging layer, Espacer	no backing
Expose JEOL JBX-9300FS	$V_{acc} = 100$ kV, $I = 1$ nA and 10 nA
Develop in Hexyl acetate	5 min
Rinse in IPA and blow dry in N ₂	10 sec
Oxygen ashing	3 – 5 sec
Metalization (Ti/Au) layer	
Evaporate Ti layer,	Lesker \#1 , 5 nm
Evaporate Au layer,	Lesker \#1 , 70 nm
Lift-off in 1165 remover	heated at 65 – 75 °C, for at least 1 hour

Acknowledgments

My Ph.D. journey is coming to an end and looking back, I realize how far I have come. I was by no means alone and many amazing individuals indeed backed me up during this chapter of my life.

First and foremost, I would like to sincerely thank my supervisor, Floriana Lombardi, for her guidance and for sharing her broad knowledge and vast experience in the field. Her never-ending enthusiasm in uncovering new phenomena through carrying out challenging experiments is simply unique. Likewise, I am very grateful to my co-supervisor, Thilo Bauch, for his continuous support, sharing his immense measurement skills, and his insightful contribution to this work.

During the last five years, I have had the pleasure of working with terrific colleagues. I would like to give my special thanks to David Gustafsson, Domenico Montemurro, Edoardo Trabaldo, Eric Andersson, Evgeny Stepantsov, Gunta Kunakova, Luca Galletti, Marco Arzeo, Maria Ekström, Matteo Salvato, Riccardo Arpaia, Shahid Nawaz, Simon Abbay, Sophie Charpentier, and Zenas Van Veldhoven. You are all incredible and have made this journey even more special for me.

The majority of this work was based on heavy nanofabrication processing, in which I greatly admire the enormous technical support I received from the wonderful staff of the Nanofabrication laboratory. I am especially grateful to Bengt Nilsson, Henrik Frederiksen, Göran Alestig, Johan Karl Andersson, Kaija Matikainen, Mahdad Sadeghi, Marcus Rommel, Mats Hagberg, Petra Johansson, and Ulf Södervall. I indeed received generous guidance from Alexei Kalaboukhov during these years; I am indebted to you.

My gratitude is extended to Lars Jönsson and Staffan Erland Pehrson for their great technical support, to Henric Fjellstedt, and Jan Andersson for their computer support and to Jan Nils-Olof Jacobsson for always providing LHe for our experiments.

I am very proud of the theory developed in this work. Besides the priceless assistance I received from my supervisors, I would like to express my sincerest thanks and appreciation to Golubev Dmitry. Tomas Löfwander and Daniel Persson are acknowledged for long discussions in the theory of electrical transport of my junctions.

I would like to recognize Marie Fredriksson, Susannah Carlsson, Debora Perlheden, Maria Tremblay and Michael Nystås for their fantastic administrative support.

I have to especially thank David Niepce, Fatemah Solouki, Domenico Montemurro and Marco Arzeo for proofreading this thesis.

I am appreciative to all my esteemed colleagues and friends at MC2: André Dankert, Angelo di Marco, Arsalan Pourkabirian, Astghik Adamyan, Avgust Yurgens, Bahram Ganjipour, Ben Schneider, Dag Winkler, David Adolph, David Niepce, Dmitrii Khokhriakov, Ehsan Hashemi, Grigory Skoblin, Hans He, Ida-Maria Svensson, Jonas Bylander, Majid Samani, Minshu Xie, Niclas Lindvall, Omid Habibpour, Philip Krantz, Saroj Prasad Dash, Sebastian de Graaf, Sergey Kubatkin, Sobhan Sepehri, Sumedh Mahashabde, Thomas Aref, Thomas Yager, Tobias Wenger, Tord Claeson, and all the people of QDP laboratory.

Last but not least, I would like to thank my family: my dear parents, my twin brother, Mehdi, and my sister, Parisa, for believing in me from day one. Finally, and most importantly, I would like to thank my wonderful wife, Saide, for her patience and endless encouragement. You mean everything to me and I am very grateful to have you in my life.

References

- [1] Q. J. Sun, H. S. Wang, H. M. Wang, L. W. Deng, Z. W. Hu, B. Gao, Q. Li, and X. M. Xie. Electronic transport transition at graphene/YBa₂Cu₃O_{7- γ} junction. *Applied Physics Letters*, 104(10):102602, 2014.
- [2] D. Perconte, F. Cuellar, M.-B. Martin, B. Dlubak, M. Piquemal-Banci, R. Bernard, J. Trastoy, C. Moreau-Luchaire, P. Seneor, J. Villegas, P. Kidambi, J. Robertson, and S. Hofmann. Experimental study of electrical conduction across high-Tc superconductor-graphene interfaces. In *APS Meeting Abstracts*, 2016.
- [3] Domenico Montemurro, Davide Massarotti, Procolo Lucignano, Stefano Roddaro, Daniela Stornaiuolo, Daniele Ercolani, Lucia Sorba, Arturo Tagliacozzo, Fabio Beltram, and Francesco Tafuri. Towards a hybrid high critical temperature superconductor junction with a semiconducting inas nanowire barrier. *Journal of Superconductivity and Novel Magnetism*, 28(12):3429–3437, 2015.
- [4] Francesco Tafuri, Davide Massarotti, Luca Galletti, Daniela Stornaiuolo, Domenico Montemurro, Luigi Longobardi, Procolo Lucignano, Giacomo Rotoli, Giovanni Piero Pepe, Arturo Tagliacozzo, and Floriana Lombardi. Recent achievements on the physics of high-tc superconductor josephson junctions: Background, perspectives and inspiration. *Journal of Superconductivity and Novel Magnetism*, 26(1):21–41, 2013.
- [5] A Yu Kitaev. Unpaired majorana fermions in quantum wires. *Physics-Uspekhi*, 44(10S):131, 2001.
- [6] V. Mourik, K. Zuo, S. M. Frolov, S. R. Plissard, E. P. A. M. Bakkers, and L. P. Kouwenhoven. Signatures of majorana fermions in hybrid superconductor-semiconductor nanowire devices. 336(6084):1003–1007, 2012.
- [7] Anindya Das, Yuval Ronen, Yonatan Most, Yuval Oreg, Moty Heiblum, and Hadas Shtrikman. Zero-bias peaks and splitting in an al-inas nanowire topological superconductor as a signature of majorana fermions. *Nat Phys*, 8(12):887–895, Dec 2012.
- [8] Sean Hart, Hechen Ren, Timo Wagner, Philipp Leubner, Mathias Muhlbauer, Christoph Brune, Hartmut Buhmann, Laurens W. Molenkamp, and Amir Yacoby. Induced superconductivity in the quantum spin hall edge. *Nat Phys*, 10(9):638–643, Sep 2014. Letter.
- [9] Jason Alicea, Yuval Oreg, Gil Refael, Felix von Oppen, and Matthew P. A. Fisher. Non-abelian statistics and topological quantum information processing in 1d wire networks. *Nat Phys*, 7(5):412–417, May 2011.
- [10] Chetan Nayak, Steven H. Simon, Ady Stern, Michael Freedman, and Sankar Das Sarma. Non-abelian anyons and topological quantum computation. *Rev. Mod. Phys.*, 80:1083–1159, Sep 2008.

- [11] D. A. Ivanov. Non-abelian statistics of half-quantum vortices in p -wave superconductors. *Phys. Rev. Lett.*, 86:268–271, Jan 2001.
- [12] Masatoshi Sato, Yoshiro Takahashi, and Satoshi Fujimoto. Non-abelian topological order in s -wave superfluids of ultracold fermionic atoms. *Phys. Rev. Lett.*, 103:020401, Jul 2009.
- [13] Peter Rickhaus, Markus Weiss, Laurent Marot, and Christian Schönenberger. Quantum hall effect in graphene with superconducting electrodes. *Nano Letters*, 12(4):1942–1945, 2012.
- [14] M. Ma and A. Yu. Zyuzin. Josephson effect in the quantum hall regime. *EPL (Europhysics Letters)*, 21(9):941.
- [15] V. Mourik, K. Zuo, S. M. Frolov, S. R. Plissard, E. P. A. M. Bakkers, and L. P. Kouwenhoven. Signatures of majorana fermions in hybrid superconductor-semiconductor nanowire devices. 336(6084):1003–1007, 2012.
- [16] A. Kastalsky, A. W. Kleinsasser, L. H. Greene, R. Bhat, F. P. Milliken, and J. P. Harbison. Observation of pair currents in superconductor-semiconductor contacts. *Phys. Rev. Lett.*, 67:3026–3029, Nov 1991.
- [17] B. J. van Wees, P. de Vries, P. Magnée, and T. M. Klapwijk. Excess conductance of superconductor-semiconductor interfaces due to phase conjugation between electrons and holes. *Phys. Rev. Lett.*, 69:510–513, Jul 1992.
- [18] R. P. Robertazzi, A. W. Kleinsasser, R. B. Laibowitz, R. H. Koch, and K. G. Stawiasz. *In situ* Ag/ YBa₂Cu₃O_{7- γ} contacts for superconductor normal-metal superconductor devices. *Phys. Rev. B*, 46:8456–8471, Oct 1992.
- [19] C.-H. Chen, I. Jin, S. P. Pai, Z. W. Dong, C. J. Lobb, T. Venkatesan, K. Edinger, J. Orloff, and J. Melngailis. Fabrication of high-temperature superconducting josephson junctions on substrates patterned by focused ion beam. *Applied Physics Letters*, 73(12):1730–1732, 1998.
- [20] Planar sns josephson junctions using fib processing of c -oriented ybco thin films. *Physica C: Superconductivity*, 341:1587 – 1588, 2000.
- [21] Manabu Fujimoto, Kunihiro Hayashi, Katsumi Suzuki, and Youichi Enomoto. Characteristics of ybco josephson junction prepared by a focused ion beam technique. *Japanese Journal of Applied Physics*, 35(1R):90.
- [22] Meissner. W. and R. Ochsenfeld. Ein neuer effekt bei eintritt der supraleitfähigkeit. *Naturwissenschaften*, 21:787, 1933.
- [23] A. P. Drozdov, M. I. Eremets, I. A. Troyan, V. Ksenofontov, and S. I. Shylin. Conventional superconductivity at 203 kelvin at high pressures in the sulfur hydride system. *Nature*, 525(7567):73–76, Sep 2015. ISSN 0028-0836. Letter.
- [24] C. W. Chu, L. Gao, F. Chen, Z. J. Huang, R. L. Meng, and Y. Y. Xue. Superconductivity above 150 k in HgBa₂Ca₂Cu₃O_{8+ δ} at high pressures. *Nature*, 365(6444):323–325, Sep 1993.
- [25] S. N. Putilin, E. V. Antipov, O. Chmaissem, and M. Marezio. Superconductivity at 94 k in HgBa₂Cu_{0.4+ δ} . *Nature*, 362(6417):226–228, Mar 1993.

- [26] S. H. Yun and J. Z. Wu. Superconductivity above 130 k in high-quality mercury-based cuprate thin films. *Applied Physics Letters*, 68(6), 1996.
- [27] A. Schilling, M. Cantoni, J. D. Guo, and H. R. Ott. Superconductivity above 130 k in the hg-ba-ca-cu-o system. *Nature*, 363(6424):56–58, May 1993.
- [28] J. G. Bednorz and K. A. Müller. Possible high t_c superconductivity in the $Ba-La-Cu-O$ system. *Zeitschrift für Physik B Condensed Matter*, 64(2):189–193, 1986.
- [29] Hiramatsu Hidenori Kamihara, Yoichi, Masahiro Hirano, Ryuto Kawamura, Hiroshi Yanagi, Toshio Kamiya, and Hideo Hosono. Iron-based layered superconductor: laofep. *Journal of the American Chemical Society*, 128(31):10012–10013, 2006.
- [30] Johnpierre Paglione and Richard L. Greene. High-temperature superconductivity in iron-based materials. *Nat Phys*, 6(9):645–658, Sep 2010.
- [31] Ruth H. Zadik, Yasuhiro Takabayashi, Gyöngyi Klupp, Ross H. Colman, Alexey Y. Ganin, Anton Potočnik, Peter Jeglič, Denis Arčon, Péter Matus, Katalin Kamarás, Yuichi Kasahara, Yoshihiro Iwasa, Andrew N. Fitch, Yasuo Ohishi, Gaston Garbarino, Kenichi Kato, Matthew J. Rosseinsky, and Kosmas Prassides. Optimized unconventional superconductivity in a molecular jahn-teller metal. 1(3), 2015.
- [32] N. J. Curro, T. Caldwell, E. D. Bauer, L. A. Morales, M. J. Graf, Y. Bang, A. V. Balatsky, J. D. Thompson, and J. L. Sarrao. Unconventional superconductivity in pucoga5. *Nature*, 434(7033):622–625, Mar 2005.
- [33] A. P. Drozdov, M. I. Erements, I. A. Troyan, V. Ksenofontov, and S. I. Shylin. Conventional superconductivity at 203 kelvin at high pressures in the sulfur hydride system. *Nature*, 525(7567):73–76, Sep 2015. Letter.
- [34] Jian-Feng Ge, Zhi-Long Liu, Canhua Liu, Chun-Lei Gao, Dong Qian, Qi-Kun Xue, Ying Liu, and Jin-Feng Jia. Superconductivity above 100 k in single-layer fese films on doped srTiO_3 . *Nat Mater*, 14(3):285–289, Mar 2015. Letter.
- [35] F. London and H. London. The electromagnetic equations of the supraconductor. 149 (866):71–88, 1935.
- [36] Michael Tinkham. *Introduction to Superconductivity: Second Edition (Dover Books on Physics) (Vol i)*. Dover Publications, second edition edition, June . ISBN 0486435032.
- [37] H. Fröhlich. Theory of the superconducting state. i. the ground state at the absolute zero of temperature. *Phys. Rev.*, 79:845–856, Sep 1950.
- [38] J E Hirsch. Did herbert fröhlich predict or postdict the isotope effect in superconductors. *Physica Scripta*, 84(4):045705.
- [39] Emanuel Maxwell. Isotope effect in the superconductivity of mercury. *Phys. Rev.*, 78: 477–477, May 1950.
- [40] C. A. Reynolds, B. Serin, W. H. Wright, and L. B. Nesbitt. Superconductivity of isotopes of mercury. *Phys. Rev.*, 78:487–487, May 1950.
- [41] J. Bardeen, L. N. Cooper, and J. R. Schrieffer. Theory of superconductivity. *Phys. Rev.*, 108:1175–1204, Dec 1957.

- [42] M. A. Subramanin, C. C. Toradi, J. C. Calabrese, J. Gopalakrishnan, K. J. Morrissey, T. R. Askew, R. B. Flippin, U. Chowdhry, and A. W. Sleight. A new high-temperature superconductor: $\text{Bi}_2\text{Sr}_{3-x}\text{Ca}_x\text{Cu}_2\text{O}_{8+y}$. 239(4843):1015–1017, 1988.
- [43] Superconductivity in tlbacuo system. *Solid State Communications*, 65(11):1329 – 1331, 1988.
- [44] James N. Eckstein. Oxide interfaces: Watch out for the lack of oxygen. *Nat Mater*, 6(7): 473–474, Jul 2007.
- [45] Yoshinori Tokura and Takahisa Arima. New classification method for layered copper oxide compounds and its application to design of new high t c superconductors. *Japanese Journal of Applied Physics*, 29(11R):2388.
- [46] R.J. Cava, A.W. Hewat, E.A. Hewat, B. Batlogg, M. Marezio, K.M. Rabe, J.J. Krajewski, W.F. Peck, and L.W. Rupp. Structural anomalies, oxygen ordering and superconductivity in oxygen deficient $\text{YBa}_2\text{Cu}_3\text{O}_{7-\gamma}$. *Physica C: Superconductivity*, 165(5):419 – 433, 1990.
- [47] J. M. Tranquada, A. H. Moudden, A. I. Goldman, P. Zolliker, D. E. Cox, G. Shirane, S. K. Sinha, D. Vaknin, D. C. Johnston, M. S. Alvarez, A. J. Jacobson, J. T. Lewandowski, and J. M. Newsam. Antiferromagnetism in $\text{YBa}_2\text{Cu}_3\text{O}_{6+\gamma}$. *Phys. Rev. B*, 38:2477–2485, Aug 1988.
- [48] H. Ding, T. Yokoya, J. C. Campuzano, T. Takahashi, M. Randeria, M. R. Norman, T. Mochiku, K. Kadowaki, and J. Giapintzakis. Spectroscopic evidence for a pseudogap in the normal state of underdoped high- T_c superconductors. *Nature*, 382(6586):51–54, Jul 1996.
- [49] Ch. Renner, B. Revaz, J.-Y. Genoud, K. Kadowaki, and Ø. Fischer. Pseudogap precursor of the superconducting gap in under- and overdoped $\text{Bi}_2\text{Sr}_2\text{CaCu}_2\text{O}_{8+\delta}$. *Phys. Rev. Lett.*, 80:149–152, Jan 1998.
- [50] P. Monthoux, D. Pines, and G. G. Lonzarich. Superconductivity without phonons. *Nature*, 450(7173):1177–1183, Dec 2007.
- [51] John M. Tranquada. Spins, stripes, and superconductivity in hole-doped cuprates. *AIP Conference Proceedings*, 1550(1), 2013.
- [52] Sudip Chakravarty, R. B. Laughlin, Dirk K. Morr, and Chetan Nayak. Hidden order in the cuprates. *Phys. Rev. B*, 63:094503, Jan 2001.
- [53] R. B. Laughlin. Hartree-fock computation of the high- T_c cuprate phase diagram. *Phys. Rev. B*, 89:035134, Jan 2014.
- [54] B. Keimer, S. A. Kivelson, M. R. Norman, S. Uchida, and J. Zaanen. From quantum matter to high-temperature superconductivity in copper oxides. *Nature*, 518(7538):179–186, Feb 2015. Review.
- [55] Yi Zhang, Akash V. Maharaj, and Steven Kivelson. Disruption of quantum oscillations by an incommensurate charge density wave. *Phys. Rev. B*, 91:085105, Feb 2015.
- [56] Patrick Lee. Amperean pairing and the pseudogap phase of cuprate superconductors. *Phys. Rev. X*, 4:031017, Jul 2014.

- [57] C. M. Varma. Theory of the pseudogap state of the cuprates. *Phys. Rev. B*, 73:155113, Apr 2006.
- [58] D. N. Zheng, A. M. Campbell, J. D. Johnson, J. R. Cooper, F. J. Blunt, A. Porch, and P. A. Freeman. Magnetic susceptibilities, critical fields, and critical currents of co- and zn-doped $\text{YBa}_2\text{Cu}_3\text{O}_{7-\gamma}$. *Phys. Rev. B*, 49:1417–1426, Jan 1994.
- [59] J.R. Waldram. *Superconductivity of Metals and Cuprates*. ISBN 9780852743379.
- [60] S. T. Johnson, E. M. Forgan, S. H. Lloyd, C. M. Aegerter, S. L. Lee, R. Cubitt, P. G. Kealey, C. Ager, S. Tajima, A. Rykov, and D. McK. Paul. Flux-line lattice structures in untwinned $\text{YBa}_2\text{Cu}_3\text{O}_{7-\gamma}$. *Phys. Rev. Lett.*, 82:2792–2795, Mar 1999.
- [61] C. C. Tsuei and J. R. Kirtley. Pairing symmetry in cuprate superconductors. *Rev. Mod. Phys.*, 72:969–1016, Oct 2000.
- [62] D. A. Wollman, D. J. Van Harlingen, W. C. Lee, D. M. Ginsberg, and A. J. Leggett. Experimental determination of the superconducting pairing state in ybco from the phase coherence of *YBCO-Pb* dc squids. *Phys. Rev. Lett.*, 71:2134–2137, Sep 1993.
- [63] C. C. Tsuei, J. R. Kirtley, C. C. Chi, Lock See Yu-Jahnes, A. Gupta, T. Shaw, J. Z. Sun, and M. B. Ketchen. Pairing symmetry and flux quantization in a tricrystal superconducting ring of $\text{YBa}_2\text{Cu}_3\text{O}_{7-\gamma}$. *Phys. Rev. Lett.*, 73:593–596, Jul 1994.
- [64] Z.-X. Shen, D. S. Dessau, B. O. Wells, D. M. King, W. E. Spicer, A. J. Arko, D. Marshall, L. W. Lombardo, A. Kapitulnik, P. Dickinson, S. Doniach, J. DiCarlo, T. Loeser, and C. H. Park. Anomalously large gap anisotropy in the *a* - *b* plane of $\text{Bi}_2\text{Sr}_2\text{CaCu}_2\text{O}_{8+\delta}$. *Phys. Rev. Lett.*, 70:1553–1556, Mar 1993.
- [65] Gustafsson, GolubevD., FogelstromM., ClaesonT., KubatkinS., BauchT., and LombardiF. Fully gapped superconductivity in a nanometre-size $\text{yba}_2\text{cu}_3\text{o}_7$ -[delta] island enhanced by a magnetic field. *Nat Nano*, 8(1):25–30, Jan 2013.
- [66] B. D. Josephson. The discovery of tunnelling supercurrents. *Rev. Mod. Phys.*, 46:251–254, Apr 1974.
- [67] P. W. Anderson and J. M. Rowell. Probable observation of the josephson superconducting tunneling effect. *Phys. Rev. Lett.*, 10:230–232, Mar 1963.
- [68] Vinay Ambegaokar and Alexis Baratoff. Tunneling between superconductors. *Phys. Rev. Lett.*, 10:486–489, Jun 1963.
- [69] A. A. Golubov, M. Yu. Kupriyanov, and E. Il'ichev. The current-phase relation in josephson junctions. *Rev. Mod. Phys.*, 76:411–469, Apr 2004.
- [70] Robert Rifkin and Bascom S. Deaver. Current-phase relation and phase-dependent conductance of superconducting point contacts from rf impedance measurements. *Phys. Rev. B*, 13:3894–3901, May 1976.
- [71] K. K. Likharev. Superconducting weak links. *Rev. Mod. Phys.*, 51:101–159, Jan 1979.
- [72] KK Likharev and LA Yakobson. Dynamical properties of superconducting filaments of finite length. *Soviet Journal of Experimental and Theoretical Physics*, 41:570, 1975.

- [73] S. S. Pei, J. E. Lukens, and R. D. Sandell. Measurement of the size dependence of the current-phase relation in microbridge josephson junctions. *Applied Physics Letters*, 36(1): 88–90, 1980.
- [74] William A. Little. Decay of persistent currents in small superconductors. *Phys. Rev.*, 156: 396–403, Apr 1967.
- [75] L. N. Bulaevskii, M. J. Graf, C. D. Batista, and V. G. Kogan. Vortex-induced dissipation in narrow current-biased thin-film superconducting strips. *Phys. Rev. B*, 83:144526, Apr 2011.
- [76] D. Yu. Vodolazov, I. L. Maksimov, and E. H. Brandt. Modulation instability of the order parameter in thin-film superconductors with edge barrier. *EPL (Europhysics Letters)*, 48 (3):313.
- [77] A. Gurevich and V. M. Vinokur. Comment on "vortex-assisted photon counts and their magnetic field dependence in single-photon superconducting detectors". *Phys. Rev. B*, 86: 026501, Jul 2012.
- [78] D. Y. Vodolazov. Saddle point states in two-dimensional superconducting films biased near the depairing current. *Phys. Rev. B*, 85:174507, May 2012.
- [79] H. Risken and T. Frank. *The Fokker-Planck Equation: Methods of Solution and Applications*. Springer Series in Synergetics. ISBN 9783540615309.
- [80] L. N. Bulaevskii, Matthias J. Graf, and V. G. Kogan. Vortex-assisted photon counts and their magnetic field dependence in single-photon superconducting detectors. *Phys. Rev. B*, 85:014505, Jan 2012.
- [81] Antonio Barone and Gianfranco Paterno. *Physics and applications of the Josephson effect*. 1982.
- [82] Tsutomu Yamashita and Yutaka Onodera. Magnetic-field dependence of josephson current influenced by self-field. *Journal of Applied Physics*, 38(9):3523–3525, 1967.
- [83] C. S. Owen and D. J. Scalapino. Vortex structure and critical currents in josephson junctions. *Phys. Rev.*, 164:538–544, Dec 1967.
- [84] V. G. Kogan, V. V. Dobrovitski, J. R. Clem, Yasunori Mawatari, and R. G. Mints. Josephson junction in a thin film. *Phys. Rev. B*, 63:144501, Mar 2001.
- [85] IK Yanson. Effect of fluctuations on the dependence of the josephson current on the magnetic field. *Soviet Journal of Experimental and Theoretical Physics*, 31:800, 1970.
- [86] R. C. Dynes and T. A. Fulton. Supercurrent density distribution in josephson junctions. *Phys. Rev. B*, 3:3015–3023, May 1971.
- [87] Tsutomu Yamashita, Masanori Kunita, and Yutaka Onodera. Magnetic-field dependence of josephson current modified by self-field. *Journal of Applied Physics*, 39(12), 1968.
- [88] S. Basavaiah and R. Broom. Characteristics of in-line josephson tunneling gates. *IEEE Transactions on Magnetics*, 11(2):759–762, 1975.

- [89] Peter A. Rosenthal, M. R. Beasley, K. Char, M. S. Colclough, and G. Zaharchuk. Flux focusing effects in planar thin-film grain-boundary josephson junctions. *Applied Physics Letters*, 59(26), 1991.
- [90] John R. Clem. Josephson junctions in thin and narrow rectangular superconducting strips. *Phys. Rev. B*, 81:144515, Apr 2010.
- [91] Maayan Moshe, V. G. Kogan, and R. G. Mints. Edge-type josephson junctions in narrow thin-film strips. *Phys. Rev. B*, 78:020510, Jul 2008.
- [92] R. G. Mints. Nonlocal josephson electrodynamics. *Journal of Low Temperature Physics*, 106(3):183–192, 1997.
- [93] A. A. Boris, A. Rydh, T. Golod, H. Motzkau, A. M. Klushin, and V. M. Krasnov. Evidence for nonlocal electrodynamics in planar josephson junctions. *Phys. Rev. Lett.*, 111:117002, Sep 2013.
- [94] D. E. McCumber. Effect of ac impedance on dc voltage-current characteristics of superconductor weak-link junctions. *Journal of Applied Physics*, 39(7), 1968.
- [95] W. C. Stewart. Current-voltage characteristics of josephson junctions. *Applied Physics Letters*, 12(8), 1968.
- [96] Sidney Shapiro. Josephson currents in superconducting tunneling: The effect of microwaves and other observations. *Phys. Rev. Lett.*, 11:80–82, Jul 1963.
- [97] Sidney Shapiro, Andre R. Janus, and Sandor Holy. Effect of microwaves on josephson currents in superconducting tunneling. *Rev. Mod. Phys.*, 36:223–225, Jan 1964.
- [98] P. Russer. Influence of microwave radiation on current-voltage characteristic of superconducting weak links. *Journal of Applied Physics*, 43(4), 1972.
- [99] John Clarke and Alex I Braginski. *The SQUID handbook: Applications of SQUIDs and SQUID systems*. John Wiley & Sons, 2006.
- [100] P. W. Anderson and A. H. Dayem. Radio-frequency effects in superconducting thin film bridges. *Phys. Rev. Lett.*, 13:195–197, Aug 1964.
- [101] Riccardo Arpaia, Marco Arzeo, Shahid Nawaz, Sophie Charpentier, Floriana Lombardi, and Thilo Bauch. Ultra low noise $\text{YBa}_2\text{Cu}_3\text{O}_{7-\gamma}$ nano superconducting quantum interference devices implementing nanowires. *Applied Physics Letters*.
- [102] Claudia D. Tesche and John Clarke. dc squid: Noise and optimization. *Journal of Low Temperature Physics*, 29(3):301–331, 1977.
- [103] Won-Tien Tsang and T. Van Duzer. dc analysis of parallel arrays of two and three josephson junctions. *Journal of Applied Physics*, 46(10), 1975.
- [104] K. Hasselbach, D. Mailly, and J. R. Kirtley. Micro-superconducting quantum interference device characteristics. *Journal of Applied Physics*, 91(7), 2002.
- [105] R. Arpaia, M. Arzeo, S. Nawaz, S. Charpentier, F. Lombardi, and T. Bauch. Ultra low noise $\text{YBa}_2\text{Cu}_3\text{O}_{7-\gamma}$ nano superconducting quantum interference devices implementing nanowires. *Applied Physics Letters*, 104(7):072603, 2014.

- [106] Asier Ozaeta. Transport phenomena in superconducting hybrid nanostructures. *arXiv preprint arXiv:1409.7805*, 2014.
- [107] P. G. de Gennes. Boundary effects in superconductors. *Rev. Mod. Phys.*, 36:225–237, Jan 1964.
- [108] L.D. Landau, E.M. Lifshitz, and J.B. Sykes. *Course of Theoretical Physics: Non-relativistic Theory. Quantum Mechanics.* Course of theoretical physics. ISBN 9780080291406.
- [109] M. Y. Kupriyanov and K. K. Likharev. Towards the quantitative theory of the high- T_c josephson junctions. *IEEE Transactions on Magnetics*, 27(2):2460–2463, 1991.
- [110] B. A. Aminov, A. A. Golubov, and M. Yu. Kupriyanov. Quasiparticle current in ballistic constrictions with finite transparencies of interfaces. *Phys. Rev. B*, 53:365–373, Jan 1996.
- [111] AF Andreev. Thermal conductivity of the intermediate state of superconductors. *Zh. Eksperim. i Teor. Fiz.*, 46, 1964.
- [112] C. W. J. Beenakker. *Colloquium* : Andreev reflection and klein tunneling in graphene. *Reviews of Modern Physics*, 80(4):1337–1354, October 2008.
- [113] G. E. Blonder, M. Tinkham, and T. M. Klapwijk. Transition from metallic to tunneling regimes in superconducting microconstrictions: Excess current, charge imbalance, and supercurrent conversion. *Phys. Rev. B*, 25:4515–4532, Apr 1982.
- [114] K. Flensberg, J. Bindslev Hansen, and M. Octavio. Subharmonic energy-gap structure in superconducting weak links. *Phys. Rev. B*, 38:8707–8711, Nov 1988.
- [115] B. Pannetier and H. Courtois. Andreev reflection and proximity effect. *Journal of Low Temperature Physics*, 118(5):599–615, 2000.
- [116] C. W. J. Beenakker and H. van Houten. Josephson current through a superconducting quantum point contact shorter than the coherence length. *Phys. Rev. Lett.*, 66:3056–3059, Jun 1991.
- [117] Philip F. Bagwell. Suppression of the josephson current through a narrow, mesoscopic, semiconductor channel by a single impurity. *Phys. Rev. B*, 46:12573–12586, Nov 1992.
- [118] C Caroli, R Combescot, D Lederer, P Nozieres, and D Saint-James. A direct calculation of the tunnelling current. ii. free electron description. *Journal of Physics C: Solid State Physics*, 4(16):2598.
- [119] C. W. J. Beenakker. Universality in the random-matrix theory of quantum transport. *Phys. Rev. Lett.*, 70:1155–1158, Feb 1993.
- [120] IO Kulik. Macroscopic quantization and the proximity effect in sns junctions. *Soviet Journal of Experimental and Theoretical Physics*, 30:944, 1969.
- [121] IO Kulik and A Omelyanchuk. Pis’ ma zh. éksp. teor. fiz. 21 (4), 216 (1975)[jetp lett. 21 (4), 96 (1975)]. *Zh. Eksp. Teor. Fiz*, 68(6):2139, 1975.
- [122] Klaus D. Usadel. Generalized diffusion equation for superconducting alloys. *Phys. Rev. Lett.*, 25:507–509, Aug 1970.

- [123] P. Dubos, H. Courtois, B. Pannetier, F. K. Wilhelm, A. D. Zaikin, and G. Schön. Josephson critical current in a long mesoscopic S - N - S junction. *Phys. Rev. B*, 63:064502, Jan 2001.
- [124] H. Courtois, Ph. Gandit, and B. Pannetier. Proximity-induced superconductivity in a narrow metallic wire. *Phys. Rev. B*, 52:1162–1166, Jul 1995.
- [125] Jiro Yoshida, Tatsunori Hashimoto, Shinji Inoue, Yoshihisa Mizutani, Masayuki Sagoi, and Koichi Mizushima. Josephson effect in $\text{YBa}_2\text{Cu}_3\text{O}_{7-\gamma}$ / Au-Ag/Pb junctions. *Japanese Journal of Applied Physics*, 31(6R):1771.
- [126] Frank K. Wilhelm, Andrei D. Zaikin, and Gerd Schön. Superconducting current in narrow proximity wires. *Czechoslovak Journal of Physics*, 46(4):2395–2396, 1996.
- [127] AD Zaikin and GF Zharkov. Effect of external fields and impurities on the Josephson current in SNS junctions. *Sov. Phys.-JETP (Engl. Transl.);(United States)*, 54(5), 1981.
- [128] I. O. Kulik and A. G. Omelyanchuk. Properties of Superconducting Microbridges in the Pure Limit. *Sov. J. Low Temp. Phys.*, 3:459–461, 1978.
- [129] Gert Eilenberger. Transformation of Gorkov’s equation for type II superconductors into transport-like equations. *Zeitschrift für Physik A Hadrons and nuclei*, 214(2):195–213, 1968.
- [130] LP Gor’kov. Energy spectrum of superconductors.[quantum field theory]. *Sov. Phys.-JETP (Engl. Transl.);(United States)*, 7(3), 1958.
- [131] Artem V. Galaktionov and Andrei D. Zaikin. Quantum interference and supercurrent in multiple-barrier proximity structures. *Phys. Rev. B*, 65:184507, Apr 2002.
- [132] G Linker, XX Xi, O Meyer, Q Li, and J Geerk. Control of growth direction of epitaxial $\text{YBa}_2\text{Cu}_3\text{O}_{7-\gamma}$ thin films on SrTiO_3 substrates. *Solid state communications*, 69(3):249–253, 1989.
- [133] CB Eom, AF Marshall, SS Laderman, and RD Jacowitz. Epitaxial and smooth films of a -axis $\text{YBa}_2\text{Cu}_3\text{O}_{7-\gamma}$. 1990.
- [134] R. Ramesh, C. C. Chang, T. S. Ravi, D. M. Hwang, A. Inam, X. X. Xi, Q. Li, X. D. Wu, and T. Venkatesan. Structural perfection of Y-Ba-Cu-O thin films controlled by the growth mechanism. *Applied Physics Letters*, 57(10), 1990.
- [135] S. Hontsu, N. Mukai, J. Ishii, T. Kawai, and S. Kawai. a -axis oriented growth of $\text{YBa}_2\text{Cu}_3\text{O}_{7-\gamma}$ films on $\text{LaSrGaO}_4(100)$ substrates. *Applied Physics Letters*, 61(9), 1992.
- [136] Y. Suzuki, D. Lew, A. F. Marshall, M. R. Beasley, and T. H. Geballe. Anisotropic transport properties of in-plane-aligned a -axis $\text{YBa}_2\text{Cu}_3\text{O}_{7-\gamma}$ films. *Phys. Rev. B*, 48:10642–10645, Oct 1993.
- [137] a axis laser ablated superconducting YBCO thin films growth mechanism on MgO substrate. *Journal of Alloys and Compounds*, 195:235 – 238, 1993.
- [138] Jerzy Krupka, Richard G Geyer, Matthias Kuhn, and Johann Heyen Hinken. Dielectric properties of single crystals of Al_2O_3 , LaAlO_3 , NdGaO_3 , SrTiO_3 , and MgO at cryogenic temperatures. *IEEE Transactions on Microwave Theory and Techniques*, 42(10):1886–1890, 1994.

- [139] Dorthe Lybye, Finn Willy Poulsen, and Mogens Mogensen. Conductivity of a- and b-site doped LaAlO_3 , LaGaO_3 , LaSrCo_3 and LaInO_3 perovskites. *Solid State Ionics*, 128(1):91–103, 2000.
- [140] AW McConnell, RA Hughes, A Dabkowski, HA Dabkowska, JS Preston, JE Greedan, and T Timusk. Evaluation of LaSrGaO_4 as a substrate for $\text{YBa}_2\text{Cu}_3\text{O}_{7-\gamma}$. *Physica C: Superconductivity*, 225(1):7–12, 1994.
- [141] C. B. Eom, A. F. Marshall, S. S. Laderman, R. D. Jacowitz, and T. H. Geballe. Epitaxial and smooth films of a-axis $\text{YBa}_2\text{Cu}_3\text{O}_{7-\gamma}$. 249(4976):1549–1552, 1990.
- [142] Z. Trajanovic, C. J. Lobb, M. Rajeswari, I. Takeuchi, C. Kwon, and T. Venkatesan. Critical currents and pinning mechanisms in untwinned a-axis $\text{YBa}_2\text{Cu}_3\text{O}_{7-\gamma}$ thin films. *Phys. Rev. B*, 56:925–933, Jul 1997.
- [143] Jinhua Ye and Keikichi Nakamura. Quantitative structure analyses of $\text{YBa}_2\text{Cu}_3\text{O}_{7-\delta}$ thin films: Determination of oxygen content from x-ray-diffraction patterns. *Phys. Rev. B*, 48:7554–7564, Sep 1993.
- [144] S. Nawaz, R. Arpaia, F. Lombardi, and T. Bauch. Microwave response of superconducting $\text{YBa}_2\text{Cu}_3\text{O}_{7-\gamma}$ nanowire bridges sustaining the critical depairing current: Evidence of Josephson-like behavior. *Phys. Rev. Lett.*, 110:167004, Apr 2013.
- [145] S. Nawaz, R. Arpaia, T. Bauch, and F. Lombardi. Approaching the theoretical depairing current in $\text{YBa}_2\text{Cu}_3\text{O}_{7-\gamma}$ nanowires. *Physica C: Superconductivity*, 495:33 – 38, 2013.
- [146] R. Arpaia, S. Nawaz, F. Lombardi, and T. Bauch. Improved nanopatterning for YBCO nanowires approaching the depairing current. *IEEE Transactions on Applied Superconductivity*, 23(3):1101505–1101505, 2013.
- [147] S. Nawaz, R. Arpaia, F. Lombardi, and T. Bauch. Microwave response of superconducting $\text{YBa}_2\text{Cu}_3\text{O}_{7-\gamma}$ nanowire bridges sustaining the critical depairing current: Evidence of Josephson-like behavior. *Phys. Rev. Lett.*, 110:167004, Apr 2013.
- [148] John R. Clem and Karl K. Berggren. Geometry-dependent critical currents in superconducting nanocircuits. *Phys. Rev. B*, 84:174510, Nov 2011.
- [149] Fred B Hagedorn and PM Hall. Right-angle bends in thin strip conductors. *Journal of Applied Physics*, 34(1):128–133, 1963.
- [150] Simon Abay, Henrik Nilsson, Fan Wu, H.Q. Xu, C.M. Wilson, and Per Delsing. High critical-current superconductor-in-as nanowire-superconductor junctions. *Nano Letters*, 12(11):5622–5625, 2012.
- [151] H. Bartolf, A. Engel, A. Schilling, K. Il'in, M. Siegel, H.-W. Hübers, and A. Semenov. Current-assisted thermally activated flux liberation in ultrathin nanopatterned nbn superconducting meander structures. *Phys. Rev. B*, 81:024502, Jan 2010.
- [152] L. N. Bulaevskii, M. J. Graf, C. D. Batista, and V. G. Kogan. Vortex-induced dissipation in narrow current-biased thin-film superconducting strips. *Phys. Rev. B*, 83:144526, Apr 2011.
- [153] Dynamics of vortex matter in YBCO sub-micron bridges. *Physica C: Superconductivity and its Applications*, 506:188 – 194, 2014.

- [154] Reza Baghdadi, Riccardo Arpaia, Sophie Charpentier, Dmitri Golubev, Thilo Bauch, and Floriana Lombardi. Fabricating nanogaps in $\text{YBa}_2\text{Cu}_3\text{O}_{7-\gamma}$ for hybrid proximity-based josephson junctions. *Phys. Rev. Applied*, 4:014022, Jul 2015.
- [155] John R. Clem and V. G. Kogan. Kinetic impedance and depairing in thin and narrow superconducting films. *Phys. Rev. B*, 86:174521, Nov 2012.
- [156] John Bardeen. Critical fields and currents in superconductors. *Rev. Mod. Phys.*, 34:667–681, Oct 1962.
- [157] Z. G. Ivanov, N. Ya. Fogel, O. I. Yuzepovich, E. A. Stepantsov, and A. Ya. Tzalenchuk. Depairing critical currents and self-magnetic field effects in submicron $\text{YBa}_2\text{Cu}_3\text{O}_{7-\gamma}$ microbridges and bicrystal junctions. *Low Temperature Physics*, 30(3):203–207, 2004.
- [158] $\text{YBa}_2\text{Cu}_3\text{O}_{7-\gamma}$ nanorings to probe fluxoid quantization in high critical temperature superconductors. *Physica C: Superconductivity and its Applications*, 506:184 – 187, 2014.
- [159] J. Johansson, K. Cedergren, T. Bauch, and F. Lombardi. Properties of inductance and magnetic penetration depth in (103)-oriented $\text{yba}_2\text{cu}_3\text{o}_{7-\delta}$ thin films. *Phys. Rev. B*, 79:214513, Jun 2009.
- [160] R. Arpaia, M. Arzeo, S. Nawaz, S. Charpentier, F. Lombardi, and T. Bauch. Ultra low noise $\text{YBa}_2\text{Cu}_3\text{O}_{7-\gamma}$ nano superconducting quantum interference devices implementing nanowires. *Applied Physics Letters*, 104(7):072603, 2014.
- [161] R. Baghdadi, R. Arpaia, T. Bauch, and F. Lombardi. Toward ybco nanoscale structures for hybrid devices. *IEEE Transactions on Applied Superconductivity*, 25(3):1–4, 2015.
- [162] A. Sawa, S. Kosaka, H. Obara, and K. Aoki. Low-pressure oxidation of $\text{YBa}_2\text{Cu}_3\text{O}_{7-\gamma}$ thin films in purified ozone. *IEEE Transactions on Applied Superconductivity*, 3(1):1088–1091, 1993.
- [163] F Herbstritt, T Kemen, A Marx, and R Gross. Ultraviolet light assisted oxygenation process for submicron $\text{YBa}_2\text{Cu}_3\text{O}_{7-\gamma}$ thin film devices. *J. Appl. Phys.*, 91(8):5411–5418, 2002.
- [164] SJ Rothman, JL Routbort, U Welp, and JE Baker. Anisotropy of oxygen tracer diffusion in single-crystal $\text{YBa}_2\text{Cu}_3\text{O}_{7-\gamma}$. *Phys. Rev. B*, 44(5):2326, 1991.
- [165] H Dreuth and H Dederichs. Evaluation of low resistance contacts on $\text{YBa}_2\text{Cu}_3\text{O}_{7-\gamma}$ thin films using the transmission line model. *Supercond. Sci. Technol.*, 6(7):464.
- [166] R. P. Robertazzi, A. W. Kleinsasser, R. B. Laibowitz, R. H. Koch, and K. G. Stawiasz. *In situ* Ag/ $\text{YBa}_2\text{Cu}_3\text{O}_7$ contacts for superconductor normal-metal superconductor devices. *Phys. Rev. B*, 46:8456–8471, Oct 1992.
- [167] C.-H. Chen, I. Jin, S. P. Pai, Z. W. Dong, C. J. Lobb, T. Venkatesan, K. Edinger, J. Orloff, and J. Melngailis. Fabrication of high-temperature superconducting josephson junctions on substrates patterned by focused ion beam. *Appl. Phys. Lett.*, 73(12):1730–1732, 1998.
- [168] W. L. McMillan and Jack Mochel. Electron tunneling experiments on amorphous $\text{Ge}_{1-x}\text{Au}_x$. *Phys. Rev. Lett.*, 46:556–557, Feb 1981.

- [169] A. Barone, W. J. Johnson, and R. Vaglio. Current flow in large Josephson junctions. *Journal of Applied Physics*, 46(8), 1975.
- [170] J. M. Rowell. Magnetic field dependence of the Josephson tunnel current. *Phys. Rev. Lett.*, 11:200–202, Sep 1963.
- [171] B. Mayer, S. Schuster, A. Beck, L. Alff, and R. Gross. Magnetic field dependence of the critical current in $\text{YBa}_2\text{Cu}_3\text{O}_{7-\gamma}$ bicrystal grain boundary junctions. *Applied Physics Letters*, 62(7), 1993.
- [172] P. Dubos, H. Courtois, O. Buisson, and B. Pannetier. Coherent low-energy charge transport in a diffusive s-n-s junction. *Phys. Rev. Lett.*, 87:206801, Oct 2001.
- [173] Amos Sharoni, Itay Asulin, Gad Koren, and Oded Millo. Proximity effect in gold-coated $\text{YBa}_2\text{Cu}_3\text{O}_{7-\gamma}$ films studied by scanning tunneling spectroscopy. *Phys. Rev. Lett.*, 92:017003, Jan 2004.
- [174] T. R. Dinger, T. K. Worthington, W. J. Gallagher, and R. L. Sandstrom. Direct observation of electronic anisotropy in single-crystal $\text{YBa}_2\text{Cu}_3\text{O}_{7-\gamma}$. *Phys. Rev. Lett.*, 58:2687–2690, Jun 1987.
- [175] I. Takeuchi, Y. Gim, F. C. Wellstood, C. J. Lobb, Z. Trajanovic, and T. Venkatesan. Systematic study of anisotropic Josephson coupling between $\text{YBa}_2\text{Cu}_3\text{O}_{7-x}$ and PbIn using in-plane aligned a -axis films. *Phys. Rev. B*, 59:7205–7208, Mar 1999.
- [176] Zhang Hong, Wu Hong, Ren Cong-Xin, and Chen Guo-Liang. The anisotropy of the current-carrying characteristics of YBCO film fabricated by magnetron sputtering. *Superconductor Science and Technology*, 7(6):359.
- [177] High temperature superconductor twin films: Growth mechanics - interfaces - multilayers anisotropy of the critical current in YBCO thin films grown by metal organic chemical vapour deposition. *Journal of Alloys and Compounds*, 251(1):351 – 354, 1997.
- [178] T. K. Worthington, W. J. Gallagher, and T. R. Dinger. Anisotropic nature of high-temperature superconductivity in single-crystal $\text{YBa}_2\text{Cu}_3\text{O}_{7-\gamma}$. *Phys. Rev. Lett.*, 59:1160–1163, Sep 1987.
- [179] J. Johansson, K. Cedergren, T. Bauch, and F. Lombardi. Properties of inductance and magnetic penetration depth in (103)-oriented $\text{YBa}_2\text{Cu}_3\text{O}_{7-\gamma}$ thin films. *Phys. Rev. B*, 79:214513, Jun 2009.
- [180] M M Khapaev Jr. Extraction of inductances of plane thin film superconducting circuits. *Superconductor Science and Technology*, 10(6):389.
- [181] G. Blatter, M. V. Feigel'man, V. B. Geshkenbein, A. I. Larkin, and V. M. Vinokur. Vortices in high-temperature superconductors. *Rev. Mod. Phys.*, 66:1125–1388, Oct 1994.
- [182] Erez Berg, Eduardo Fradkin, and Steven A. Kivelson. Charge-4e superconductivity from pair-density-wave order in certain high-temperature superconductors. *Nat Phys*, 5(11):830–833, Nov 2009.
- [183] Eduardo Fradkin, Steven A Kivelson, and John M Tranquada. Colloquium: Theory of intertwined orders in high temperature superconductors. *Rev. Mod. Phys.*, 87(2):457, 2015.

- [184] T. Imaizumi, T. Kawai, T. Uchiyama, and I. Iguchi. Tunneling between dissimilar high- T_c oxide superconductors. *Phys. Rev. Lett.*, 89:017005, Jun 2002.
- [185] The origin of the half-integral constant voltage steps in high- T_c grain-boundary junction. *Physica C: Superconductivity*, 243(1):187 – 190, 1995.
- [186] Myung-Ho Bae, R. C. Dinsmore III, M. Sahu, Hu-Jong Lee, and A. Bezryadin. Zero-crossing shapiro steps in high- T_c superconducting microstructures tailored by a focused ion beam. *Phys. Rev. B*, 77:144501, Apr 2008.
- [187] Charles Kittel. *Introduction to solid state*. John Wiley & Sons, 1966.
- [188] Hans Eisenmann, Thomas Waas, and Hans Hartmann. Proximity correction of high-dosed frame with proxecco, 1994.